

**ROLE OF ANTENNAS AND THE PROPAGATION CHANNEL ON THE
PERFORMANCE OF AN ULTRA WIDE BAND (UWB)
COMMUNICATION SYSTEM**

**A
THESIS**

**Presented to the Faculty
of the University of Alaska Fairbanks
in Partial Fulfillment of the Requirements
for the Degree of**

DOCTOR OF PHILOSOPHY

By

Arun Venkatasubramanian, B.S., M.S.

Fairbanks, Alaska

December 2007

UMI Number: 3302513

INFORMATION TO USERS

The quality of this reproduction is dependent upon the quality of the copy submitted. Broken or indistinct print, colored or poor quality illustrations and photographs, print bleed-through, substandard margins, and improper alignment can adversely affect reproduction.

In the unlikely event that the author did not send a complete manuscript and there are missing pages, these will be noted. Also, if unauthorized copyright material had to be removed, a note will indicate the deletion.

UMI[®]

UMI Microform 3302513

Copyright 2008 by ProQuest LLC.

All rights reserved. This microform edition is protected against unauthorized copying under Title 17, United States Code.

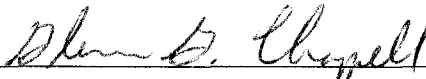
ProQuest LLC
789 E. Eisenhower Parkway
PO Box 1346
Ann Arbor, MI 48106-1346

ROLE OF ANTENNAS AND THE PROPAGATION CHANNEL ON
THE PERFORMANCE OF AN ULTRA WIDEBAND (UWB)
COMMUNICATION SYSTEM

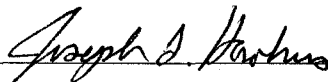
By

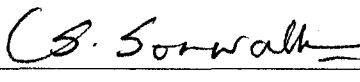
Arun Venkatasubramanian

RECOMMENDED:

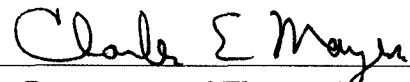






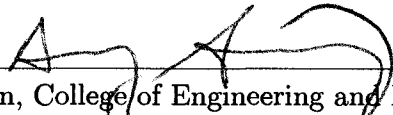


Chair, Advisory Committee

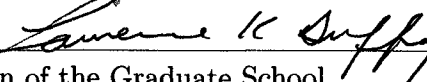


Chair, Department of Electrical and Computer Engineering

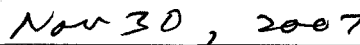
APPROVED:



Dean, College of Engineering and Mines



Dean of the Graduate School



Date

Abstract

The objectives of this dissertation are to experimentally and numerically quantify the effect of antennas and the propagation channel on the performance of an Ultra Wide Band (UWB) receiver. This work has led to the following new results: (1) the variation in the time duration of the impulse response of the oval dipole in the vertical plane is within 5% up to an angle $\theta = 60^\circ$ off the broadside direction ($\theta = 90^\circ$); at larger angles a factor of six elongation in the time duration of the impulse response along the antenna axis ($\theta = 0^\circ$) is observed, (2) for an axial ratio of 0.5, the oval dipole has a Voltage Standing Wave Ratio (VSWR) of 2:1 ($\sim 11\%$ reflection coefficient) in a 3.1 GHz bandwidth with a lower cut off frequency of 2.8 GHz; for an axial ratio of 2.0 this scales to 0.5 GHz bandwidth with a lower cut off frequency of 1.75 GHz, (3) a new theoretical model has been developed for UWB pulse propagation over the ground which takes into account the geometrical properties of the propagation channel (such as the heights of the transmitter (h_1) and the receiver (h_2) over the ground) and the nature of the radiated UWB pulse (such as pulse duration (τ_p) and cycle time (τ_c)), (4) an improvement in bit error rate by up to a factor of 100 can be achieved for a matched filter receiver by careful orientation of the transmitting and the receiving oval dipole antennas used in the measurements presented in this dissertation.

Table of Contents

	Page
Signature Page	i
Title Page	ii
Abstract	iii
Table of Contents	iv
List of Figures	viii
List of Tables	xiii
List of Appendices	xiv
Acknowledgements	xv
Chapter 1 Introduction	1
1.1 Objective of this Dissertation	1
1.2 Background	1
1.3 Literature Review	3
1.4 Problem Statement and Approach	5
1.5 Contributions of the Present Work	6
1.6 Organization of the Dissertation	7
Chapter 2 UWB Dipole Antennas: Experiments and Numerical Simulations	9
2.1 Objective and Significance	9
2.2 Experiments	11
2.2.1 Experimental Setup and Instrumentation Description	11

	Page
2.2.2 Frequency Domain Scattering Parameter Measurements	16
2.2.2.1 Broadside Transmitting and Receiving Impulse Response Measurement	16
2.2.2.2 Voltage Standing Wave Ratio (VSWR) Measurement . . .	19
2.2.2.3 Measurement of the Cross-Polarized Antenna Response . .	21
2.2.2.4 Co-Polarized and Cross-Polarized Radiation Pattern of the Oval Dipole Antenna	21
2.2.3 Time domain Measurement of the Received Voltage Waveform . . .	25
2.3 Finite Difference Time Domain Simulations	31
2.3.1 Mathematical Formulation	31
2.3.2 Accuracy and Stability	34
2.3.3 Boundary Conditions	35
2.3.4 Serial Implementation	35
2.3.5 Bottlenecks in Serial Code	38
2.3.6 Parallel Implementation of the Serial Code	39
2.4 Simulation of the Oval Dipole Antenna	40
2.5 Summary of Results	48
2.6 Discussion	48
2.7 Concluding Remarks	50
Chapter 3 UWB Pulse Propagation: Experiments and Numerical Simula-	
tions	51
3.1 Objective and Significance	51
3.2 UWB Pulse Propagation in an Empty Parking lot	53
3.2.1 Measurements	54
3.2.1.1 Experiment Geometry	54
3.2.1.2 Instrumentation Description and Measurements	54
3.2.1.3 PulsON 200 Antenna Description and Measurements . . .	60

	Page
3.2.1.4 Measurement of the Peak Amplitude of the Received UWB Pulse	62
3.2.1.5 Multiple Reflections from a Layered Ground	66
3.2.2 Theoretical Formulation	67
3.2.2.1 A General Time and Frequency Domain Representations of UWB Multipath Propagation	67
3.2.2.2 Theoretical Model of the Propagation Regimes: First and Second Breakpoints	74
3.2.2.3 Extension of the Theoretical Model to Finite Wall case for LOS and NLOS propagation	78
3.2.2.4 Comparison of the Theoretical model with Experiments	82
3.3 UWB Pulse Propagation inside a Building	83
3.3.1 Measurements	83
3.3.2 FDTD Simulations	87
3.4 Summary of Results	88
3.5 Discussion	89
3.5.1 Range of Propagation Regimes Consistent with FCC Regulation	89
3.5.2 Effect of Finite Thickness Walls on UWB Receiver Performance	89
3.5.3 Extension of the Theoretical Model to LOS and NLOS Scenarios With More Than Two Propagation Paths	91
3.6 Concluding Remarks	94
Chapter 4 Numerical Model of a UWB Matched Filter Receiver and a Rake Receiver	96
4.1 Objective and Significance	96
4.2 Simulation Model of a UWB Communication System	99
4.2.1 Waveform Generation Model	99
4.2.2 Transmitter Model	100

	Page
4.2.3 Transmitting Antenna and the Propagation Channel Model	102
4.2.4 Noise and Interference Model	105
4.2.5 Receiving Antenna Model	107
4.2.6 Receiver Model	109
4.2.6.1 Matched Filter Receiver Model	109
4.2.6.2 Rake Receiver Model	115
4.3 Simulation Results - Case Studies	116
4.3.1 Case A - Effect of the Transmitting and the Receiving Antenna on the Bit Error rate of a Matched Filter and a Rake Receiver	117
4.3.2 Case B - Effect of the Transmitting Antenna Orientation on the Bit Error Rate of a Matched Filter and a Rake Receiver	118
4.3.3 Case C - Effect of the UWB Propagation Channel on the Bit Error Rate of a Matched Filter and a Rake Receiver	121
4.4 Summary of Results	123
4.5 Discussion	125
4.6 Concluding Remarks	125
Chapter 5 Conclusions and Recommendations	126
5.1 Introduction	126
5.2 Summary of Conclusions	126
5.3 Deficiencies in the Presented Work and Suggested Improvements	128
5.4 Outstanding Research Questions and Recommendations	130
References	133
Appendices	144

List of Figures

	Page
1.1 Federal Communications Commission (FCC) spectrum allocation for UWB indoor applications	2
1.2 Problem approach	6
2.1 Transmitting and receiving antenna coordinate system	12
2.2 Experimental setup and instrumentation used for antenna measurements in the time and frequency domain	13
2.3 UWB Reference Antennas	15
2.4 Pictures of the UWB microstrip dipole antennas built at UAF	15
2.5 Transmitting antenna transfer function computed for the oval and cat-fish dipole antennas	17
2.6 Receiving antenna transfer function computed for the oval and cat-fish dipole antennas	18
2.7 Transmitting and receiving antenna impulse response using the transfer functions calculated from frequency domain scattering parameter measurements for the oval and cat-fish dipole antennas	19
2.8 VSWR of the oval and the cat-fish dipole antennas	20
2.9 Co-polarized and cross-polarized transmitting and receiving impulse response of a pair of oval dipole antennas separated by 2 m in the anechoic chamber	22

	Page
2.10 Directional dependence of the co-polarized components of the oval dipole antenna transfer function and impulse response	24
2.11 Directional dependence of the cross-polarized components of the oval dipole antenna transfer function and impulse response	26
2.12 Radiation pattern of the oval dipole antenna in the vertical and horizontal planes	27
2.13 Time and frequency domain measurement of the received voltage waveform for a pair of identical horn antennas	29
2.14 Time and frequency domain measurement of the received voltage waveform for a pair of identical horn antennas	30
2.15 Position of the field components on a single Yee cell	32
2.16 Computation flow of the serial FDTD program	36
2.17 Snapshot in time of the electric field strength radiated by a 6 cm long dipole antenna	37
2.18 Three snapshots in time of a electromagnetic wave impinging on the PML boundary	38
2.19 The execution time as a function of the number of processors for a 200 X 200 X 200 problem space with 1000 time steps	40
2.20 Simulation geometry of the oval dipole antenna	41
2.21 Measured and simulated received voltage waveform for a oval dipole transmitter and a horn receiver system	44
2.22 Time evolution of the current distribution on the oval antenna calculated using FDTD	45
2.23 Effect of axial ratio of the oval on its matching and gain properties	46
3.1 Schematic showing the geometry of UWB pulse propagation in the presence of a single reflecting surface	55

	Page
3.2 The PulsON 200 TM impulse captured by the PulsON 200 TM receiver (dotted line trace) and the Tektronix DSO (solid line trace), and their frequency domain spectra (lower panel)	57
3.3 The change in radiated pulse shape as a function of elevation angle	58
3.4 The change in radiated pulse spectrum as a function of elevation angle	58
3.5 Radiation pattern of the PulsON 200 TM Broadspec antenna	59
3.6 The change in time domain properties of received UWB pulse as a function of receiving angle θ_R	59
3.7 The change in frequency domain properties of the received UWB pulse as a function of receiving angle θ_R	60
3.8 The relative path loss as a function of separation distance between the transmitter and the receiver held at 0.5 m above the ground	64
3.9 Path loss measurement as a function of separation distance between the PulsON200 transmitter and receiver	65
3.10 Four different types of received voltage waveforms measured by the PulsON 200 receiver in the Taku parking lot measurement	68
3.11 Schematic showing the overlap of the direct and reflected pulses in the time domain	75
3.12 Schematic showing the geometry of UWB pulse propagation in the presence of a single finite thickness reflecting surface for LOS and NLOS cases	79
3.13 Comparison between the the maxima and minima distance predicted by the hyperbola model and measured from the signal strength data	82
3.14 Measurement and simulation of UWB pulse propagation inside a hallway in the Duckering building at UAF	85
3.15 Time snapshots of the FDTD calculation of the UWB peak electric field amplitude along the length of the hallway, across the corner, and inside the laboratory room	86

	Page
3.16 Calculation of the three propagation regimes for varying pulse and geometrical parameters	90
3.17 Ray tracing simulation of UWB pulse propagation in the presence of a 30 cm concrete wall	92
4.1 Block diagram of the numerical model of an UWB communication link from signal generation to information retrieval	98
4.2 Block diagram of the UWB waveform generation model	100
4.3 Normalized waveforms and spectra for the measured MSSSI pulse (solid line) and the simulated first and second derivatives of the gaussian pulse (dotted lines) with a pulse width of 0.6 ns	101
4.4 Block diagram of the UWB transmitter model	103
4.5 Example of a dithered and un-dithered pulse train generated by the transmitter model	104
4.6 Block diagram for transmitting antenna model	104
4.7 Block diagram for propagation channel model	105
4.8 Block diagram for the receiving antenna model	108
4.9 Example of the radiated electric field waveform from a transmitting horn antenna and the electric field waveform 4.2 m apart in a line of sight hallway	108
4.10 Block diagram of the matched filter receiver model	109
4.11 Block diagram and output of the template generator model	111
4.12 Block diagram and output of the acquisition model	111
4.13 Block diagram for demodulation of the transmitted information from the received signal	113
4.14 Example of pulse sequence with single and two UWB users transmitting with a 5 dB ratio of received bit energy to noise spectral density	114
4.15 Block diagram of a two arm rake receiver model	116

	Page
4.16 Bit error rate performance curves as a function of transmitted bit energy (E_b) to noise density (N_0) ratio for a matched filter and a rake receiver with two identical antenna pairs in the anechoic chamber	119
4.17 The effect of transmitting antenna orientation on the bit error rate as a function of E_b/N_0 for a matched filter and a rake receiver	122
4.18 Effect of template selection on the bit error rate of a rake receiver	123
4.19 The effect of the propagation channel on the bit error rate as a function of E_b/N_0 for a matched filter and a RAKE receiver with 20, and 200 branches	124
A.1 VNA noise floor with both analyzer cables terminated with 50 Ω loads and calibrated shorts	145
A.2 DSO Noise waveform and statistics for vertical sensitivity equal to 10 mV/div	147
A.3 Free space measurements to calibrate anechoic chamber using Time Domain PulsON200 TM antenna	151
A.4 Transmitting antenna transfer function computed for the horn antenna	154
A.5 Receiving antenna transfer function for the horn antenna	154
A.6 Transmitting and receiving band-limited impulse response of the horn antenna	156
A.7 Time domain measurement of the band-limited impulse response of a pair of horn antennas	158
B.1 Determination of duration and cycle time of the input pulse	160
B.2 Determination of bandwidth B and center frequency f_c	162
B.3 Flow diagram for the algorithm to determine breakpoint distances and maxima and minima in the received signal strength data	164
B.4 Determination of breakpoint distances and maxima and minima in the received signal strength data for $h_1 = h_2 = 0.5$ m.	165
B.5 Problem geometry to calculate the permittivity of the ground	166
B.6 Examples of received UWB pulses measured in the Taku parking lot at UAF	169
B.7 Measured ϵ_r as a function of distance in the Taku Parking Lot	171

List of Tables

	Page
4.1 Input parameters for the UWB communication system simulations presented in this chapter	117
A.1 Agilent E8356A VNA noise power level and noise floor	146
A.2 Noise Performance of Tektronix TDS6804B DSO	148
A.3 Maximum Signal-to-Noise Ratio for Tektronix TDS6804B DSO	148
B.4 Dates, temperature and ground conditions in the Taku parking lot when the UWB propagation measurements were performed	170

List of Appendices

	Page
Appendix A Noise Calculation in Experiments	144
A.1 Noise Floor of the Agilent E8358A Vector Network Analyzer	144
A.2 Tektronix TDS6804B Digital Signal Oscilloscope	144
A.2.1 Vertical Resolution and Quantization Noise	144
A.2.2 Sensitivity of the DSO	149
A.3 Anechoic Chamber Calibration Measurements	150
A.4 Signal Processing Algorithms	152
A.4.1 Frequency Domain De-convolution of the Antenna Impulse Response	152
A.4.2 Time Domain De-convolution of the Antenna Impulse Response . . .	155
Appendix B Data Processing Algorithms	159
B.1 Calculation of the Pulse Width τ_p and the Pulse Cycle Time τ_c	159
B.2 Calculation of the Bandwidth B and the Center Frequency f_c	161
B.3 Algorithm to Calculate the Breakpoint Distances and the Location of Maxima and Minima in the RSS data	162
B.4 Calculate the relative permittivity of the ground and the thickness of snow layer on the ground using UWB measurements	163
B.4.1 Mathematical Formulation	163
B.4.2 Measurements	167

Acknowledgements

I would like to sincerely thank my mentor and advisor, Dr. Vikas Sonwalkar, for his able guidance and active constructive criticism throughout my tenure at UAF. I would like to sincerely thank Dr. Joseph Hawkins for seeing potential in me and giving me the opportunity to work on an interesting problem like ultra wide band communication. I am always in awe of his work ethics and his ability to communicate efficiently with people. I would also like to thank my committee members Dr. Richard Collins and Dr. Glenn Chappell for taking the time to read my thesis.

I must express my utmost gratitude to Dr. Hans Schantz for funding me in the summer of 2007 and also sharing his views on UWB antennas with me. I will cherish the enlightening discussions I have had with him on antenna design and super luminosity. I would like to thank Dr. Kirk McDonald from Princeton University for providing some insightful suggestions. I must thank Dr. Sergei Maurits and Dr. Brenton Watkins for funding me throughout the summer and the Fall of 2007. Dr. Maurits requires a special mention for his patience while I worked on my thesis and other immigration issues.

I would like to thank Bruce Johnson for four reasons: (1) for teaching me how to etch microstrip antennas, (2) for teaching me Agilent Momentum software, (3) working closely with me on improving the ray tracing code written as part of my masters thesis, and (4) assisting in planning and performing the various antenna and propagation measurements. The experiments presented in this thesis are as much his work as they are mine.

I would like to thank Tom Logan from the Arctic Region Super Computing (ARSC) center for helping me with the Finite difference time domain code development. I would like to thank Shelly Bauman and Laura Bender from the graduate school for answering innumerable questions on typesetting my dissertation and helping me find an external examiner in short notice. I would like to thank Todd Parris and Blake Ryder for taking the

time to read my thesis and helping me sort out the cobwebs in my English language. I would also like to thank Amani Reddy and Ashish Agarwal for helping me with two of my measurements.

I am indebted to my wife, Ganga, who has provided me with the encouragement necessary for me to succeed. It was her sustained support and love that got me through these three rough months. I consider myself the luckiest man in the world for having her beside me as a pillar of strength. I would also like to thank my dad, Dr. N. Venkatasubramanian, who will always be my role model, my ever loving mom, Dr. Chandra Venkatasubramanian, my sister, Aparna, my grand parents, Lt. Col. P. Sreenivasan and Mrs. Gomathi Sreenivasan, and my wonderful aunt, Mrs. Banumathi Suresh, for her trust in my ability and her support towards helping me broaden my horizons as a researcher.

I have been fortunate to have been blessed with wonderful friends who keep me smiling no matter what the circumstance. I want to thank Srivathsan, his wife Jayashree and their beautiful daughter Sri Lakshmi. They have been my extended family here in Alaska and I have shared many occasions that has left me with a lifetime of memories. I need to thank Todd, Thangamani, Sara, Adhiyan, Subramanian, Topsy, Baala and Ashok for bearing with my nervous tantrums and standing by me through some tough times.

This research at UAF was supported through a subcontract from Kachemak Research Development Inc., Homer, AK in support of prime contract **N00164-05-D-6653** from the U.S. Navy Crane Division Naval Surface Warfare Center. I would like to thank graduate school for funding me for one year under the thesis completion fellowship. I would like to thank ARSC for funding me through the months of May to December 2007.

Chapter 1 Introduction

1.1 Objective of this Dissertation

The objectives of this dissertation are: (1) To experimentally and numerically relate the geometry of two planar Ultra Wide Band (UWB) microstrip antennas to the nature of the radiated and the received UWB pulse. (2) To relate the nature of the UWB pulse and the physical properties (e.g., geometry, number of reflecting surfaces) of the propagation channel (e.g., hallway) to the peak amplitude of the received pulse at the receiver; (3) To calculate the bit error rate of a UWB receiver in the presence of noise and multipath propagation for two specific transmitting and receiving UWB antenna pairs.

1.2 Background

A UWB signal is a radio signal with an instantaneous bandwidth ≥ 500 MHz [Fowler *et al.*, 1990; Miller, 2003] or a fractional bandwidth ≥ 0.2 , where the fractional bandwidth is defined as the ratio of the instantaneous bandwidth to the center frequency of the signal spectrum [FCC, 2002]. The upper and lower ends of the instantaneous bandwidth are defined by the frequency points where the radiated power is down 10 dB from its peak level. Throughout this dissertation, the bandwidth of a signal is defined as the width of the frequency spectrum between the two -10 dB frequency points.

In the USA, the radiated UWB signal for indoor applications has to conform with the

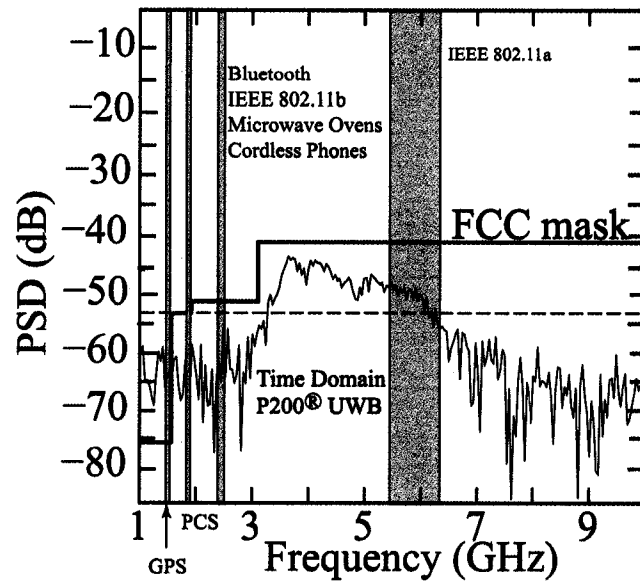


Figure 1.1. **Federal Communications Commission (FCC) spectrum allocation for UWB indoor applications.** The black curve shows the Time Domain PulsON200 UWB signal spectrum and the grayed rectangles show the other commercial applications like GPS, PCS, cell phone, and wireless local area network (WLAN) signals. The solid black line shows the FCC regulated average power of -41.3 dBm/MHz over the licensed frequency band from 3.1 GHz to 10.6 GHz for indoor UWB applications.

following regulations: (1) The occupied spectrum of the UWB signal is between 3.1 GHz to 10.6 GHz. (2) The average radiated power over the entire spectrum should be ≤ -41.3 dBm/MHz or 75 nW/MHz. These bounds ensure that the radiated UWB signals do not cause harmful interference to other licensed services and important radio operations [FCC, 2002]. Figure 1.1 shows the spectrum of a commercial UWB system and other commercial systems that occupy the same frequency band.

The large bandwidth of the UWB signal (500 MHz to 7.5 GHz bandwidth) translates to a short time duration (~ 2 ns to 133.3 ps), which offers several advantages over conventional narrow bandwidth (< 20 MHz) systems: (1) Immunity to interference from multiple propagation paths and other narrow bandwidth signals [Taylor, 2000]; (2) Faster transmission of information at data rates (≥ 100 Mbps over 5 m) [Scholtz, 1993] which are a factor of 100 greater than competing narrow bandwidth technologies like bluetooth (1 Mbps over 10 m) and IEEE 802.15.3+ wireless local area network (55 Mbps over 10 m distance) [Porcino and Hirt, 2003]; (3) Precise location determination (5 cm to 50 cm accuracy) [Siwiak and Mckeown, 2004]; and (4) High resolution radar capabilities [Astani and Kostylev, 1989]. Hence UWB technology has gained considerable research interest for short-range (5 m to 50 m), high data rate (10 Mbps to 480 Mbps) communication, navigation and radar applications [Ghavammi *et al.*, 2007].

1.3 Literature Review

There has been extensive work on several unique aspects and potential applications of UWB technology over the last 20 years. An exhaustive survey of 492 papers was done on the past work in (1) transmitted UWB pulse shape and antenna models, (2) UWB channel measurement and models, (3) UWB receiver design and signal processing algorithms. This was presented as a separate report [Hawkins *et al.*, 2005]. The brief review (8 papers) presented here will focus mainly on the past work done which was not covered as a part of the previous report and that directly relates to the objectives of this dissertation.

To faithfully transmit information from the transmitter to the receiver, it is important

to consider the impairments introduced by the propagation channel and the transmitting and receiving antenna. The propagation channel impairments are a result of frequency dependent reflections from structures present in the channel. These reflections or multipath signals interfere/overlap with the transmitted information signal and cause errors in the reception of the transmitted information. An extensive review of the past experimental and numerical work on multipath propagation of an UWB pulse was done by Molisch [2005]. Recent experimental work on UWB propagation inside buildings has shown that path loss and the Root Mean Square (RMS) delay spread depend strongly on the choice of center frequency and bandwidth of the transmitted UWB pulse [Malik *et al.*, 2007]. It is also experimentally demonstrated that, for a UWB radar system centered at 12.5 GHz, a bandwidth greater than 4 GHz does not cause significant improvement in ranging accuracy (< 1 cm/ GHz beyond 4 GHz) [Tarique *et al.*, 2006]. The same work also shows that the standard deviation of ranging errors can decrease about 15 times by using directional antennas. The number of resolved multipaths in common rake receivers is shown to increase linearly with bandwidth with a slope of 11 paths/GHz and falls monotonically with an increase in the center frequency [Malik *et al.*, 2004]. Numerical work on ranging accuracy of two types of UWB radar systems have shown that the selected pulse waveform has a significant impact on the distance estimation error, mainly due to bandwidth [Cardinali *et al.*, 2006]. Hence the nature of the transmitted UWB waveform and the physical properties of the propagation channel strongly influence the achievable performance of a given UWB communication, navigation or radar system.

The antennas affect the bandwidth of the radiated UWB signal. The antenna's transmission and reception bandwidth and center frequency is highly sensitive to the transmission and reception angles at each end of a communication link [Malik *et al.*, 2006]. For pulsed-UWB systems, it has also been shown that electrically small antennas are a direct source of pulse distortion [Pozar, 2003a; 2003b]. Most available UWB antennas have an octave of operational bandwidth in the main beam direction [Schantz, 2005]. The UWB signal has a 7.5 GHz bandwidth. Hence the limited bandwidth of the antenna causes zero crossings in

the transmitted and the received UWB pulse resulting in an increase in the time duration and a corresponding decrease in the bandwidth of the radiated UWB pulse.

1.4 Problem Statement and Approach

This thesis presents analysis and calculations, via measurements and numerical simulations, to quantify the dependence of the amplitude and shape of the radiated and received UWB pulse on the geometry and orientation of the transmitting antenna, propagation channel and the receiving antenna. The thesis presents bit error rate calculations of two commonly used types of UWB receivers, namely, the matched filter receiver and the rake receiver.

Two planar, microstrip UWB dipole antennas, namely the oval dipole and the cat-fish dipole antenna [Schantz, 2005], are designed and built. Independent time and frequency domain experiments are performed to measure the transfer function, band-limited impulse response, and the radiation pattern of the two UWB antennas in the anechoic chamber at the University of Alaska Fairbanks (UAF). A set of test oval dipole antennas are used to measure the band-limited impulse response of a hallway inside the Duckering building at UAF. A Finite Difference Time Domain (FDTD) code is developed to run on 8 parallel computers at the Arctic Region Supercomputing Center (ARSC) at UAF. The FDTD code was used to calculate the transient response of the antennas and the propagation channel. The calculations were compared with measurements to relate the geometry of the antenna and the channel to the properties of the radiated and received UWB signal.

A MATLAB-based numerical model was developed to calculate the effect of the antennas and the propagation channel on the bit error rate of two commonly used UWB receivers. The top level program flow is shown in Figure 1.2. The transmitted information is modulated on a sequence of UWB pulses by changing their position in time in a coherent manner. The measured band-limited impulse response of the transmitting antenna, propagation channel and the receiving antenna are convolved with the generated sequence of UWB pulses. The received signal is decoded by the receiver models. The decoded information signal is compared with the original transmitted information to calculate the bit error

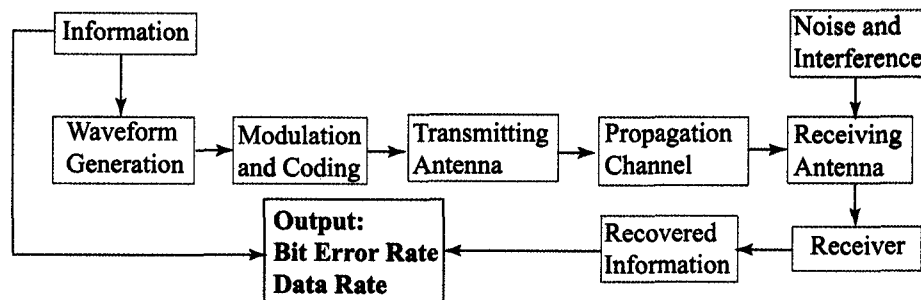


Figure 1.2. **Problem approach.** This approach was adapted from the direct-inverse problem approach used to simulate and analyze electromagnetic wave data received on a spacecraft [Sonwalkar, 1986]. The modular nature of this approach allows separate blocks to be modified independently. This approach also permits incorporating measurements to perform accurate case studies.

rate, which is the ratio of the number of received bits in error to the total number of bits transmitted.

1.5 Contributions of the Present Work

Part of the present work has been reported in three conference papers [Venkatasubramanian *et al.*, 2007; Sonwalkar *et al.*, 2007; 2006]. The specific contributions are listed as follows:

1. The transmitting and receiving properties of two microstrip UWB antennas, namely the oval dipole and the cat-fish dipole antennas, are measured in the time and the frequency domain.
2. A FDTD code is developed to run on 8 parallel computers at ARSC (UAF).
3. The reciprocity relation for constant gain UWB antennas is derived from measurements: (a) The transmitting antenna radiates the derivative of the input UWB waveform in the time domain, so the corresponding spectrum of the radiated electric field is 90° out of phase from the spectrum of the input voltage waveform. (b) The spectrum of the received voltage waveform is in phase with the spectrum of the electric field waveform incident on the antenna.

4. The oval dipole antenna has a half-power beamwidth of 80° in the vertical plane and radiates uniform pulse properties (e.g., pulse width, cycle time) within 5% in the vertical plane for a broad beamwidth of $\sim 60^\circ$ on either side of the broadside direction (90°).
5. FDTD simulations of the amplitude and the direction of the currents on the surface of an oval dipole are related to the nature of the radiated electric field waveform. The effect of the axial ratio of the ellipse on the impedance bandwidth of the antenna is presented. It is shown that as the axial ratio increases, the antenna presents a higher input impedance and hence is poorly matched to 50Ω .
6. A new theoretical model for UWB pulse propagation in the presence of a single reflecting surface is developed and the nature of the radiated UWB pulse and the physical properties of the propagation channel are related to the peak amplitude of the received signal at the receiver. Two new distance scales are proposed and are named breakpoint distances.
7. Frequency domain measurements of band-limited impulse response for line-of-sight and non-line-of-sight propagation in a hallway and a room are performed. The measurements show a clustering of multiple propagation paths. The peak amplitude of the pulse arriving through multiple propagation paths show an exponential decay. Both of these features that are observed in the data agree with the Saleh-Valenzuela model [Saleh and Valenzuela, 1987]. The measurements are compared with the FDTD simulations and show excellent agreement for the first few (< 5) dominant propagation paths.

1.6 Organization of the Dissertation

The organization of this dissertation is as follows: The first chapter discusses the objective of this research work, the significance of the stated research problem in light of the work done in the past and the approach adopted in this dissertation. The second chapter presents

the measurements and simulations of the transient response of two UWB microstrip dipole antennas to relate the geometry of the antenna to the properties of the radiated and received waveform. Chapter three presents the measurements and simulations of UWB pulse propagation in an empty parking lot and in a cluttered hallway and room. Chapter four presents a MATLAB-based numerical model of two UWB receivers to calculate the bit error rate and data rate of the receivers for specific antennas and propagation channel. Chapter five summarizes the results and discusses future directions for research.

Chapter 2 UWB Dipole Antennas: Experiments and Numerical Simulations

2.1 Objective and Significance

The objective of this chapter is to relate, via measurements and numerical simulations, the physical properties (e.g., geometry, size) of two planar, microstrip UWB antennas to the nature (e.g., shape, duration) of the radiated electric field and received voltage waveform. Independent time and frequency domain experiments are performed to measure the band-limited transfer function, band-limited impulse response, impedance and radiation pattern of the two UWB antennas. A parallel FDTD code is used to calculate the time evolution of the first derivative of the vertical component of the current on the antenna surface. The calculated current direction and distribution is related to the nature of the radiated electric field. Implications of this work towards communication and navigation applications are discussed.

The broad bandwidth (> 500 MHz) of a UWB signal causes electrically small wire antennas to considerably distort the radiated UWB pulse [Pozar, 2003a]. Most UWB antennas, with the exception of some designs like Transverse Electromagnetic (TEM) horns,

are a source of distortion for UWB pulses due to the variation of their transfer function with frequency [Scholtz and Win, 1997]. The pulse distortion of typical UWB antennas is strongly dependent on the angle of radiation or reception [Sorgel and Wiesbeck, 2005]. This is because the angular variation of the radiation pattern of an UWB antenna is frequency dependent. Recent measurements show that the transmission bandwidth of the radiated UWB signal is severely limited in some directions, and the signal energy is lost in undesired frequency bands as the look angle of the antenna moves off the broadside direction [Malik *et al.*, 2006]. This causes interference with other narrow bandwidth systems. Hence the transmitting and the receiving UWB antenna transfer function in different directions needs to be accurately quantified. To some extent, this distortion can be avoided by the use of adaptive templates [Taha and Chugg, 2002] and pulse shaping filters [McLean *et al.*, 2005] in correlation receivers. Pozar [2003b] proposed a method to optimize the generated UWB signal properties to achieve maximum output energy or peak amplitude of the received voltage waveform. Though past work has been done on measurement of the impulse response of certain specific UWB antennas as a function of radiation or reception angle [Qing *et al.*, 2006; Mehdipour *et al.*, 2007], there is little work done [Schantz, 2005] in developing a general framework to relate the antenna physical properties (e.g., geometry, size) to its impulse response via measurements and numerical simulations. This is the focus of the research presented here.

The first section of this chapter discusses the objective and significance of the antenna work presented in light of work done in the past. The second section discusses the antenna measurements performed and the measurement results. The third section describes the simulation and validation of the FDTD code developed at UAF. The fourth section describes the simulation of an oval dipole antenna and compares the measurements with simulations. The fifth section summarizes the results presented in this chapter. The sixth section discusses the implications of this work for UWB communication, navigation and radar applications and the seventh section presents concluding remarks.

2.2 Experiments

This section presents the UWB antenna experiments performed inside the anechoic chamber at the University of Alaska Fairbanks. Two planar microstrip dipole antennas are designed and their time domain and frequency domain properties are measured. A Vector Network Analyzer (VNA) is used to measure the frequency domain transfer function, input impedance and radiation pattern of the two antennas from 300 kHz to 9 GHz. A Digital Sampling Oscilloscope (DSO) is used to measure the received voltage waveform for a pair of UWB antennas. The rest of this section will discuss the experimental setup, instrumentation, signal processing algorithms used and finally the experimental results.

2.2.1 Experimental Setup and Instrumentation Description

A measurement campaign was conducted in spring and summer of 2006 to measure the radiation and reception properties of two UWB planar microstrip dipole antennas in the UAF anechoic chamber. Independent time domain and frequency domain measurements were performed. Figures 2.1A and 2.1B show the coordinate system and the definition of the antenna orientation angles θ and ϕ that are used in the experiments presented in this section. The subscripts t and r are used for the transmitting and the receiving antenna respectively.

Figure 2.2A shows the experimental setup for the frequency domain measurements. A pair of antennas aligned along the z -axis (local vertical) with their broadside directions facing one another, and placed inside the anechoic chamber, are connected to the two ports of an Agilent E8358A PNA series vector network analyzer (VNA). When the two ports of the VNA are connected to calibrated 50Ω loads via test cables, the source power set to +10 dBm, and the intermediate frequency (IF) bandwidth set to 1 kHz, the measured noise floor of the VNA for the scattering parameter measurements is -98 ± 2 dBm in the 3 GHz to 9 GHz frequency range. A detailed discussion of the noise floor of the VNA is presented in Appendix A.1.

Figure 2.2B shows the experimental setup for the time domain measurements. Also

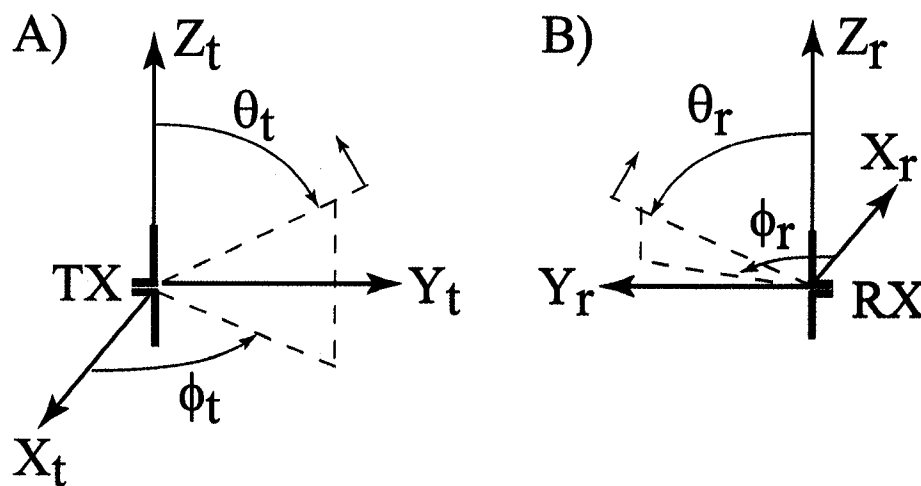


Figure 2.1. **Transmitting and receiving antenna coordinate system.** (A) The plane containing the antenna is defined as the z_t - x_t plane and the normal vector to the plane is the y_t -axis. The z_t -axis is along the local vertical. The elevation angle θ_t is defined from the z_t -axis with 0° (end fire) along the z_t -axis and 90° (broadside) along the y_t -axis. The azimuth angle ϕ_t is defined from the x_t -axis with 0° along the x_t -axis and 90° along the y_t -axis. (B) Receiving Antenna coordinate frame is the same as the transmitting antenna coordinate frame except that it is rotated by 180° about the z_r -axis. The azimuth and elevation angles, θ_r and ϕ_r are defined from the z_r -axis and the x_r -axis, respectively.

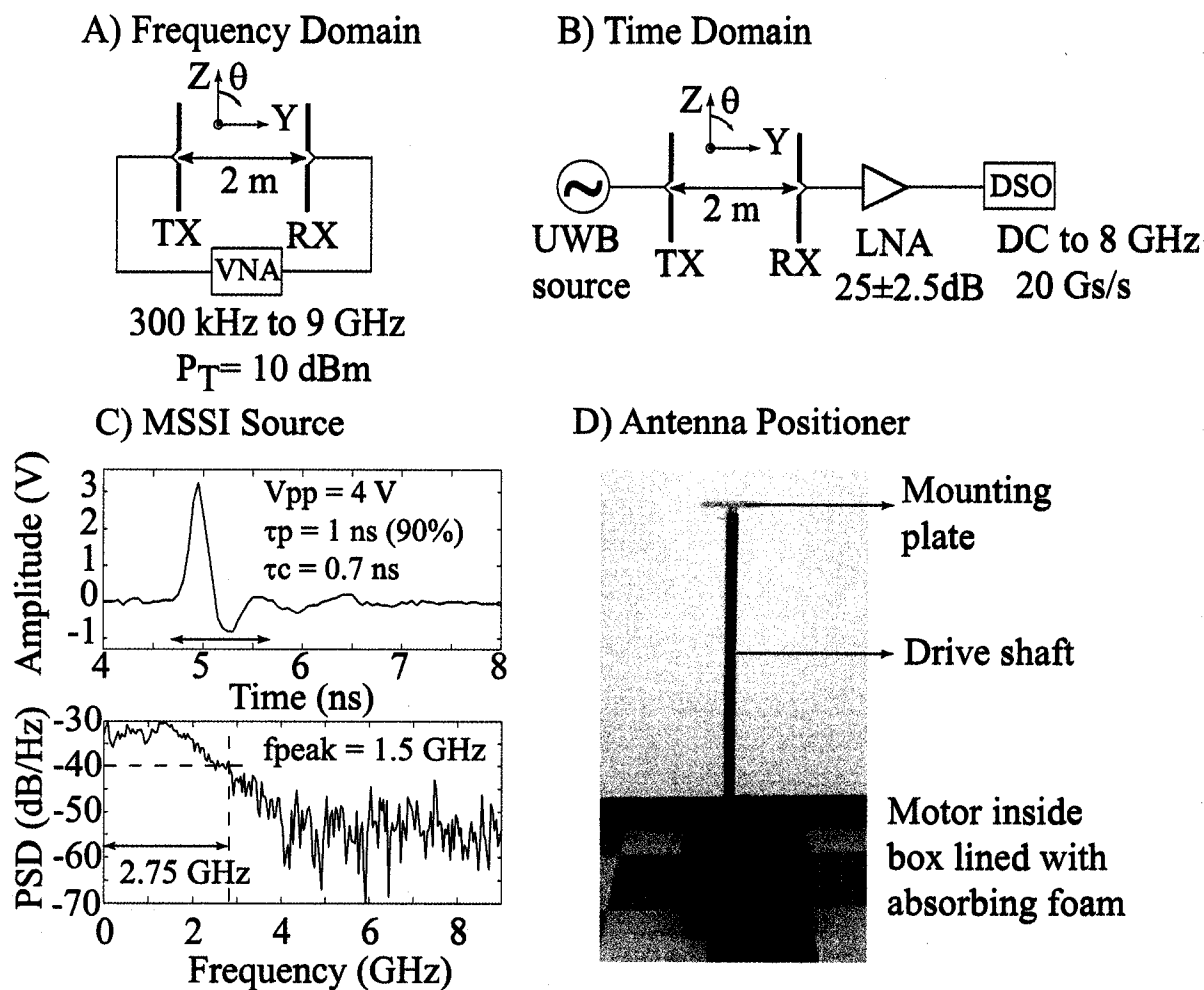


Figure 2.2. Experimental setup and instrumentation used for antenna measurements in the time and frequency domain. (A) Frequency domain measurement. (B) Time domain measurement. (C) Time domain waveform and frequency spectrum of a Multispectral Solutions, Inc. (MSSI) TFP1001 UWB source. The peak-to-peak amplitude of the time domain waveform after 5 dB attenuation (to prevent gain clipping) is 4 V. The peak positive amplitude before the 5 dB attenuator is 10.24 V, corresponding to a peak power level of 2.1 Watts (+33 dBm). The MSSI source is operated by a 15 MHz clock resulting in a duty cycle of 1%. Hence the average power into a 50 Ω load is less than 20 mW. (D) One-axis antenna positioner built at UAF.

shown in the figure is the coordinate system used for the antenna experiments presented in this thesis. The transmitting antenna is connected to a Multi Spectral Solutions Inc. (MSSI) TFP1001 impulse source whose time and frequency domain properties are shown in Figure 2.2C. The receiving antenna, 2 m away from the transmitting antenna, is connected to a Tektronix TDS 6804B digital storage oscilloscope (DSO) via a Miteq AFS3-0200600-15-LN low noise amplifier (LNA). The LNA has a nominal gain of 25 ± 2.5 dB and a noise figure of 1.6 dB in the 2 GHz to 8 GHz frequency range. The DSO measures the received voltage waveform from DC to 8 GHz with a maximum sampling rate of 20 Gs/sec. A detailed discussion of the vertical resolution and sensitivity of the DSO is presented in Appendix A.2.

Figure 2.2D shows a picture of a one-axis antenna positioner that was developed in-house at UAF. The positioner is controlled by a program running under Windows 2000 on the VNA. The drive shaft and mounting plate of the positioner are made from non-metallic materials to minimize unwanted reflections. The antenna positioner is used to measure the radiation pattern of the UWB antennas in the time and frequency domains.

Figure 2.3 shows a picture of two types of UWB reference antennas used in the experiments presented in this thesis. The Sunol broadband DRH 118 horn antennas, shown in Figure 2.3A, have a wide bandwidth from 1 to 18 GHz and a gain of 10 ± 1.5 dB for minimal distortion of the received spectrum. The horn antenna is 28 cm long by 15 cm wide and offers an angular resolution of $\sim 4^\circ$ in the vertical plane for radiation pattern measurements. These antennas are used as reference antennas to measure the time and frequency domain behavior of the antenna under test (AUT). The Time Domain Corporation Broadspec[®] P200 antennas, shown in Figure 2.3B, have an operational bandwidth from 3 GHz to 8 GHz and are omni-directional with a gain of 2.2 dBi. They are used as probe antennas for the chamber calibration measurements discussed in Appendix A.3.

Figure 2.4 shows the UWB microstrip dipole antennas designed and built at UAF. Figures 2.4A and 2.4B show pictures of the oval and the cat-fish dipole antennas. The dimensions of the ovals were also chosen based on past work [Schantz, 2001]. The cat-fish

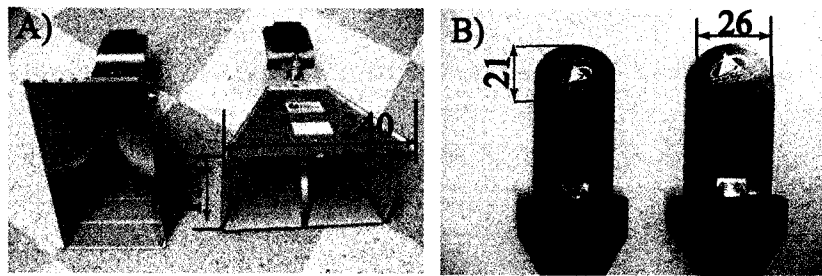


Figure 2.3. **UWB Reference antennas.** (A) Sunol Sciences DRH-118 broadband horn antennas (B) Time Domain Corporation Broadspec® P200 antennas.

dipole is an exact replica of the commercial Time Domain Broadspec® P200 antenna (Figure 2.3B). The oval and the cat-fish dipole antennas were chosen because of their omnidirectional pattern uniform over a broad bandwidth (> 2 GHz), scalability to higher frequency ranges and linear polarization [Schantz, 2005]. The experimental procedure to measure the time and frequency domain properties of these antennas will be discussed next.

A) Oval Dipole

B) Cat-Fish Dipole

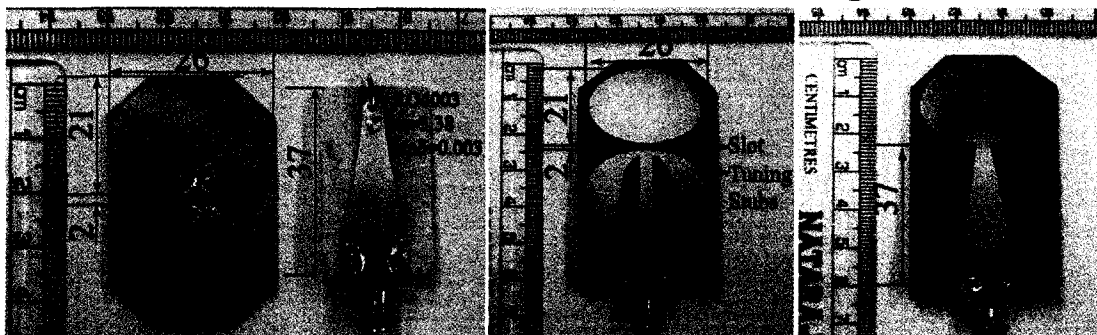


Figure 2.4. **Pictures of the UWB microstrip dipole antennas built at UAF.** (A) Oval dipole (B) Cat-Fish dipole. The 26 X 21 mm radiating oval is placed on the left and the 37 mm long tapered balun is placed on the right. All the dimensions shown are in millimeters. The balun design was based on the PulsON200TM antenna feeding structure [Schantz, 2003]. The radiating elements on either side of the antenna are electrically connected by vias milled onto the antenna (not shown in figure).

2.2.2 Frequency Domain Scattering Parameter Measurements

2.2.2.1 Broadside Transmitting and Receiving Impulse Response Measurement

The frequency domain transfer function and the time domain band-limited impulse response of a UWB antenna in the transmitting and the receiving mode is measured based on the procedure proposed by Qing *et al.* [2006]. This procedure involves a pair of “identical” antennas oriented with the same polarization so that the same parts of their radiation patterns point at each other. The two “identical” antennas are connected to a VNA inside the anechoic chamber (described earlier) as shown in Figure 2.2A. The VNA performs a swept frequency measurement of the scattering parameters of the antenna pair from 300 kHz to 9 GHz in steps of 5.6 MHz thereby, capturing a total of 1601 equally spaced measurements.

The VNA was calibrated using the Agilent electronic calibration (E-Cal) module prior to the commencement of the measurement. Calibration accuracy is confirmed using an independent set of mechanical standards. For S11 and S22 measurements, the significant analyzer error is due to the output signal reflecting back to the port at the directional coupler and the reflected signal from the device under test (DUT) that is reflected a second time at the port. After calibration, the measured reflection coefficients (S11 and S22) were within a few tenths of a dB for open and short standards, and less than -30 dB for a 50Ω load standard. The uncertainty in the measured transmission coefficients (S21 and S12) for a pair of commercial horn antennas (discussed in section 2.2.1), 2 meters apart, is < 0.2 dB in the 300 kHz to 9 GHz frequency range. The two meter separation distance between the antennas inside the chamber was chosen based on the anechoic chamber calibration measurements presented in Appendix A.3.

The transmitting antenna transfer function, $H_t(\omega, \theta_t, \phi_t)$, is defined as the ratio of the radiated electric field to the input voltage applied to the antenna terminals. The radiated electric field is normalized to the magnitude and phase of the electric field at the location of the receiving antenna in the transmitting antenna reference frame (Figure 2.1A). Hence $H_t(\omega, \theta_t, \phi_t)$ is dimensionless. The receiving antenna transfer function $H_r(\omega, \theta_r, \phi_r)$ is defined as the output voltage at the antenna terminals divided by the electric field incident on

the antenna. The direction of arrival of the incident electric field in the receiving antenna coordinate frame (Figure 2.1B) is given by (θ_r, ϕ_r) . $H_r(\omega, \theta_r, \phi_r)$ has dimensions of meters.

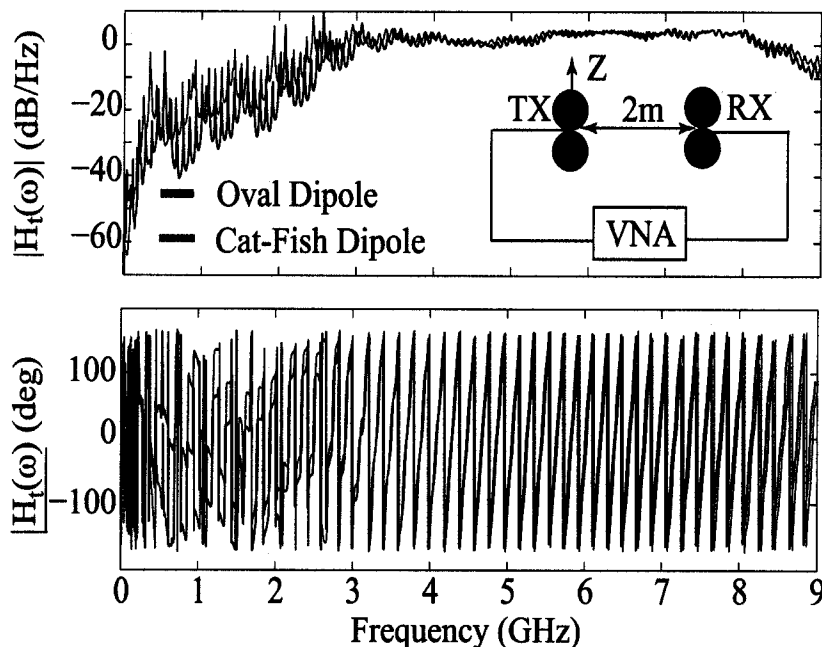


Figure 2.5. **Transmitting antenna transfer function computed for the oval and cat-fish dipole antennas.** The top panel shows the amplitude in log scale and the bottom panel shows the phase of the transmitting antenna transfer function calculated from the S21 measured for a pair of matched oval (black curve) and cat-fish (red curve) dipole antennas separated by 2 m in the anechoic chamber (shown as inset in figure).

Figure 2.5A and 2.6B show the transmitting and receiving antenna transfer functions of a pair of identical oval (black curve) and the cat-fish (red curve) dipole antennas measured using the approach detailed in Appendix A.4.1. The transfer functions are measured for 1601 positive frequency points spaced every 5.6 MHz. The inverse fourier transform of this transfer function yields a discrete time analytical signal [Iverson, 1991]. The real part of this signal yields the time domain impulse response, $h(t)$, for each pair of elevation and azimuth angles [Sorgel and Wiesbeck, 2005]. The measured impulse response has a time resolution of 284.6 ps. The time resolution is improved to 5 ps by zero padding the measured transfer function from 9 GHz to 200 GHz. The impulse response is further processed by low

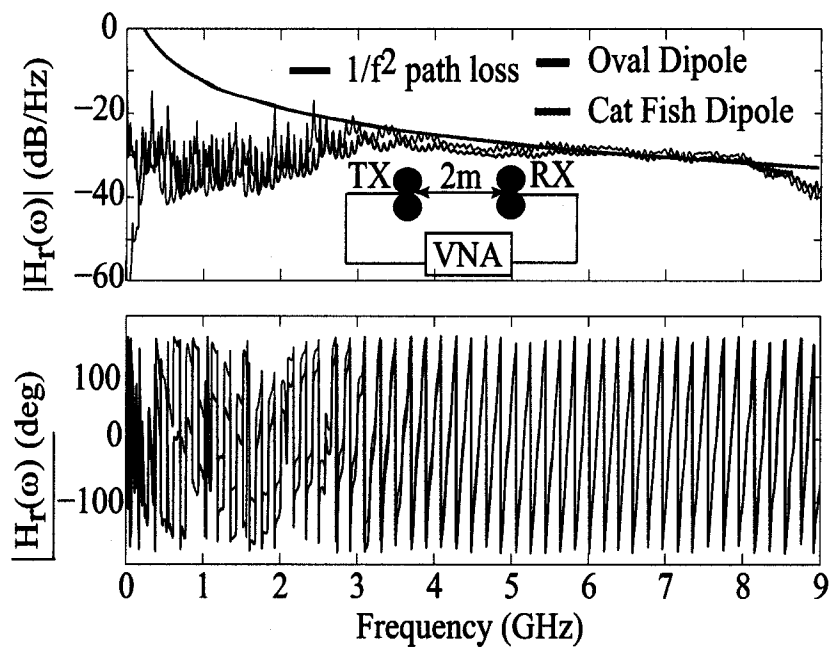


Figure 2.6. **Receiving antenna transfer function computed for the oval and cat-fish dipole antennas.** The top panel shows the amplitude in log scale and the bottom panel shows the phase of the receiving antenna transfer function calculated from the S21 measured for a pair of matched oval (black curve) and cat-fish (red curve) dipole antennas separated by 2 m in the anechoic chamber (shown as inset in figure).

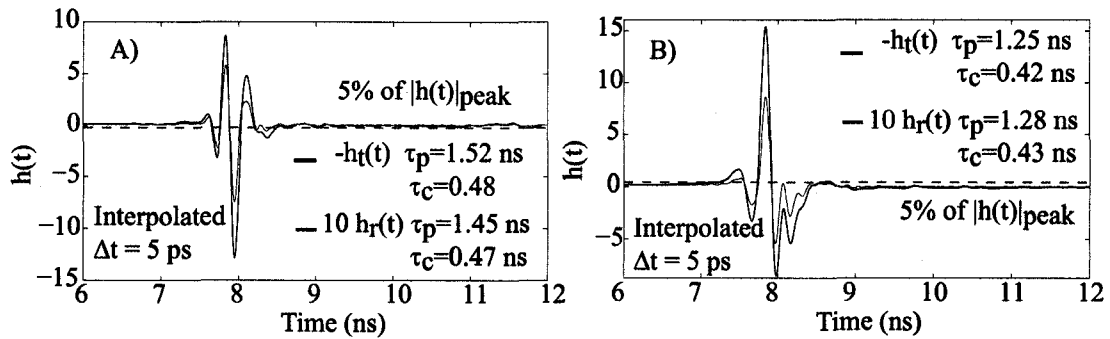


Figure 2.7. Transmitting and receiving antenna impulse response using the transfer functions calculated from frequency domain scattering parameter measurements for the oval and cat-fish dipole antennas. (A) Oval dipole. (B) Cat-fish dipole. The transmitting antenna impulse response is shown as a red curve and the receiving antenna impulse response is shown as a black curve. The receiving antenna impulse response has dimensions of meters and the transmitting antenna impulse response is dimensionless. The receiving antenna impulse response is scaled 10 times for clarity.

pass filtering the high frequency oscillations due to the sharp cut off in the measurement at 9 GHz. Figures 2.7A and 2.7B show the band-limited transmitting (black curve) and receiving (red curve) antenna impulse response of an oval and a cat-fish dipole antenna using the transfer functions shown in Figures 2.5 and 2.6.

2.2.2.2 Voltage Standing Wave Ratio (VSWR) Measurement

The scattering parameter measurement also permits the calculation of the voltage standing wave ratio which is a measure of how well an antenna is impedance-matched to a 50 Ω load. The VSWR is a real quantity and is related to the reflection coefficient $S_{11}(\omega)$ as

$$VSWR = \frac{1 + |S_{11}|}{1 - |S_{11}|}. \quad (2.1)$$

Figures 2.8 shows the VSWR for the oval (black curve) and the cat-fish (red curve) dipole antennas along with the tapered balun feed (shown in Figure 2.4) in the 300 kHz to 9 GHz frequency range. Also shown in the figure is the VSWR of the Time Domain P200 antenna, measured by Schantz [2005]. It is interesting to note that this measurement

departs from the VSWR of the cat-fish dipole which has the exact same dimensions as the P200 antenna. A VSWR of 1.5:1 is chosen which translates to a return loss of -14 dB or 4% of the energy incident on the antenna is reflected back into the port.

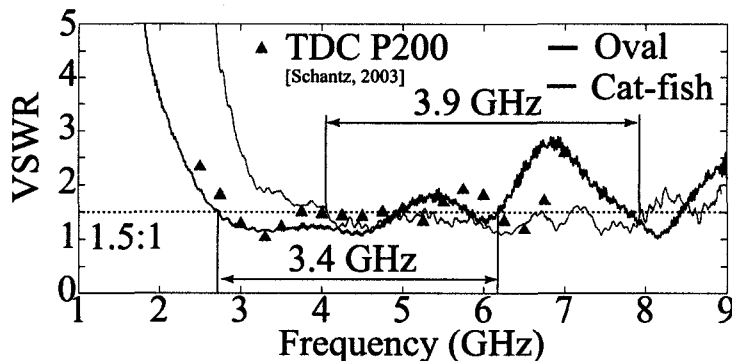


Figure 2.8. VSWR of the oval and the cat-fish dipole antennas. The black curve shows the VSWR of the oval dipole antenna which has a impedance bandwidth of 3.4 GHz from 2.75 GHz to 6.15 GHz. The red curve shows the VSWR for the cat-fish dipole antenna which has an impedance bandwidth of 3.9 GHz from 4.0 GHz to 7.9 GHz. The red triangles represent the VSWR of the TDC Broadpsec® P200 antenna, which has a impedance bandwidth of 2.75 GHz from 2.8 GHz to 5.5 GHz. These measurements were estimated from Fig 6.28 in Schantz [2005]. The VSWR for the impedance bandwidth calculation is 1.5:1 shown as a horizontal dotted line.

The cat-fish dipole antenna is a variant of the oval dipole antenna. There are two main differences between the two antennas. The first difference is that the oval dipole antenna is center fed with the balun aligned perpendicular to the plane containing the radiating elements, whereas the cat-fish dipole antenna is bottom fed with the balun in the same plane as the radiating element. This affects the near fields of the antenna and the radiated electric field at angles close to the antenna null [Schantz, 2003]. The second difference is that the oval dipole antenna has symmetrical radiating elements on either side of the feed point in the same plane, whereas the cat fish dipole has asymmetrical radiating elements with part of the bottom oval etched out to accommodate the balun structure. This causes differences in the pattern, matching (as seen in Figure 2.8), and radiated pulse properties of the two antennas. Our main objective is to relate geometry of the radiating elements to

the radiated electric field. Hence the rest of this chapter will focus only on the oval dipole antenna.

2.2.2.3 Measurement of the Cross-Polarized Antenna Response

The vector electric field vector radiated by an antenna is oriented in the plane perpendicular to the direction of propagation. The orientation of the electric field determines the polarization. The polarization characteristics of an oval dipole antenna is measured by connecting two identical ovals to the two ports of a network analyzer. The co-polarized measurement where the two ovals are identically oriented in azimuth and elevation is shown in Figure 2.5A. The cross polarized component of the electric field is measured by rotating the receiving oval in the vertical plane by 90° as shown in Figure 2.9A. Figures 2.9B and 2.9C show the transmitting and the receiving antenna co-polarized (black curve) and the cross-polarized (red curve) impulse responses for a pair of oval dipoles separated by 2 m in the anechoic chamber. The cross-polarized field components are ~ 20 dB below the co-polarized components but the pulse width of the cross polarized response is a factor of 1.5 longer than the co-polarized signal for both the transmitting and receiving antenna response.

2.2.2.4 Co-Polarized and Cross-Polarized Radiation Pattern of the Oval Dipole Antenna

The radiation pattern and the transient response of the oval dipole antenna is measured in the anechoic chamber in two orthogonal polarizations using the procedure proposed by Sorgel and Wiesbeck [2005]. Figure 2.10A shows the schematic of the experimental setup to measure the co-polarized antenna response. The oval dipole antenna and the horn antenna are connected to ports 1 and 2 of the VNA. The two antennas are aligned with their broadside direction facing each other. The oval dipole antenna is mounted on the antenna positioner (shown in Figure 2.2D) and is rotated in the horizontal plane in 5° increments. The elevation angle θ is defined from the axis of the oval antenna which is aligned along

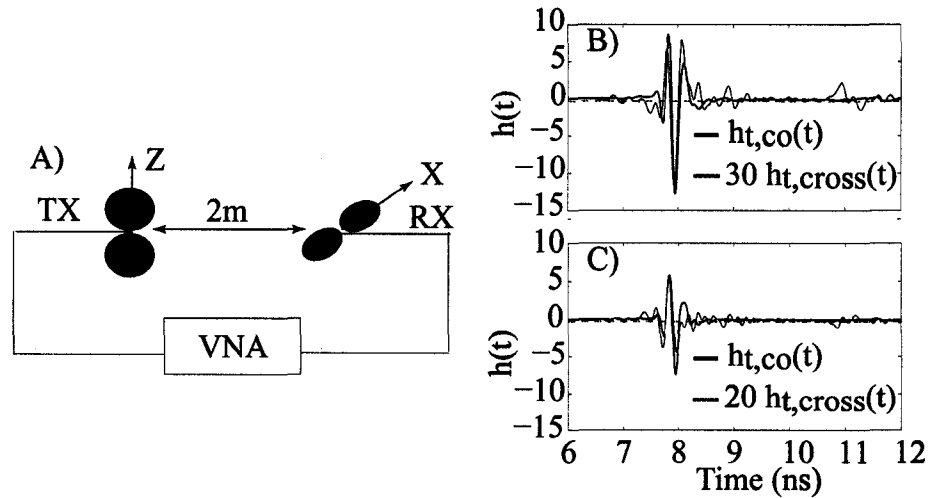


Figure 2.9. Co-polarized and cross-polarized transmitting and receiving impulse response of a pair of oval dipole antennas separated by 2 m in the anechoic chamber. (A) Experimental setup (B) Transmitting antenna impulse response. (C) Receiving antenna impulse response.

the local vertical. The $\theta = 90^\circ$ corresponds to the broadside direction and the $\theta = 0^\circ$ corresponds to the end-fire direction. The horn is held fixed 2 m away throughout the measurement.

The co-polarized and cross-polarized transfer functions of the oval dipole antenna for each pair of elevation and azimuth angles are calculated from the measured forward transmission coefficient S_{21} using the relation

$$S_{21}(\omega, \theta, \phi) = H_{ref}(\omega, 90, 90)H_t(\omega, \theta, \phi)\frac{j\omega}{2\pi Rc}e^{j\omega R/c} \quad (2.2)$$

where $H_{ref}(\omega, 90^\circ, 90^\circ)$ is the broadside receiving transfer function of the horn antenna and $H_t(\omega, \theta, \phi)$ is the transmitting antenna transfer function of the oval dipole antenna. The measured broadside transfer function of the horn antenna, shown in Appendix A.3, is used to calculate the transfer function of the oval antenna from Equation 2.2.

Figures 2.10C and 2.10D show the co-polarized oval antenna transfer function for three elevation and azimuth angles respectively. The -10 dB bandwidth of the transfer function is

3.5 GHz in the vertical plane and its variation remains within 5% up to an elevation angle of 33° . In the horizontal plane the bandwidth of the transfer function remains within 5% for all the azimuthal angles. Note that the negative slope in the transfer function is due to the $1/f^2$ path loss, shown as a black dotted line. The algorithm adopted to calculate the time duration, number of zero crossings, bandwidth, and center frequency of a waveform is discussed in Appendix B.1. For $\theta = 0^\circ$, $f_c = 1.8$ GHz, $B = 400$ MHz and with $\theta = 90^\circ$, $f_c = 4.2$ GHz, $B = 3.5$ GHz. For $\phi = 0^\circ$, $f_c = 4.2$ GHz, $B = 3.5$ GHz and with $\phi = 90^\circ$, $f_c = 4.2$ GHz, $B = 3.3$ GHz. This shows that the properties of the radiated pulse are strongly dependant on the orientation of the transmitting and receiving antenna.

Figure 2.10E shows the band-limited impulse response of the oval dipole antenna for $\theta = 0^\circ$, 30° , and 90° . The impulse response duration remains within 5% of the broadside direction value up to $\theta = 33^\circ$. Beyond this angle, the duration of the impulse response is elongated by a factor of two at $\theta = 30^\circ$ and a factor of six along the antenna axis ($\theta = 0^\circ$) compared to the response in the broadside direction ($\theta = 90^\circ$). Figure 2.10F shows the band-limited impulse response of the oval dipole antenna for $\phi = 0^\circ$, 30° , and 90° . The duration of the impulse response is within 5% of the $\phi = 0^\circ$ waveform time duration, which is ~ 2.5 ns.

Thus far all the experiments presented have measured the co-polarized components such as the results shown in Figure 2.10. The experimental setup for the measurement of the cross-polarized components in the vertical and horizontal plane is similar to Figures 2.10A and 2.10B except that the receiving horn antenna is rotated by 90° on its axis. Figures 2.11A and 2.11B show the cross-polarized oval antenna transfer function for three elevation and azimuth angles, respectively. The amplitudes are 15 dB down from the co-polarized amplitudes for the same three elevation angles (shown in Figures 2.10C and 2.10D). Figures 2.11C and 2.11D show the corresponding cross-polarized band-limited impulse response. The peak amplitude is down by a factor of 10 and the pulse width increases by a factor of 5 in comparison with the co-polarized components for the same azimuth and elevation angles (shown in Figures 2.10E and 2.10F). The polarization ratio is the peak amplitude

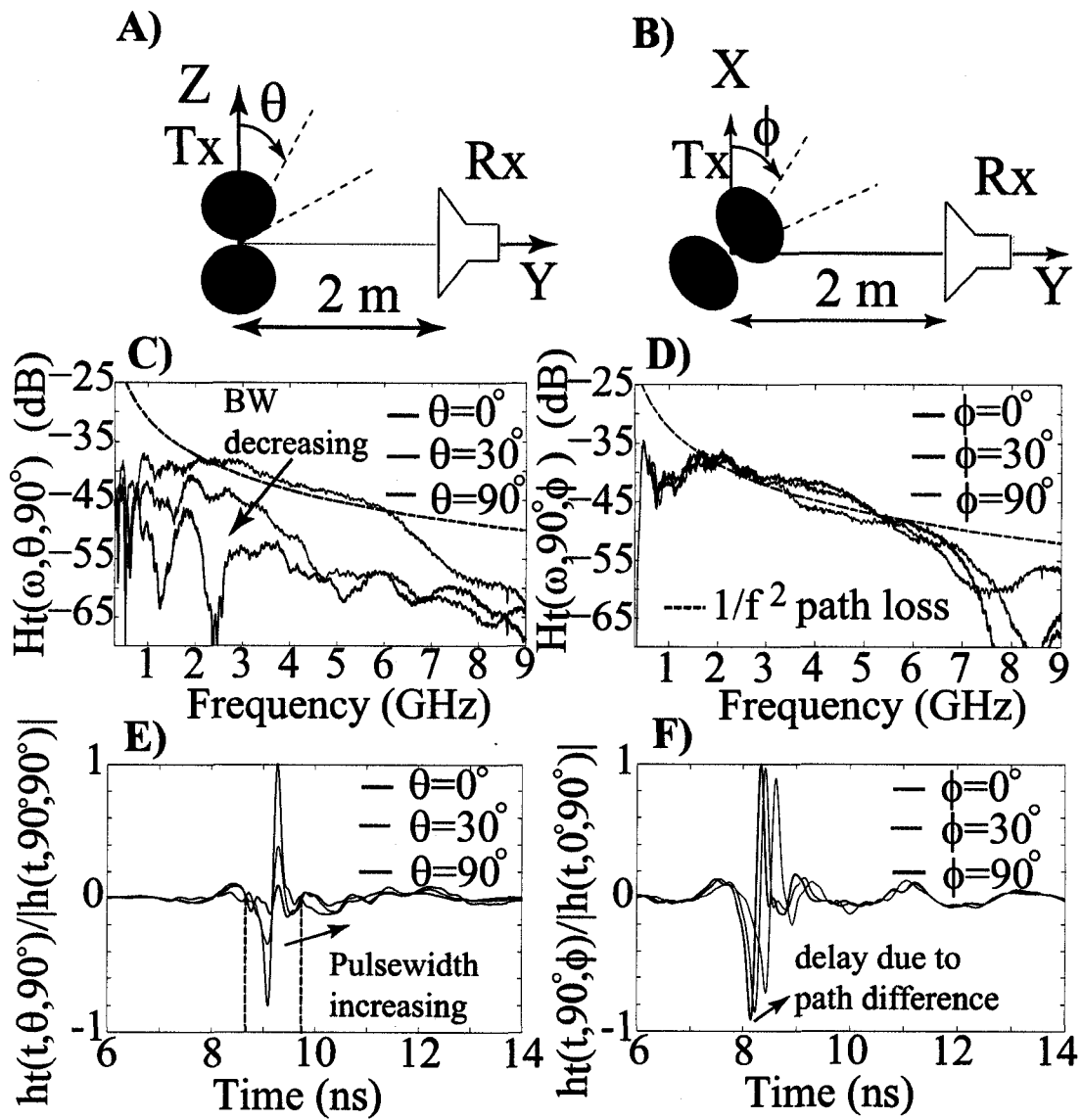


Figure 2.10. Directional dependence of the co-polarized components of the oval dipole antenna transfer function and impulse response. (A) Experimental setup to measure the variation of antenna response with elevation angle θ . (B) Experimental setup to measure the variation of antenna response with azimuth angle ϕ . (C) Transmitting antenna transfer function for $\theta = 0^\circ, 30^\circ, 90^\circ$. (D) Transmitting antenna transfer function for $\phi = 0^\circ, 30^\circ, 90^\circ$. (E) Band-limited impulse response for $\theta = 0^\circ, 30^\circ, 90^\circ$. (F) Band-limited impulse response for $\phi = 0^\circ, 30^\circ, 90^\circ$.

of the cross-polarized band-limited impulse response divided by the peak amplitude of the co-polarized band-limited impulse response. These measurements suggest that the oval antenna has good polarization purity with 15 dB difference between the co-polarization to cross-polarization components. The maximum polarization ratio is 0.55 along the $\theta = 0^\circ$ null and the minimum is 0.06 along the $\theta = 90^\circ$ (broadside) direction.

Figure 2.12 shows the peak amplitude of the co-polarized (black) and the cross-polarized (gray) impulse response of the oval dipole in the vertical (curve) and the horizontal plane (diamonds). The oval antenna has a dipole like pattern in the vertical plane with the maximum shifted to $\sim 85^\circ$. The oval antenna has an omnidirectional pattern with a front to back ratio of 0.8 in the vertical plane. The asymmetry in the vertical plane is due to the geometry of the oval antenna and is exaggerated by the balun structure, which is asymmetrical on either side of the antenna and orthogonal to the plane containing the antenna. The cross polarization radiation pattern is dipole-like in the horizontal plane but rotated by 33° with its maximum at 115° and -75° respectively. In the vertical plane, the pattern is smeared out with a maximum at -110° .

2.2.3 Time domain Measurement of the Received Voltage Waveform

As discussed in Figure 2.2B, the time domain measurement involves exciting the antenna under test (AUT) with an MSSI UWB source (Figure 2.2C) and measuring the voltage received by a commercial horn antenna 2 m away using a DSO. The details of the DSO are discussed in section 2.2.1. Two signal processing algorithms are used to de-convolve the impulse response of the test antenna: (1) sensor-CLEAN algorithm [Cramer *et al.*, 1999] and (2) Van-Citteret algorithm [Bennia and Riad, 1992] discussed in Appendix A.4.2.

Figure 2.13A shows the experimental setup for the time domain measurement. Figure 2.13B shows the received voltage waveform, as a red curve, for a pair of horn antennas separated by 2 m in the anechoic chamber. The MSSI source waveform is shown as a black curve. Also shown, as a blue curve, is the received voltage waveform calculated by multiplying the transmitting and the receiving transfer function of the horn antenna,

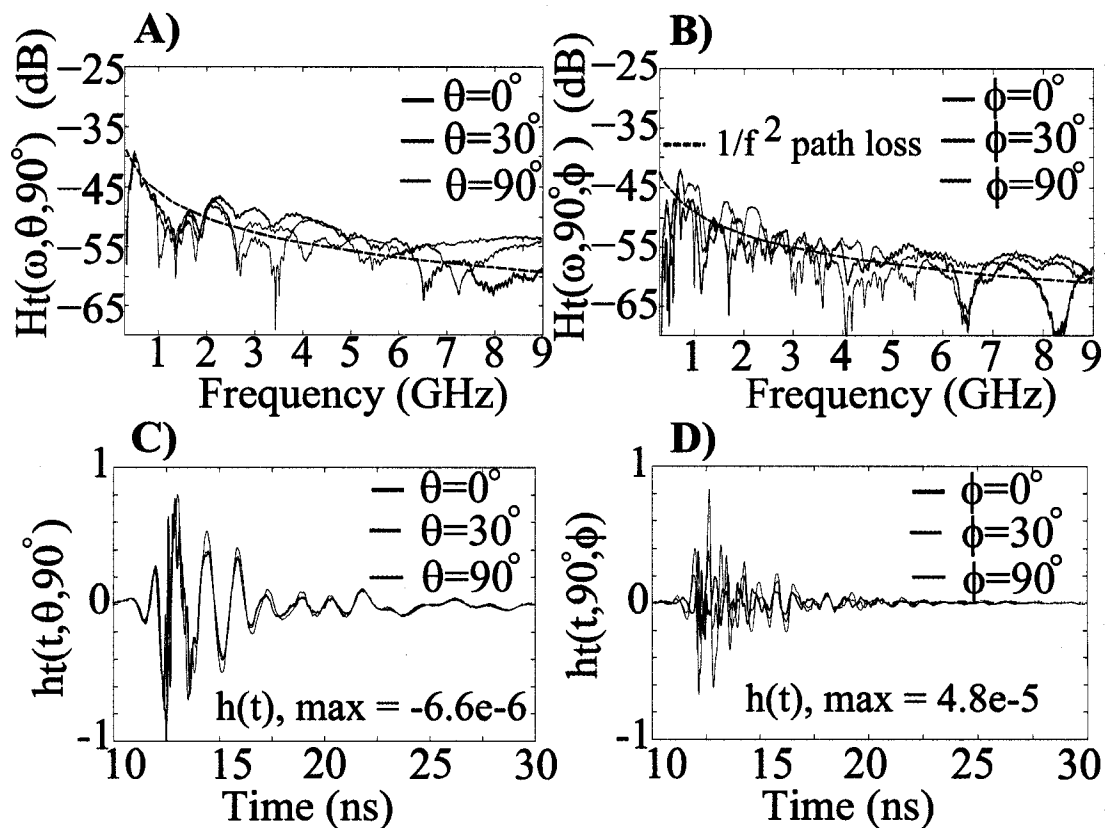


Figure 2.11. Directional dependence of the cross-polarized components of the oval dipole antenna transfer function and impulse response. (A) Transmitting antenna transfer function for $\theta = 0^\circ, 30^\circ,$ and 90° . (B) Transmitting antenna transfer function for $\phi = 0^\circ, 30^\circ,$ and 90° . (C) Band-limited impulse response for $\theta = 0^\circ, 30^\circ,$ and 90° . (D) Band-limited impulse response for $\phi = 0^\circ, 30^\circ,$ and 90° .

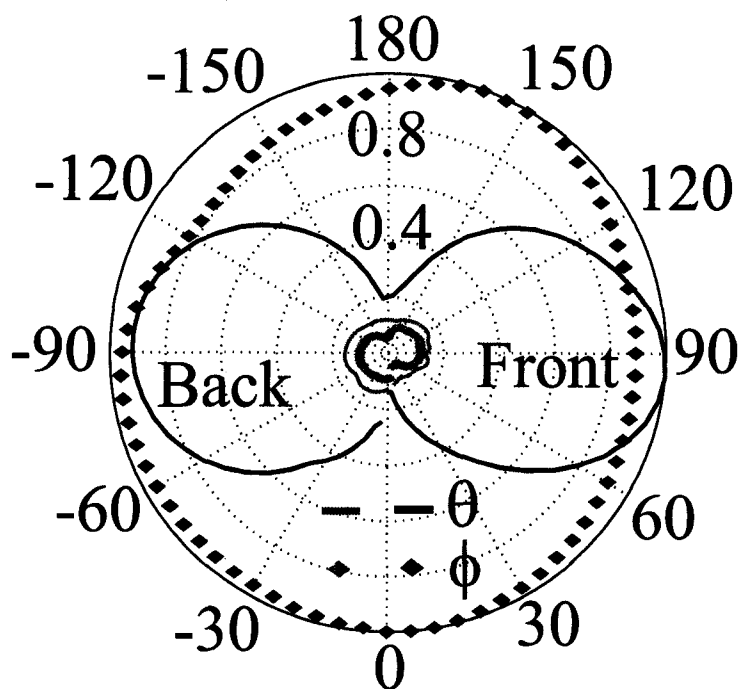


Figure 2.12. Radiation pattern of the oval dipole antenna in the vertical and horizontal planes. The variation of the peak amplitude of the impulse response of the oval antenna as a function of elevation and azimuth angles are shown as a black curve and black diamonds respectively for vertical polarization and as a gray curve and diamonds respectively for horizontal polarization. The positive elevation angles from 0° to 180° denotes radiation directions in front of the antenna and the negative elevation angles denote the directions behind the antenna. Note that measurements are made from 0° to 180° and then from -180° to -5° . hence there is a missing data point shown by a gap in the pattern curve. The -3 dB beam width of the oval antenna is $67^\circ \pm 2^\circ$.

measured by the VNA, with the frequency spectrum of the MSSSI source. The primary cycle of the two waveforms show fair agreement, but the VNA measurement shows additional ringing. Figure 2.13C shows the frequency spectrum of the DSO (red curve) and VNA (blue curve) measurement of the received voltage waveform. Also shown as a black curve is the spectrum of the MSSSI source signal. The received voltage waveform calculated from the frequency domain measurement has a lower center frequency compared to the time domain measurement. The spectrum of the DSO and VNA measurement align at the peak frequency of the MSSSI source, which is 1.6 GHz. The VNA measured spectrum closely follows the spectrum of the MSSSI source up to 4.5 GHz, suggesting that all the energy supplied to the antenna up to this frequency is radiated. The DSO measured spectrum shows a sharper fall off compared to the VNA measurement and has a narrower bandwidth.

Figure 2.14A shows the experimental setup for the time domain measurement. Figure 2.14B shows the received voltage waveform measured by the DSO (red curve), for a pair of oval dipoles separated by 2 m in the anechoic chamber. Also shown, as a black curve, is the received voltage waveform calculated by multiplying the transmitting and the receiving transfer function of the oval dipoles with the frequency spectrum of the MSSSI source (shown in Figure 2.2C). The primary cycle of the two waveforms show good agreement, but the frequency domain measurement shows additional ringing because most of the energy of the MSSSI source lies in the DC to 3 GHz bandwidth, whereas the transmission bandwidth of the oval antenna is from 2 GHz to 6.5 GHz. Also, the time domain measurement has additional 25 ± 2.5 dB gain owing to a LNA connected to the receiving antenna terminals. The details of the LNA are discussed in section 2.2.1. This additional gain provides ample signal to be well above the noise floor of the DSO in the time domain measurements. Figure 2.14C shows a comparison of the broadside spectrum of the received voltage waveform measured using the DSO (red curve) and the VNA (blue curve).

The radiation pattern of the oval dipole antenna is measured by mounting the oval on an antenna positioner, which rotates the antenna first in the vertical plane from 0° to 180° and then from -180° to 0° elevation angle. The oval antenna is connected to an MSSSI

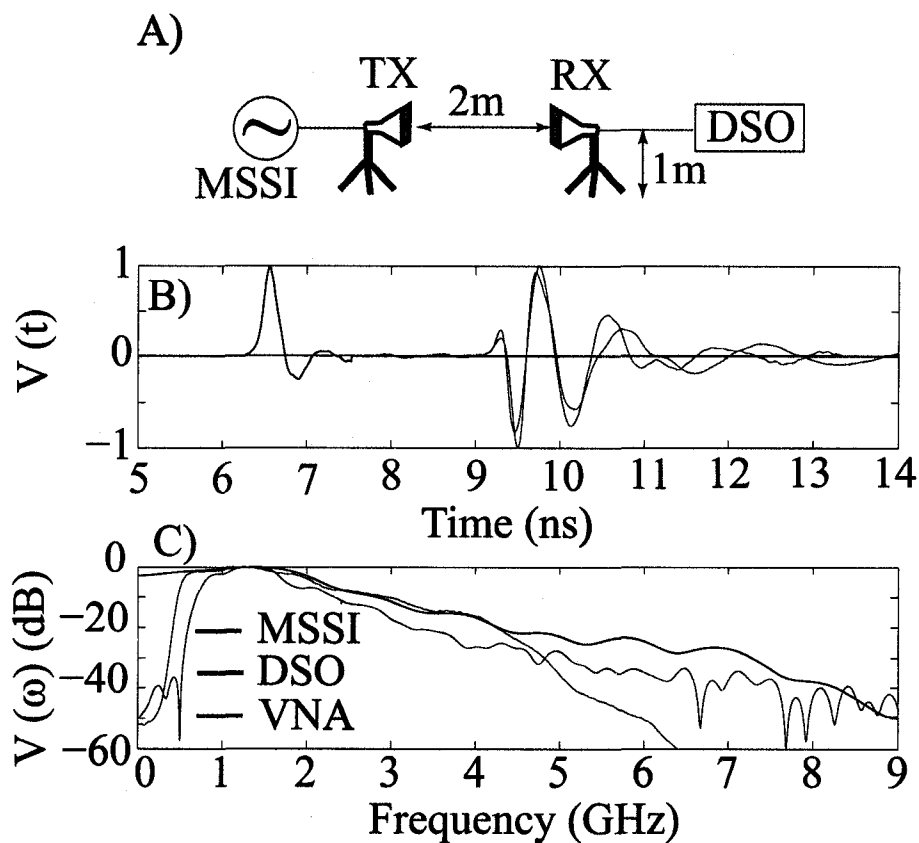


Figure 2.13. Time and frequency domain measurement of the received voltage waveform for a pair of identical horn antennas. (A) The experimental setup for the time domain measurement. (B) The blue curve shows the transmitting and the receiving transfer function of the horn antennas, measured using VNA, and multiplied with the spectrum of the MSSSI source. The resulting frequency domain signal is inverse fourier transformed to get the time domain waveform. This is compared with the voltage waveform directly measured at the terminals of the receiving antenna using a DSO, shown as a red curve. The MSSSI source waveform is shown as a black curve. (C) The frequency domain spectrum of the received voltage waveform measured using the time domain (red curve), frequency domain (blue curve) and the MSSSI source waveform (black curve).

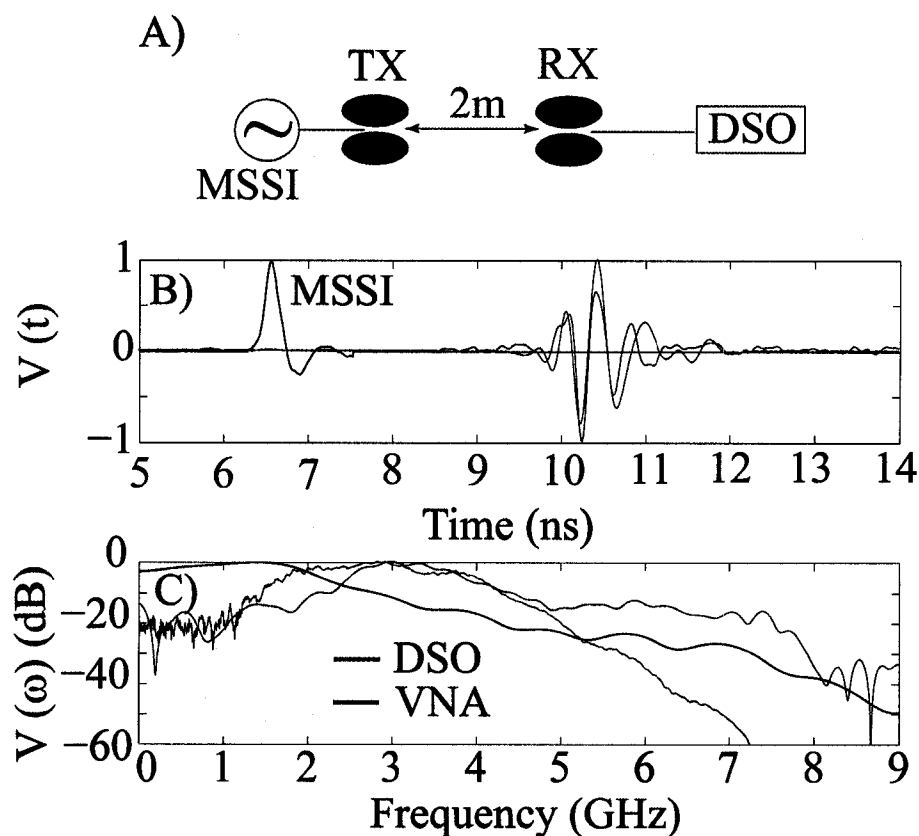


Figure 2.14. Time and frequency domain measurement of the received voltage waveform for a pair of identical oval antennas. (A) The experimental setup for the time domain measurement. (B) The blue curve shows the transmitting and the receiving transfer function of the horn antennas, measured using VNA, and multiplied with the spectrum of the MSSSI source. The resulting frequency domain signal is inverse fourier transformed to get the time domain waveform. This is compared with the voltage waveform directly measured at the terminals of the receiving antenna using a DSO, shown as a red curve. The MSSSI source waveform is shown as a black curve. (C) The frequency domain spectrum of the received voltage waveform measured using the time domain (red curve), frequency domain (blue curve) and the MSSSI source waveform (black curve).

source. The electric field radiated by the oval dipole is received by a horn antenna 2 m away with its broadside direction facing the oval antenna. The received voltage is amplified using a low noise amplifier and then measured on a DSO. The transmitting oval antenna impulse response is de-convolved using the measured broadside receiving transfer function of the horn antenna and the spectrum of the MSSSI source waveform. The time domain results are presented later in section 2.3.

2.3 Finite Difference Time Domain Simulations

This section discusses the 3D FDTD simulation code that was developed to calculate the transient response of UWB antennas and the propagation of UWB signals. The FDTD method was chosen because: (1) It is a time domain method. (2) It is easily scalable for multiple domain sizes. (3) The code structure is amenable to parallelization permitting simulation of large (> 1 GB storage space) domain sizes. There are several FDTD approaches known [Sullivan, 2000]. The implemented code uses a second-order, centered difference approach known as Yee's algorithm on a uniform mesh of points [Yee, 1966].

This section will begin with a brief discussion of the FDTD method, followed by optimization and parallelization of the FDTD code to run on the supercomputers available through the Arctic Region Supercomputing Center (ARSC) at UAF and finally the simulation of a few test cases.

2.3.1 Mathematical Formulation

The integral and differential form of Maxwell's equations are [Taflove, 1995]

$$\begin{aligned}
 \oiint (\vec{D} \cdot \vec{n}) d^2 A &= Q_{\text{free, included}} & \nabla \cdot \vec{D} &= \rho_{\text{free}} \\
 \oiint (\vec{B} \cdot \vec{n}) d^2 A &= 0 & \nabla \cdot \vec{B} &= 0 \\
 \oint \vec{E} \cdot d\vec{s} &= -\frac{d\Phi}{dt} & \nabla \times \vec{E} &= -\frac{\partial \vec{B}}{\partial t} \\
 \oint \vec{H} \cdot d\vec{s} &= I_{\text{free, included}} + \frac{d\Psi}{dt} & \nabla \times \vec{H} &= \vec{J}_{\text{free}} + \frac{\partial \vec{D}}{\partial t}
 \end{aligned}$$

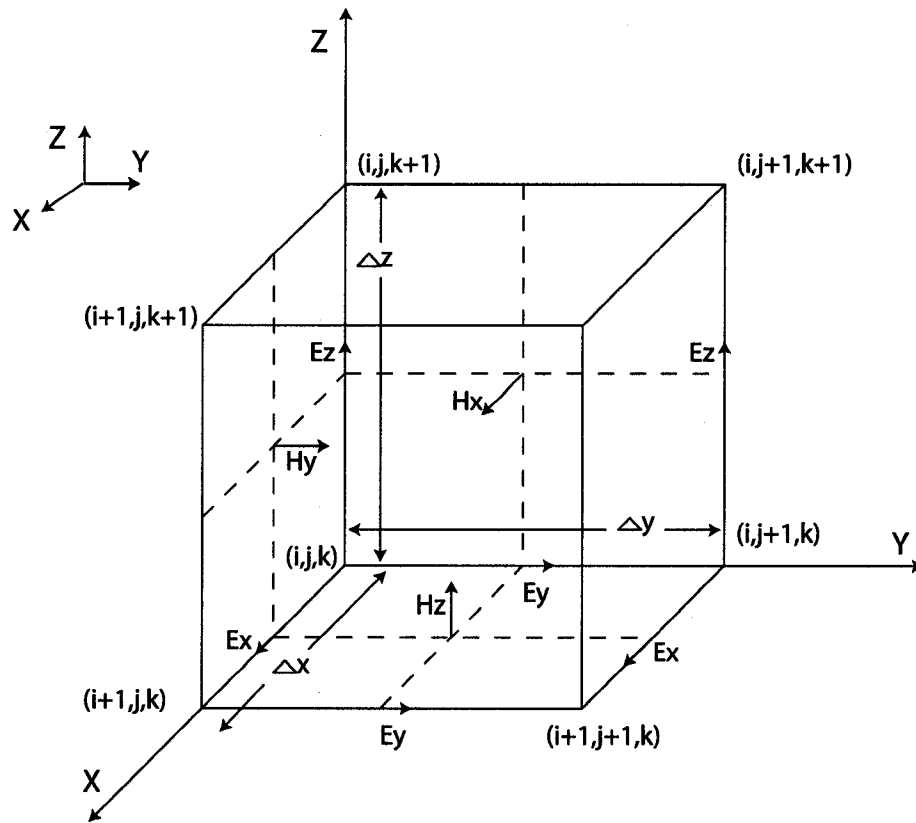


Figure 2.15. Position of the field components on a single Yee cell. The problem space is divided into cubes called Yee Cells. In the cartesian coordinate system, each Yee cell contains six field components, \vec{E}_x , \vec{E}_y , \vec{E}_z , \vec{H}_x , \vec{H}_y and \vec{H}_z . The fields are all arranged in a staggered grid and are offset by half a step in the spatial domain as shown in the diagram.

$$\text{For the fluxes holds: } \Psi = \iint (\vec{D} \cdot \vec{n}) d^2 A, \quad \Phi = \iint (\vec{B} \cdot \vec{n}) d^2 A.$$

The electric displacement \vec{D} , and electric field strength \vec{E} depend on each other according to $\vec{D} = \epsilon_0 \epsilon_r \vec{E}$, where ϵ_0 is the permittivity of free space and ϵ_r is the permittivity of a medium. The magnetic field strength \vec{H} , the magnetization \vec{M} and the magnetic flux density \vec{B} depend on each other according to $\vec{B} = \mu_0 \mu_r \vec{H}$, where μ_0 is the permeability of free space and μ_r is the permeability of the medium. The current density \vec{J} , and the electric field are related by $\vec{J} = \vec{J}_{source} + \sigma \vec{E}$, where σ is the conductivity of a medium. It is important to note that only the curl equations ($\nabla \times$) determine how the \mathbf{E} and \mathbf{H} fields

vary in space and time. The two divergence ($\nabla \cdot$) equations are implicitly described by the curl equations provided the initial conditions: $\nabla \cdot \vec{D}|_{t=0} = \nabla \cdot \vec{B}|_{t=0} = 0$ hold.

These equations are discretized in space and time resulting in a set of explicit finite-difference equations. Figure 2.15 shows one cube in the FDTD calculation domain. The discretized mesh has (i, j, k) spatial indices along the $x, y,$ and z -axes as shown in the figure with spatial resolution $\Delta x, \Delta y$ and Δz respectively. The implemented code has a uniform grid spacing $\Delta x = \Delta y = \Delta z = \delta$. Note that each of the electric field (\vec{E}) components are surrounded by four magnetic field (\vec{H}) components. Similarly, each of the magnetic field (\vec{H}) components are surrounded by four electric field (\vec{E}) components. The difference equations compute the new field components from the field components at the previous time step with resolution Δt . The six scalar finite difference equations to calculate the vector \vec{E} and \vec{H} fields are

$$\begin{aligned} E_x^{n+1}(i+1/2, j, k) &= A_{i+1/2, j, k} E_x^n(i+1/2, j, k) + B_{i+1/2, j, k} [H_z^{n+1/2} \\ &\quad (i+1/2, j+1/2, k) - H_z^{n+1/2}(i+1/2, j-1/2, k) + \\ &\quad H_y^{n+1/2}(i+1/2, j, k-1/2) - H_y^{n+1/2}(i+1/2, j, k+1/2)] \end{aligned} \quad (2.3a)$$

$$\begin{aligned} E_y^{n+1}(i, j+1/2, k) &= A_{i, j+1/2, k} E_y^n(i, j+1/2, k) + B_{i, j+1/2, k} [H_x^{n+1/2} \\ &\quad (i, j+1/2, k+1/2) - H_x^{n+1/2}(i, j+1/2, k-1/2) + \\ &\quad H_z^{n+1/2}(i-1/2, j+1/2, k) - H_z^{n+1/2}(i+1/2, j+1/2, k)] \end{aligned} \quad (2.3b)$$

$$\begin{aligned} E_z^{n+1}(i, j, k+1/2) &= A_{i, j, k+1/2} E_z^n(i, j, k+1/2) + B_{i, j, k+1/2} [H_y^{n+1/2} \\ &\quad (i+1/2, j, k+1/2) - H_y^{n+1/2}(i-1/2, j, k+1/2) + \\ &\quad H_x^{n+1/2}(i, j-1/2, k+1/2) - H_x^{n+1/2}(i, j+1/2, k+1/2)] \end{aligned} \quad (2.3c)$$

$$\begin{aligned}
H_x^{n+1/2}(i+1/2, j+1/2, k) &= H_x^{n-1/2}(i, j+1/2, k+1/2) + \frac{\Delta t}{\mu\delta} [E_y^n(i, j+1/2, k+1) \\
&\quad - E_y^n(i, j+1/2, k) + E_z^n(i, j, k+1/2) - E_z^n(i, j+1, k+1/2)]
\end{aligned} \tag{2.3d}$$

$$\begin{aligned}
H_y^{n+1/2}(i+1/2, j, k+1/2) &= H_y^{n-1/2}(i+1/2, j, k+1/2) + \frac{\Delta t}{\mu\delta} [E_z^n(i+1, j, k+1/2) \\
&\quad - E_z^n(i, j, k+1/2) + E_x^n(i+1/2, j, k) - E_x^n(i+1/2, j, k+1)]
\end{aligned} \tag{2.3e}$$

$$\begin{aligned}
H_z^{n+1/2}(i+1/2, j+1/2, k) &= H_z^{n-1/2}(i+1/2, j+1/2, k) + \frac{\Delta t}{\mu\delta} [E_x^n(i+1/2, j+1/2, k) \\
&\quad - E_x^n(i, j+1/2, k) + E_y^n(i, j+1/2, k) - E_y^n(i+1, j+1/2, k)]
\end{aligned} \tag{2.3f}$$

where the terms A and B are given as

$$A_{i,j,k} = 1 - \frac{\sigma(i, j, k)}{\epsilon(i, j, k)} \tag{2.4}$$

$$B_{i,j,k} = 1 - \frac{\Delta t}{\epsilon(i, j, k)\delta} \tag{2.5}$$

2.3.2 Accuracy and Stability

Past work has shown that for FDTD methods to yield accurate results for a given wavelength, the grid spacing, δ , must be less than the smallest dimension of the simulation geometry and typically 1/10th of the smallest wavelength [Taflove, 1995]. Hence, the highest frequency or the smallest wavelength controls the size of the FDTD domain. The stability

condition relating the δ and temporal step size Δt is

$$\Delta t \leq \frac{\delta}{c\sqrt{3}} \quad (2.6)$$

where c is the speed of light. This condition places a bound on the minimum sampling time based on the time taken by an electromagnetic wave to propagate at the speed of light from one grid point to the next. Sub-Courant conditions can be achieved if the FDTD problem space is enclosed inside a medium of refractive index, n , such that the electromagnetic wave propagates slower at $v = c/n$ and hence the time resolution scales as $n\Delta t$.

2.3.3 Boundary Conditions

In a finite sized FDTD grid, there are spurious reflections at the domain boundaries because of abrupt terminations. These reflections are avoided by using perfectly matched layer (PML) boundary condition [Berenger, 1994]. The PML boundary has a diagonal matrix of permittivity and conductivity which permits perfect transmission and zero reflection of an incident electromagnetic wave at all frequencies and angles of incidence. The PML boundary condition was chosen instead of a more commonly used absorbing boundary condition (ABC) because PML provides a larger dynamic range (80 dB) for the simulations compared to ABC (25 dB) [Taflov, 1995]. For all the simulations performed, PML with 7 matched layers are chosen.

2.3.4 Serial Implementation

Figure 2.16 shows the flow diagram for the serial FDTD simulator. At $t = 0$, the domain size, problem geometry and the material properties of the various objects in the problem space are read from the header file. The uniform FDTD grid is generated. The \vec{E} and \vec{H} field arrays in the simulation space are initialized to zero. The initial source voltage is applied to the antenna terminals. The currents on the antenna are calculated from the magnetic field using Ampere's law. Using Equations 2.3 (a-f) \vec{E} and \vec{H} components are calculated at alternate half time steps, such that at the n^{th} time step, the \mathbf{H} field components are

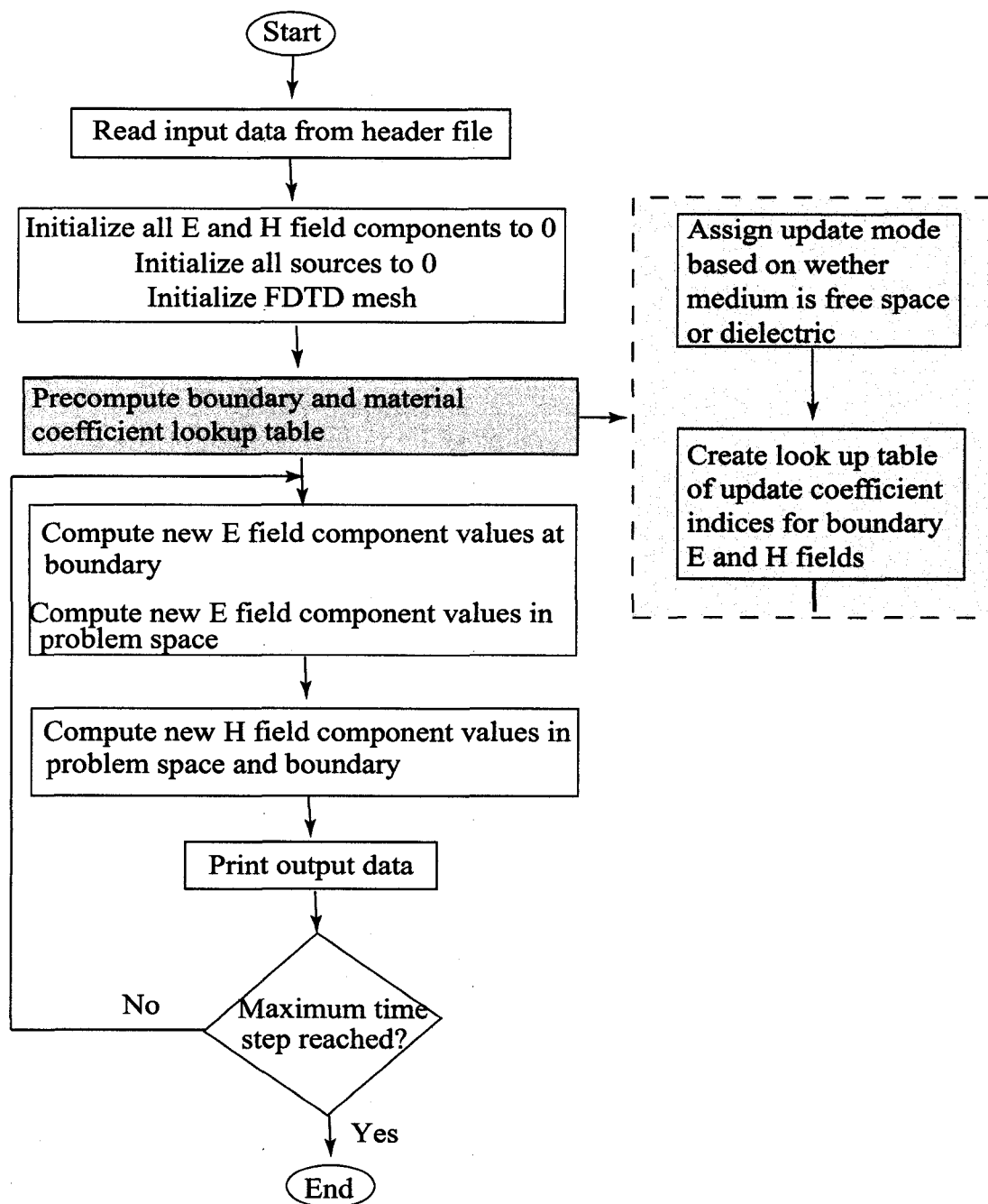


Figure 2.16. **Computation flow of the serial FDTD program.** The grayed out area are changes made to a normal FDTD computation flow in order to improve performance and make the code more suitable for parallel programming.

calculated at the $n+1/2$ time step followed by the \vec{E} field components at the $n+1$ time step. This update cycle is repeated until the last time step is reached. At each time step the electric and magnetic fields at the boundaries are calculated and the boundary conditions imposed.

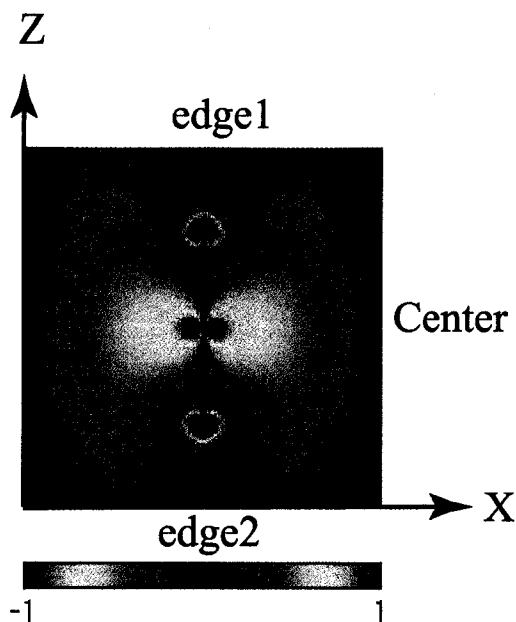


Figure 2.17. Snapshot in time of the electric field strength radiated by a 6 cm long dipole antenna.

To test the validity of the FDTD code, two test cases were calculated. The first case was the calculation of the radiation fields from a 6 cm dipole antenna. Figure 2.17 shows a snapshot of the normalized electric field magnitude radiated by the dipole antenna across a $100 \times 100 \times 357$ grid of points at the 1021 time step. The dipole antenna is excited by a modulated gaussian waveform with pulse width 1 ns and center frequency 2 GHz. At 2 GHz the dipole is half a wavelength long. The dipole radiates most of its energy from the center and the ends of each of its arms. This agrees with Figure 4.15 in Schantz [2005].

The second test performed was to check if the PML absorbing boundary conditions functioned properly. Figure 2.18 shows three snapshots in time of an electromagnetic wave

impinging on the PML boundary. The first snapshot in Figure 2.18A shows the electromagnetic wave propagating towards the PML layer. Figure 2.18B shows that the incident wave propagates into the absorbing layer with very little energy reflected back into the problem space. Figure 2.18C shows that the transmitted energy is completely absorbed and a small portion of the reflected energy propagates back in the problem space. A single PML layer is included in this simulation. A total of 8 layers were chosen for the rest of the simulation done in this chapter.

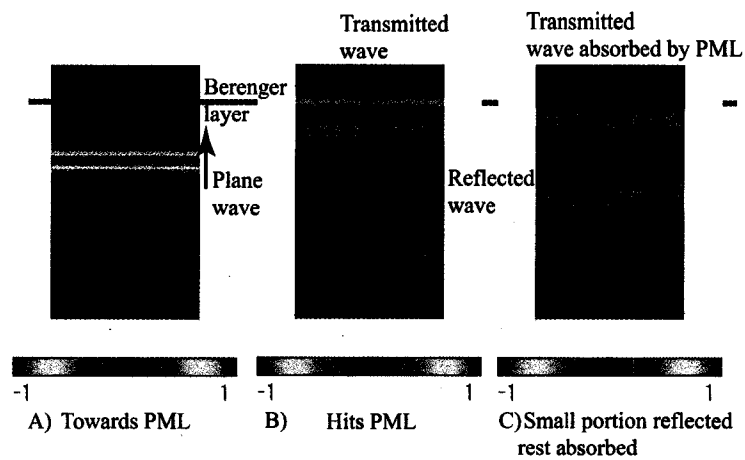


Figure 2.18. Three snapshots in time of a electromagnetic wave impinging on the PML boundary.

2.3.5 Bottlenecks in Serial Code

For UWB simulations, the smallest wavelength is ~ 2 cm (15 GHz). Hence the maximum spatial grid resolution is 2 mm. For free space propagation of an electromagnetic wave the time resolution is chosen as 3.8 ps. A 60 cm X 60 cm X 60 cm domain would require 27×10^6 grid points. In a 3-D simulation, each grid point stores arrays for 6 field components, permittivity, ϵ , conductivity, σ , and the 27 real and imaginary field components for the PML boundary layers as double precision floating point numbers. Each double precision floating point number occupies 8 bytes. So for the whole problem space $27 \times 10^6 \times 1.05 \times (18 \times 8 + 8) = 1.3$ GB of memory is required. There is additional storage associated with the 6 PML

boundary layers which is 796 MB. The memory scale factor of 1.05 is for pointer operations. Therefore a total of 2.1 GB of memory is required.

The dipole simulation presented in the previous section took ~ 43 mins for a 60 cm X 60 cm X 100 cm domain and a total of 1200 time steps at 0.5 ps time resolution. The simulation was done on an AMD Athlon 32 bit 2.2 GHz processor with 512 MB of RAM. Profiling the serial code reveals that 97% of the execution time is spent in updating the electric and magnetic field arrays. The large memory allocation for the electric and magnetic fields and the associated update coefficients require careful handling to prevent cache misses that severely affect performance and scalability.

Modifications to the serial code permit reduction of data storage. The ϵ and σ at each grid point are stored as real values, and only 6 values per grid point are stored. Also the material properties are pre-loaded in a look-up table and only a 1 byte short integer ID tag for the material is supplied to each node during computation. This further reduces the storage requirement for the FDTD code. Hence the number of bytes is reduced from 96 bytes per grid point to 1 byte per grid point. Still the serial implementation of the FDTD approach using Yee's algorithm is computationally intensive and a parallel implementation is necessary for larger computational domains.

2.3.6 Parallel Implementation of the Serial Code

The serial implementation of the FDTD code has a characteristic feature that makes it amenable for parallel programming; When the electric fields are being updated, the magnetic fields are only read and when the magnetic fields are being updated, the electric fields are only read at each grid point. Hence as long as the field update loops are kept separate, these calculations can be completed in a multi-threaded OpenMP environment. There is no risk of a race condition as long as different threads update different field components. Additionally, there is no domain distribution overhead problem as long as the storage is accessible by all of the threads.

The C code was parallelized using OpenMP multiple threading environment. The up-

date equations for the \vec{E} and \vec{H} fields are split up by the multiple processors in the multi-threading environment. The speedup of the code after multi-threading for the dipole simulation with a 200 X 200 X 200 domain space with 1000 time steps running on an IBM p650 computer with eight 1452 MHz Power4 processors and 1 GB of RAM is shown in Figure 2.19. The problem scales well up to 6 processor threads after which the inter-thread communication overhead swamps the improvement and hence shows a higher execution time for 8 threads.

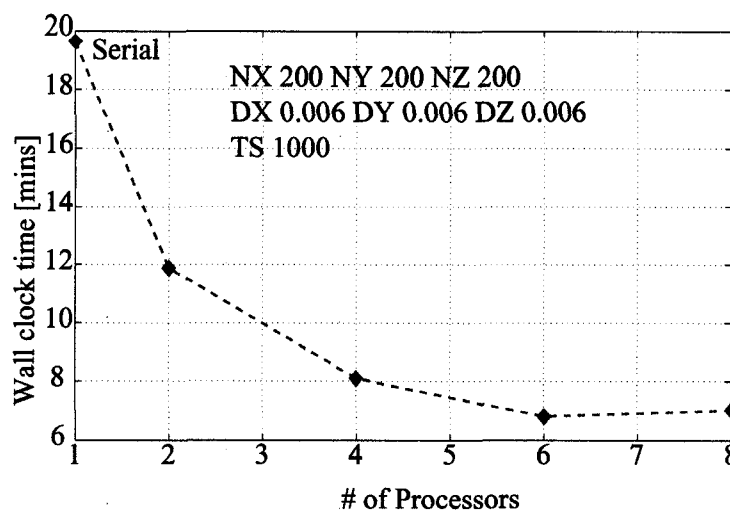


Figure 2.19. The execution time as a function of the number of processors for a 200 X 200 X 200 problem space with 1000 time steps.

2.4 Simulation of the Oval Dipole Antenna

The parallel FDTD code is used to calculate the transient response of an oval dipole antenna. The top and bottom panel of Figure 2.20 shows the coordinate system and simulation geometry of the oval dipole in two projection planes. The UWB frequency range from 3.1 GHz to 10.6 GHz corresponds to a minimum wavelength of ~ 3 cm. Hence the spatial resolution of the FDTD mesh is 3 mm and the corresponding time step is 5 ps calculated using the Courant condition (Equation 2.6). The simulated spatial domain is 2 m long in

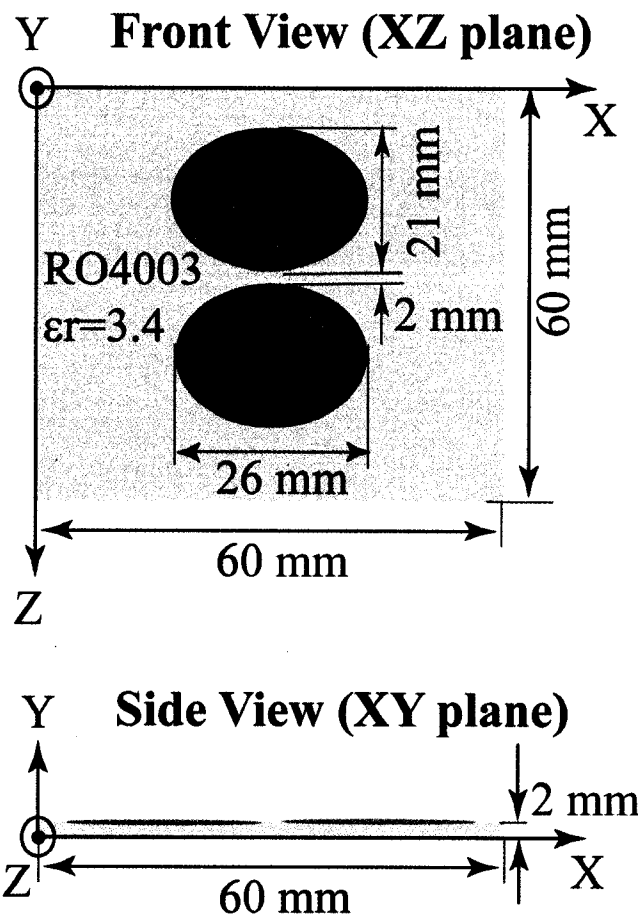


Figure 2.20. Simulation geometry of the oval dipole antenna. The Front view and the side view of the simulated oval antenna geometry. The antenna coordinate frame for the simulations is also shown. The plane containing the antenna is defined as the horizontal x - z plane and the normal to the plane is the y -axis. The elevation angle θ is defined from the plane containing the antenna with 0° (endfire) along the z -axis and 90° (broadside) along the y -axis. The azimuth angle is defined from the x -axis with 0° along the x -axis and 90° (broadside) along the y -axis. Note that this convention is opposite to the convention used for the measurements presented in the previous section.

each dimension corresponding to a 700 X 700 X 700 uniform rectangular mesh of points. The input voltage waveform for the simulation is the measured Multi Spectral Solutions, Inc. (MSSI) TFP1001 impulse source (Figure 2.2C). The balun structure is not included in the simulation model and the input voltage waveform is applied to the center of the antenna structure which has a gap of 2 mm between the ovals.

Figure 2.21 showing the received voltage waveform as a function of four elevation angles 0° , 20° , 60° and 90° , is calculated using the FDTD code. The calculated radiated electric field waveform for each of the elevation angles is convolved with the measured broadside receiving horn antenna transfer function to calculate the received voltage waveform. These simulated received voltage waveforms (black curve) show excellent agreement with the oscilloscope measurements for the 90° , 60° , 40° , and 20° elevation angles. The comparison of the pulse shape, duration and cycle time of the simulated and measured waveforms for these four elevation angles show $< 5\%$ variation. The simulation result for the 0° elevation angle shows poor agreement with measurement. This is because the simulation does not include the balun structure which radiates most of the energy received by the horn antenna when the antenna is aligned with its axis facing the receiving horn antenna.

The top left panel of Figure 2.22 shows a schematic of the right hand rule of radiation. A dipole is a pair of opposite charges separated by a distance d . Energy supplied to the dipole causes the charges to move back and forth about their mean position. The moving charge corresponds to a current. The right hand rule of radiation [Schantz, 1997] states that, "if the thumb of the right hand points in the direction of the rate of change of current then the fingers curl in the direction of the radiated magnetic field."

The radiated electric field vector \vec{E} , the radiated magnetic field vector \vec{H} and the direction of propagation of the electromagnetic wave \vec{k} form a mutually orthogonal system. Hence the radiated electric field is in the same direction as the rate of change of current but has opposite sign. This will be used to relate the surface currents calculated on an oval dipole antenna to the nature of the radiated electric field waveform.

The bottom left panel of Figure 2.22 shows the radiated electric field waveform calculated

by the FDTD code for three elevation angles 0° , 30° , and 90° (solid black curve). Also shown in the figure is the DSO measurement of the electric field waveform (solid gray curve). The measured electric field waveform is calculated by de-convolving the broadside receiving horn antenna transfer function, measured using a VNA, from the received voltage waveform. The calculated waveform shows good agreement with the primary cycle of the measured waveform. There are additional features, such as secondary cycles and elongated width, in the measured electric field pulse which are not reproduced by the simulation. These could be due to the limited bandwidth of the frequency domain measurement (0.0003 to 9 GHz) of the horn antenna's response or the parasitic radiation from the balun structure which couples with the intense fields close to the antenna and distorts the radiated waveform [Schantz, 2005].

The right panel of Figure 2.22 shows a time evolution of the derivative of the vertical component of the surface current on a 26 cm X 21 cm oval dipole antenna at 5 different time steps corresponding to the points marked A, B, C, D and E in the broadside ($\theta = 90^\circ$) electric field waveform. Due to the symmetry of the oval dipole, the horizontal components of antenna current always exist as opposing pairs, so there is no net radiated energy in the far field. Only the vertical components need to be considered from the standpoint of radiated energy. At point A, the impulse enters the antenna at the feed point. Current is increasing in an upward direction in both the upper and lower arms of the antenna. Because the electric and magnetic fields are orthogonal to each other, upward accelerating currents result in a downward directed electric field (Figure 2.22, point A) in the radiated waveform. At point B, the current continues to propagate away from the feed point. At the same time, the feed from the source has ended and instantaneous currents at the feed point are decreasing. The instantaneous rate of change of currents are in opposing directions at the feed point and the mid point of the antenna. These opposing currents partially cancel in the far field resulting in reduced field strength at point B. The area of decelerating currents near the feed point continues to increase as the original impulse propagates toward the tip of the antenna. At point C, these factors approximately cancel each other and the

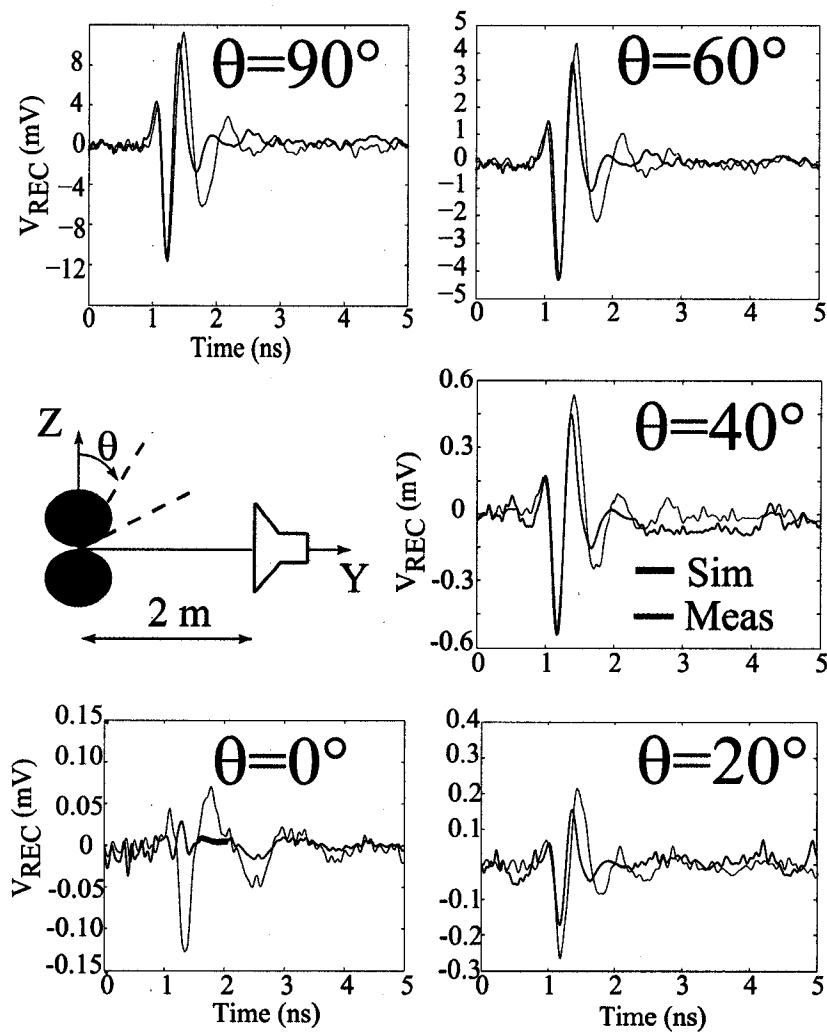


Figure 2.21. Measured and simulated received voltage waveform for an oval dipole transmitting antenna and a horn receiving antenna system. The red curves show the time domain measurement using a DSO and an MSSSI source. The black curves show the simulated received voltage waveform when the input waveform to the FDTD simulation is the MSSSI waveform. The simulation calculates the radiated electric field from the oval dipole antenna 2 m away from the transmitting antenna. The calculated electric field is Fourier transformed and its frequency spectrum is multiplied with the receiving transfer function of the horn antenna. The resulting spectrum is inverse Fourier transformed back to the time domain. The additional delays associated with the phase of the horn antenna and the method are removed to line up the maximum peak of the two waveforms.

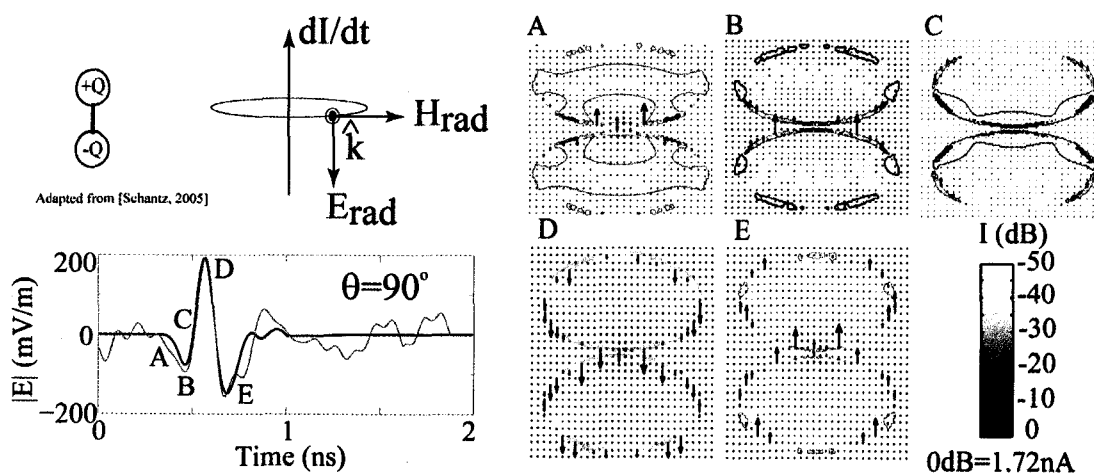


Figure 2.22. Time evolution of the current distribution on the oval antenna calculated using FDTD. The top left panel shows the right hand rule of radiation adapted from Schantz [2005]. The bottom left panel shows the calculated (black) and measured (gray) electric field waveform in the broad side direction $\theta = 90^\circ$. The calculated waveform shows good agreement with the primary cycle of the measured electric field waveform and shows similar cycle duration within 10%. The duration of the primary cycle of the waveform deviate by 5%. The right panel shows the time evolution of the vertical component of the current derivative at 5 points marked A, B, C, D, and E on the electric field waveform. Also plotted at each time is the magnitude (size of arrow) and direction (arrow direction) of the vertical current derivatives (arrows) on the antenna surface.

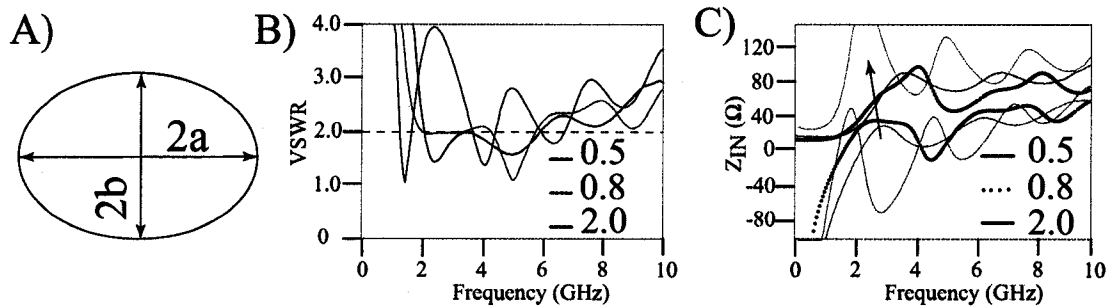


Figure 2.23. Effect of axial ratio of the oval on its matching and gain properties. (A) Schematic of the oval dipole with major axis a and minor axis b . (B) VSWR simulated using FDTD for three axial ratios 0.5, 0.8 and 2. (C) The input impedance of the oval dipole for the three axial ratios.

radiated electric field approaches zero. As time passes, the accumulated charge in the two arms of the antenna reaches a maximum, and the downward current derivative reaches a maximum (point D). Current is accelerating in a downward direction over the entire structure, producing a peak positive directed electric field in the radiated waveform. As the built up charge in the antenna dissipates, the change in current slows. Eventually, the local electric field approaches a minimum with most of the local energy stored in the magnetic fields around the antenna. Currents are nearly constant and radiated energy approaches zero. As the magnetic field collapses, the cycle repeats itself (at reduced levels) and the direction of the rate of change of current once again points upward, this time producing a negative electric field in the radiated waveform (point E). This simulation suggests that there is a handshake of energy between the static and quasi-static reactive fields close to the antenna and the radiation fields. Therefore, the radiation efficiency of an antenna in a wide frequency range is improved by reducing the energy lost to the reactive fields surrounding the antenna.

Figure 2.23A shows a schematic of an oval dipole with the major axis, a , and the minor axis, b , defined. Here the axial ratio is defined as the ratio of the minor axis to the major axis of the ellipse. Figure 2.23B and 2.23C show the VSWR and the input impedance of

the oval dipole for three axial ratios. In Figure 2.23C, the radiation resistance is shown as the red curve and the reactance is shown as the green curve. These results suggest that “bulbous” oval antennas (axial ratio < 1) have increased bandwidth but reduced gain compared to narrower “skinny” oval antennas (axial ratio > 1). This agrees with past measurements [Schantz, 2005] and can be explained as follows. The currents on the oval propagate differently at different frequencies (modes). Past work on a diamond dipole antenna [Lu *et al*, 2004] has shown that lower frequency currents are focused near the feed point of the antenna and higher frequency currents propagate along the edge of the antenna to the tip of the dipole. A similar behavior is observed in the distribution of the fundamental mode current of the oval dipole antenna shown in Figure 2.22. As the frequency increases the current peak moves along the edge of the oval to the tip of the oval away from the feed point. Hence the impedance difference between the various surface current modes determine the impedance bandwidth of the antenna. A smoother shape transition from the feed point to the tip of the antenna would result in smaller impedance differences between the current modes, which in turn would translate to a larger operational bandwidth. A sharper shape transition (like the edge of a triangle in a bow tie antenna) would result in larger impedance differences between the current modes reducing the operational bandwidth of the antenna. For an oval dipole antenna a smoother shape transition of the radiating element would imply increased axial ratio of the oval and hence a shorter length of the antenna. A shorter length relates to a lower gain and a higher cut off frequency of the radiation bandwidth of the antenna. For the same area of the radiating element, a sharper shape transition would imply reduced axial ratio of the oval and hence a longer antenna. A longer antenna implies increased gain at the cost of increased return loss, narrower operational bandwidth and a lower cut off frequency of the radiation bandwidth of the antenna. All of these features are observed in the results shown in Figures 2.23B and 2.23C. The results in the figures are specific to the input excitation which is a Gaussian waveform with a time duration of 1 ns.

An alternative explanation can also be provided for the results shown in Figures 2.23B and 2.23C. The reactance of the antenna, shown as a black curve in Figure 2.23C, increases

with increasing axial ratio, suggesting that energy stored in the electric and magnetic fields surrounding the antenna increases. This would imply that the quality factor of the antenna, which is the ratio of the stored energy to the radiated energy, increases. An increasing quality factor implies a narrower bandwidth and hence a more dispersive antenna.

2.5 Summary of Results

The following measurement results were presented in this chapter: (1) Time and frequency domain measurements of the transient response of an oval and cat-fish dipole antenna in the DC to 9 GHz frequency range. (2) Measured transmitting and receiving impulse response and transfer function of the two UWB antennas and a commercial horn antenna showed that the transmitting antenna will double differentiate an input UWB waveform as long as the spectrum of the input signal is within the operational bandwidth of the antenna. (3) The oval dipole has a half power beam width of 67° with a maximum at 85° in the vertical plane. (4) The peak amplitude of the cross polarized pulse radiated by an oval dipole in the broadside direction is 15 dB down compared to the co-polarized pulse peak amplitude.

The following simulation results were presented in this chapter: (1) FDTD numerical code was developed and tested in ARSC at UAF. (2) FDTD simulations of the currents on the surface of an oval dipole were related to the nature of the radiated electric field waveform. (3) The geometry of the oval antenna was related to the antenna radiation properties.

2.6 Discussion

The experimental and numerical results presented in this chapter suggest a strong relationship between the geometry and orientation of an UWB antenna to the radiated pulse properties (e.g., pulse width, cycle time, bandwidth, center frequency). The implication of the following antenna properties for UWB applications in light of the work presented in this chapter is discussed:

(1) Reciprocity: The transmitting and receiving transfer function and impulse response measurements verify previous conclusions [Schmitt, 1960; Kanda, 1980] that, “a UWB antenna’s transmitting transient response is proportional to the derivative of the receiving transient response.” A derivative of the input waveform in the time domain translates to multiplying the transfer function in the frequency domain by $j\omega$. Hence two time derivatives imply multiplication by $-\omega^2$. The 180° (multiply by -1) rotation between the transmitting and the receiving antenna impulse response and the shape of the impulse response in Figure 2.7 suggests that the transmitting antenna will differentiate an input UWB waveform as long as the spectrum of the input signal is within the operational bandwidth of the antenna. The receiving oval dipole antenna will not introduce zero crossings in the received waveform as long as the radiated spectrum is within the antenna operational bandwidth. This has also been mathematically derived by Shlivinski and Heyman [1999] and experimentally demonstrated by Scheers *et al.* [2000].

(2) Impedance matching: The antenna geometry controls the distribution of currents on the antenna from the feed point, which in turn control the impedance matching of the antenna to a 50Ω load. To understand how this affects performance of a communication system, consider the following example: A 10 Mbps communication system with no coding and pulse position modulation transmits 1 pulse every 100 ns. Assuming the duration of the UWB signal is 1 ns and the feed line to the antenna is 50 cm long and has an effective permittivity of 4, the phase speed of propagation of the signal on the feed line is 1.5×10^8 m/sec. If the antenna reflects 25% of the incident signal (VSWR of 3:1) and the transmission line has negligible losses then the amplitude of the reflection is 1/8th of the amplitude of the incident signal delayed by ≈ 6.7 ns. So if the input signal is 1 V, the re-radiated signal amplitude is 125 mV. The delayed copies will be re-radiated. The propagation channel will also introduce delayed replicas of the original radiated signal and the re-radiated signal which will overlap constructively or destructively at the receiver, thereby influencing the signal-to-noise ratio and the bit error rate of the communication system [Sonwalkar *et al.*, 2006]. Hence, ovals with an axial ratio of 0.5 have a gradual impedance transformation

from the feed point, to free space (377Ω) thereby reducing the signal energy reflected back into the transmission line.

(3) Radiated pulse properties as a function of radiation angle: The oval dipole has uniform pulse properties within 5% in the vertical plane for a broad beamwidth of $\sim 60^\circ$ on either side of the broadside direction. This permits applications like channel sounding and radio frequency identification tags. Increasing the axial ratio of the oval antenna will reduce the beam width of the antenna and hence control the properties of the pulse radiated in a particular direction. For example, suppose that Bob and Alice are communicating with one another, then Eve (eavesdropper) can intercept and decode the information as the broad beamwidth of the antenna provides Eve with consistent pulse properties. Now Bob and Alice can synchronously change the properties of the input waveform such that the pulse radiated by the antenna is consistent over a much narrower beamwidth thereby preventing Eve from decoding the information. This presents a new physical layer of security above the standard coding techniques.

2.7 Concluding Remarks

The results in this chapter showed that the nature (e.g., amplitude, shape, time duration) of the radiated UWB waveform is closely related to the geometry of the UWB antenna. The next chapter will discuss how multipath propagation of an UWB pulse relates to the received waveform properties (pulse width, cycle time, bandwidth and center frequency).

Chapter 3 UWB Pulse Propagation: Experiments and Numerical Simulations

3.1 Objective and Significance

The objective of this chapter is to relate the nature of the received UWB pulse to the physical properties of the propagation channel. Measurements and numerical simulations of UWB pulse propagation in two scenarios are presented: (1) empty parking lot and (2) cluttered hallway and room inside a building. A theoretical model is developed to relate the nature of the radiated UWB pulse and the physical properties of the propagation channel/reflecting surface that causes the multipath. Ray tracing and finite difference time domain (FDTD) calculations are presented for propagation scenarios with single and multiple reflecting surfaces respectively. Implications of this work towards communication, navigation, and radar applications are discussed.

Overlap due to multipath propagation places a fundamental limit on the use of UWB technology [Taylor, 2000]. This limitation depends on the properties of the pulse as well as those of the propagation channel. Recent advances in UWB transmitter and receiver technologies permit adaptive variation in the characteristics of the UWB waveform transmitted

[Silva *et al.* 2007; Mclean *et al.*, 2006]. This makes it possible/practical to use a pulse that is optimized for a given application or propagation scenario. Therefore it is important to study how multipath propagation of UWB pulses depends on the waveform properties and the environment/channel/reflector that causes the multipath.

A fundamental propagation problem is the reflection of a UWB pulse from a single reflecting surface [Allen *et al.*, 2006]. Past work identifies three propagation regimes due to the interference (overlap) of the direct path pulse and the pulse reflected from the surface [Ghavami *et al.*, 2007; Siwiak and McKeown, 2004]. This overlap causes the received signal strength to fall off as the fourth power of the transmitter-receiver separation distance when the differential delay is less than half the pulse width, τ_p [Siwiak and Petroff, 2001]. The signal strength fall off have exponents that transit from ~ 2 (free space) to ~ 4 and this transition distance is referred to as the narrow bandwidth break point distance, R_b [Bertoni, 2000]. The breakpoint distance increases with bandwidth, B , which is estimated either as the arithmetic mean [Sato and Kobayashi, 2004] or the geometric mean [Siwiak *et al.*, 2003] of the upper (f_h) and lower (f_l) cut off frequencies. Recently, Liu *et al.* [2006] observed a new unsteady breakpoint in the UWB signal strength measurements at short separation distances (≤ 5 m) between the transmitter and receiver. A fluctuation of up to 6 dB is observed in the measured signal strength beyond this break point up to a transmitter-receiver separation distance of 10 m [Dohler *et al.*, 2004]. Aroonpraparat *et al.* [2006] have proposed a linear regression dual slope path loss model for UWB ground reflection. Promwong *et al.* [2007] have proposed an experimental scheme to evaluate the effect of antenna response on the UWB ground reflection transmission loss. Recent simulation work by Yang *et al.* [2007] has shown the existence of three propagation regions in which the path loss has differing slopes depending on electric field polarization. Recent frequency domain propagation measurements by Malik *et al.* [2007] have shown that the slope of the fall off in the signal strength as a function of transmitter-receiver separation distance increases with increasing center frequency.

All the aforementioned results assume that far-field approximations hold. Numerical

calculations [Cotton *et al.*, 1999] have shown that for a 5.8 GHz system (100 MHz bandwidth) the near-field effects are substantially reduced to $\sim 1\%$ when the separation distance between the transmitter and receiver and the antenna heights above the reflecting surface are ≥ 1 m for a pair of short dipole antennas. It has also been shown that for UWB pulse propagation, the errors associated with the far field approximation are $\sim 12\%$ for short ranges (≤ 5 m) and incidence angles close to the Brewster angle [Raspopovic and Thompson, 2005]. This error increases with permittivity, ϵ , and center frequency, f_c . The % refers to the change in field strength in relation to the expected far field amplitude.

A detailed review of the past work showed that a systematic investigation of the dependence of the propagation regimes on the nature of the transmitted UWB pulse is lacking. Hence this chapter focuses on measuring the properties of UWB pulse propagation in the presence of single and multiple reflecting surfaces. The observed features are explained using a two ray model and a FDTD simulation model respectively. A theoretical framework is developed to interpret and analyze UWB pulse propagation in far more complicated scenarios (e.g., hallway, room) than the scenario discussed in this chapter.

Section 3.2 discusses the propagation measurements, simulations and the theoretical framework developed for UWB signal propagation in the presence of a single reflecting surface in an empty parking lot. Section 3.3 discusses the propagation measurements, and the FDTD calculations for UWB signal propagation inside a hallway and a room and compares measurements with simulations. Section 3.4 summarizes the results presented in this chapter. Section 3.5 discusses the implications of this work for UWB communication, navigation and radar applications and the sixth section presents concluding remarks.

3.2 UWB Pulse Propagation in an Empty Parking lot

This section presents the measurements, numerical simulations and the theoretical models developed for UWB pulse propagation in the presence of a single reflecting surface.

3.2.1 Measurements

Measurements were performed to study the effects of multiple path propagation arising from the overlap of the direct and ground reflected pulses on the received pulse peak amplitude as the relative locations of the receiver and transmitter were varied. The dates, temperature and the ground conditions when the experiments were performed in the Taku parking lot at UAF are listed in Appendix B.4. The effect of the snow as well as the condition of the ground were detectable in the measurements and are discussed in section 3.2.1.5 and Appendix B.4.

3.2.1.1 Experiment Geometry

Figure 3.1 shows the schematic of experimental arrangement. The transmitting antenna (Tx) and the receiving antenna (Rx) are located at heights h_1 and h_2 , respectively, above the reflecting surface (ground) and are separated by a distance d . The transmitted signal reaches the receiver via a direct path and a reflected path as shown in the figure. The figure labels various angles and possible electrical field polarization vectors for this geometry.

3.2.1.2 Instrumentation Description and Measurements

The measurements, following the geometry shown in Figure 3.1, were carried out with the Time Domain Corporation® (TDC) PulsON 200TM UWB evaluation kit, one of the first commercially available devices to be certified under the FCC part 15 ruling for UWB transmissions [FCC, 2002]. Each PulsON 200TM evaluation kit contains two identical UWB transceivers with bottom-fed 2.6 cm x 4.3 cm planar elliptical dipoles [Schantz, 2003]. The transmitted UWB pulse is ~ 1 ns with frequency content from 2.5 to 6 GHz. When the transceivers are oriented vertically, their radiation pattern is similar to that of a dipole with a maximum 3 dB variation in the horizontal plane. The short duration UWB pulses are transmitted at a pulse repetition frequency of 9.6 MHz, resulting in a nominal average transmit power of approximately 50 μW . The PulsON 200TM receiver captures the received waveform by internally integrating a minimum of 16 received pulses (corresponding to a

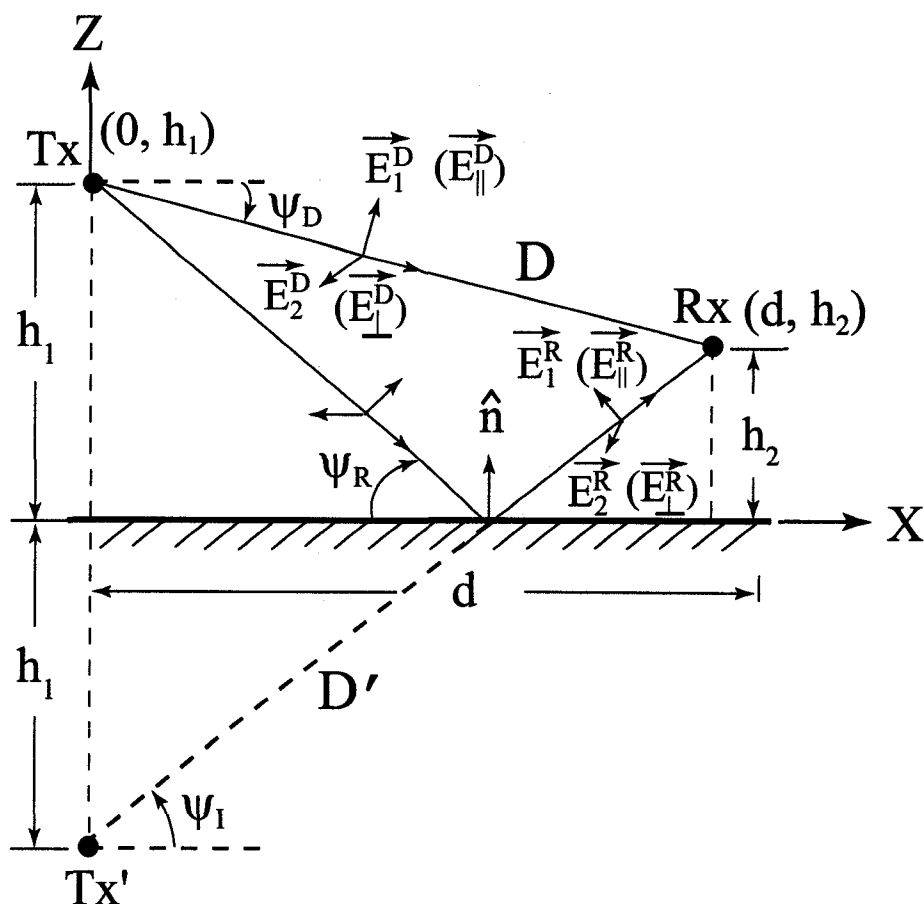


Figure 3.1. Schematic showing the geometry of UWB pulse propagation in the presence of a single reflecting surface. A UWB pulse from a transmitter (Tx) can reach the receiver (Rx) via a direct path of length D and a reflected path of length D' . The transmitter and receiver are located at heights h_1 and h_2 , respectively, from the reflecting surface and are separated by a distance d . The reflected ray path makes an angle ψ with the surface. Tx' represents the image of the transmitter. The figure also shows the parallel and perpendicular components of the electric field of the direct and reflected pulses.

maximum data rate of 600 kbps). The peak amplitude of the received waveform provides a measure of the received signal strength.

The PulsON 200TM radios were evaluated in the UAF anechoic chamber to determine the output power and received waveform using PulsON's performance application tool (PAT) and a Tektronix TDS6804B Digital Sampling Oscilloscope. The DSO has a sampling rate of 20 Gs/s corresponding to a minimum time resolution of 50 picoseconds and a dynamic range of 45 dB. First, both transmitting and receiving antennas were oriented vertically and facing each other, as shown in the inset of Figure 3.2A. This permits measurement of the parallel electric field component (labeled \mathbf{E}_1 or \mathbf{E}_{\parallel} in Figure 3.1). Figure 3.2A shows the average waveform of the 16 pulses received by the PulsON receiver at 1 m separation distance, a far field distance at UWB frequencies. The received signal was captured using the PAT tool (dotted line) and the DSO (solid line). From the figure we note that the pulse width τ_p is ~ 1.5 ns, and the cycle time τ_c is ~ 0.25 ns. The calculation of the τ_p and τ_c is discussed in Appendix B.1. The peak amplitude of the pulse is 112 mV. Figure 3.2B shows the spectrum of the waveform shown in Figure 3.2A. From this spectrum, we obtain a -10 dB bandwidth of 2 GHz. The calculation of the -10 dB bandwidth B and center frequency f_c is discussed in Appendix B.2. Next, the receiving antenna was rotated by 90° in the vertical plane, as shown in the inset of Figure 3.2C. This permits measurement of the perpendicular electric field component (labeled \mathbf{E}_2 or \mathbf{E}_{\perp} in Figure 3.1). Figure 3.2C, shows the average waveform of the 16 pulses received by the PulsON receiver at 1 m separation distance for perpendicular polarization. The peak amplitude of the pulse is 13.2 mV, about an order of magnitude smaller than that for the vertical polarization. From the figure, τ_p is ~ 1.5 ns, and τ_c is ~ 0.2 ns. The Figure 3.2D shows the spectrum of the waveform shown in Figure 3.2C. From this spectrum, we obtain a -10 dB bandwidth of about 2 GHz. To summarize, we note that the time and frequency domain properties of both polarizations are similar and the main difference is in their amplitudes.

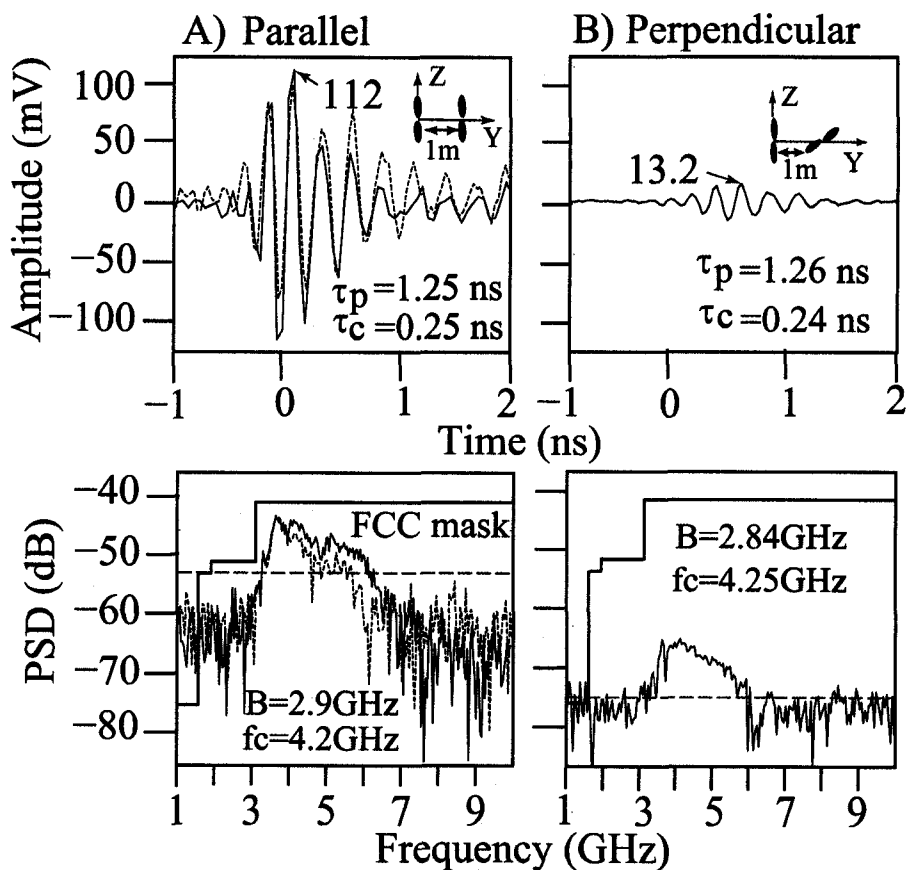


Figure 3.2. The PulsON 200TM impulse captured by the PulsON 200TM receiver (dotted line trace) and the Tektronix DSO (solid line trace), and their frequency domain spectra (lower panel). (A) The pulse is captured when the transmitting and the receiving antennas are aligned parallel to one another hence the parallel electric field component is measured. (B) The pulse is captured when the transmitter and receiver antennas are aligned perpendicular to one another hence the perpendicular electric field component is measured. There is no DSO measurement for this pulse.

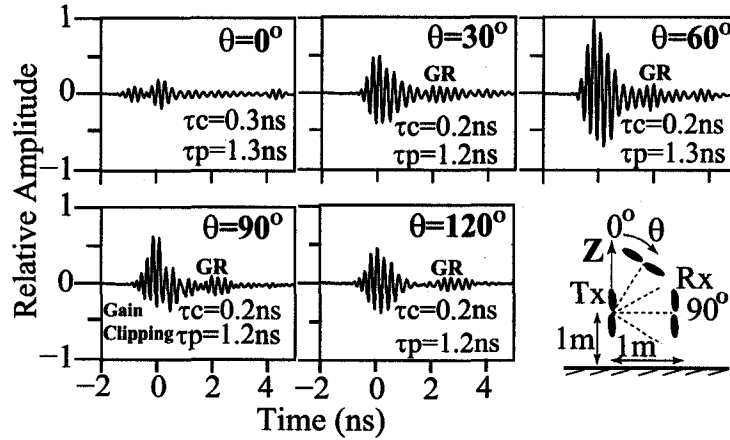


Figure 3.3. The change in radiated pulse shape as a function of elevation angle.

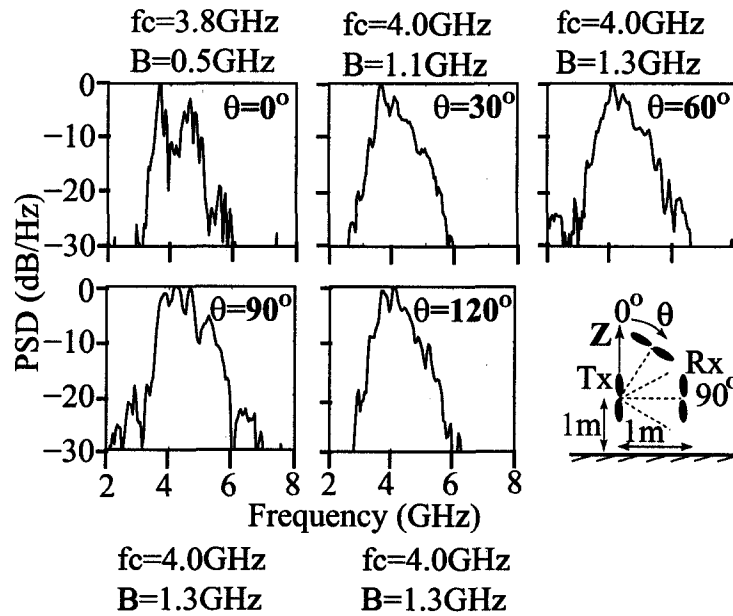


Figure 3.4. The change in radiated pulse spectrum as a function of elevation angle.

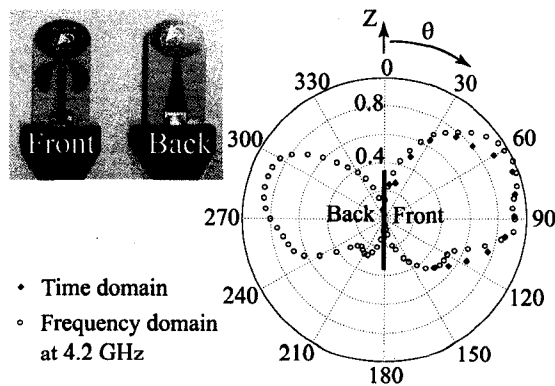


Figure 3.5. Radiation pattern of the PulsON 200TM Broadspec antenna. The frequency domain measurement at 4.2 GHz in the anechoic chamber shows a asymmetric pattern with a peak at $\theta = 65^\circ$. The peak amplitude of the received UWB waveform as a function of polar angle θ measured in the Taku parking lot when the transmitting and receiving antenna are 1 m above the ground and 1 m away from each other.

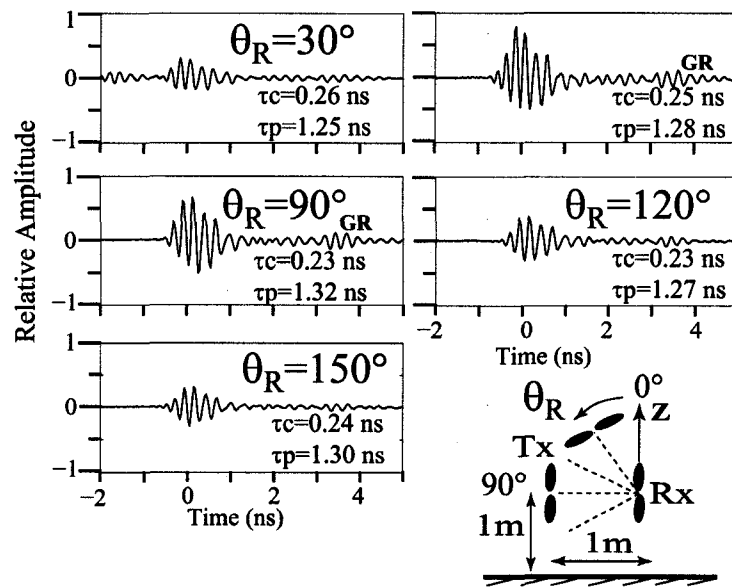


Figure 3.6. The change in time domain properties of received UWB pulse as a function of receiving angle θ_R .

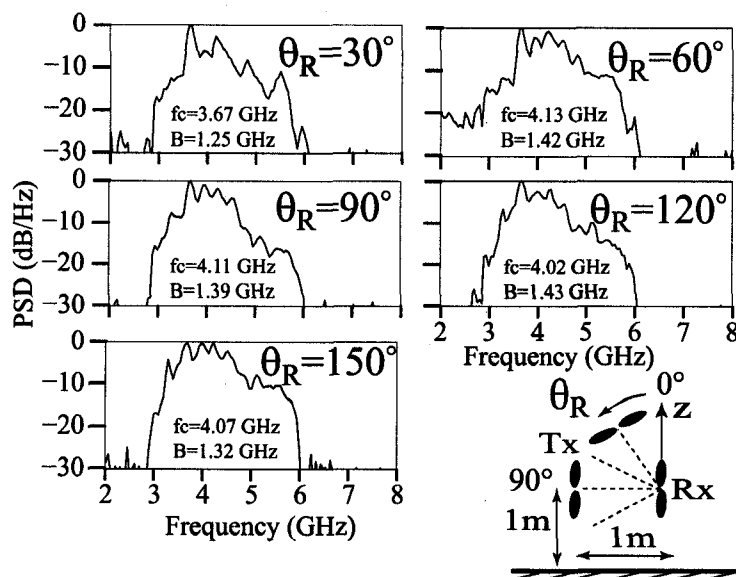


Figure 3.7. The change in frequency domain properties of the received UWB pulse as a function of receiving angle θ_R .

3.2.1.3 PulsON 200 Antenna Description and Measurements

Results from Chapter 2 clearly indicate that the radiated pulse properties depend on the direction of radiation and the configuration and geometry of the transmitting antenna. Hence it is expected that the pulse arriving at the receiver by the direct path and the one arriving by the reflected path may have different properties. Therefore it is important to study the directional properties of the transmitting and the receiving antennas. Figure 3.3 shows the 16-pulse average waveform received as a function of the elevation angle θ for the measurements performed in the Taku parking lot. In most instances the ground reflected pulse (GR) does not overlap with the direct pulse, permitting measurement of the directional properties of the transmitted pulse. The peak of the radiation pattern occurs for $\theta \sim 65^\circ$. The temporal properties of the pulses as a function of angle do not change significantly. The change in the pulse width is within 10% of ~ 1 ns and the change in the cycle time remains within 10% of 0.25 ns. Figure 3.4 shows the spectra of the pulses shown in Figure 3.3. Note that the frequency domain properties (i.e. pulse center frequency and the bandwidth)

also remain roughly constant with changes in the radiation angle. The change in the pulse center frequency is within 10% of 4.2 GHz and the change in the bandwidth is within 10% of 2 GHz. Figure 3.5 shows the radiation pattern of the PulsON 200 antenna measured by two methods. The open circles give the frequency domain measurement at 4.2 GHz. The transmitting and receiving antennas were connected to the ports of an Agilent E8358A PNA Series Vector Network Analyzer (VNA) and the entire assembly was placed in the anechoic chamber. The receiving antenna was revolved around the transmitting antenna in the vertical plane to obtain the radiation pattern. At each location the receiving antenna was oriented perpendicular to the direction of arrival of the pulse. The solid diamonds give the peak amplitude as a function of the elevation angle, θ . These measurements were performed using PulsON 200 transceivers in the Taku parking lot at UAF. The transmitting antenna was oriented vertically over the ground. The receiving antenna was oriented in the vertical plane perpendicular to the direction of arrival (see the lowermost right panel of Figure 3.3). The radiation patterns indicated by both the open circles and solid diamonds show peaks at $\theta \sim 65^\circ$ and a -3 dB beamwidth of $\sim 75^\circ$. Either type of radiation pattern measurements show asymmetry in the radiation pattern, i.e. the peak is not at $\theta = 90^\circ$. This is related to the asymmetry in the geometry of the antenna as shown in Figure 3.5. The asymmetric antenna geometry is employed to avoid near field coupling between the radiating oval elements and the feeding structure (balun transformer) [Schantz, 2003].

The experiments shown in Figures 3.3 to 3.5 relate the PulsON 200 antenna geometry to the time and frequency domain properties of the radiated UWB pulse. Figures 3.6 and 3.7 show the change in the time and frequency domain properties of the received UWB waveform as a function of the direction of arrival, θ_R . These measurements were performed using PulsON 200 transceivers in the Taku parking lot at UAF. The receiving antenna was oriented vertically 1 m above the ground. The transmitting antenna was oriented in the vertical plane perpendicular to the direction of radiation such that its broadside direction points at the receiving antenna. The transmitting antenna is rotated in the vertical plane and the received UWB voltage pulse for $\theta_R = 30^\circ, 60^\circ, 90^\circ, 120^\circ$ and 150° is shown in

the schematic in Figure 3.6. The time duration of the received pulse as a function of the direction of arrival remains within 10% of 1.25 ns and the change in the cycle time remains within 10% of 0.25 ns. Figure 3.7 shows the spectra of the pulses shown in Figure 3.6, indicating that the change in the pulse center frequency remains within 10% of 4 GHz and the change in the bandwidth remains within 10% of 1.4 GHz.

3.2.1.4 Measurement of the Peak Amplitude of the Received UWB Pulse

This subsection describes the measurement of the peak amplitude of the received pulse that is composed of pulses that reach the receiver by the direct and reflected paths, as illustrated in Figure 3.1. A single reflecting surface is an idealization and, as discussed in the next subsection, the experimental results show evidence of a layered ground. However, when only the first two pulses arriving at the receiver are considered, it may be assumed that the ground is a surface or wall of infinite thickness in the transverse direction.

The peak amplitude (16-pulse average) of the captured waveform as a function of the horizontal distance between the transmitter and the receiver was measured. A convenient way to describe this measurement is to define a relative signal strength (RSS), in dB, that relates the peak signal amplitude at a distance d ($V_G(d)$) to that measured in the anechoic chamber at a reference distance of one meter (V_{ref}):

$$RSS(d) = 20 \log \frac{V_G(d)}{V_{ref}} \quad (3.1)$$

Note that relative path loss (RPL), another commonly used variable to describe signal strength, is the negative of RSS(d) given in dB. The peak signal level measured at $d = 1$ m in the anechoic chamber was $V_{ref} \approx 6.7$ mV. This value can be used with the measured RSS to determine the peak signal level in mV for any given d using the following equation.

$$V_G(d) = V_{ref} 10^{RSS(d)/20} \quad (3.2)$$

It is possible to provide a rough estimate of the absolute value of the measured electric

field. Assuming the antenna effective length to be 2.15 cm, half the physical length, the peak electric field in the anechoic chamber at 1 m separation distance between transmitter and receiver was $\sim 6.7 \text{ mV} / (0.023) \text{ m} = 336 \text{ mV/m}$. Using this value for the electric field, the measured 3 dB beam width of $\sim \pi/2$ in the vertical plane and isotropic beam in azimuth, 1 ns pulse duration, and 9.6 MHz pulse repetition rate, the estimated average radiated power from the PulsON200TM transmitter is $\sim 14 \mu\text{W}$, a factor of 3.5 less than the nominal radiated power of $50 \mu\text{W}$ listed by the manufacturer.

As seen in the bottom panel of Figure 3.8, three characteristic propagation regimes can be clearly identified. For the first few meters ($\leq 3\text{-}4 \text{ m}$), in a region labeled ‘Little or no Overlap’, the signal power monotonically decreases as $\sim d^{-2}$ (RPL increases as $\sim d^2$), as shown by the dashed line labeled d^{-2} . The top left panel shows the captured waveform at $d = 3 \text{ m}$, showing that the direct pulse (first pulse) and the reflected pulse do not overlap.

For the next $\sim 15 \text{ m}$, from $\sim 4\text{-}20 \text{ m}$, in a region labeled ‘Partial but Significant Overlap’ in the bottom panel of Figure 3.8, the received signal exhibits fading, which depends on the relative phases of the direct and ground reflected UWB pulses. The signal amplitude reaches a final maximum at $\sim 18 \text{ m}$. The top middle panel of Figure 3.8 shows that the duration of the captured waveform at $d = 7.6$, is $\sim 1.7 \text{ ns}$, which is greater than the transmitted pulse duration. This results from the partial overlap of the direct and reflected pulses.

Beyond the last maximum in the signal amplitude near 18 m, the RSS monotonically decreases with distance showing a $\sim d^{-4}$ dependence for signal power, as shown by the dashed line labeled d^{-4} . This region is labeled as ‘Complete Overlap’. The top right panel of the Figure 3.8 shows that the captured waveform, at $d = 24 \text{ m}$, is about the same duration as the transmitted pulse (the first pulse seen in the top left panel). This results from almost complete overlap of the direct and reflected pulses.

Figure 3.8 also shows RSS as a function of d obtained from a ray tracing program that calculates, using the method of images approach, the electric and magnetic fields at the receiver location [Venkatasubramanian, 2003]. We note that simulations reproduce salient features of the measurements including three propagation regimes and the maxima and

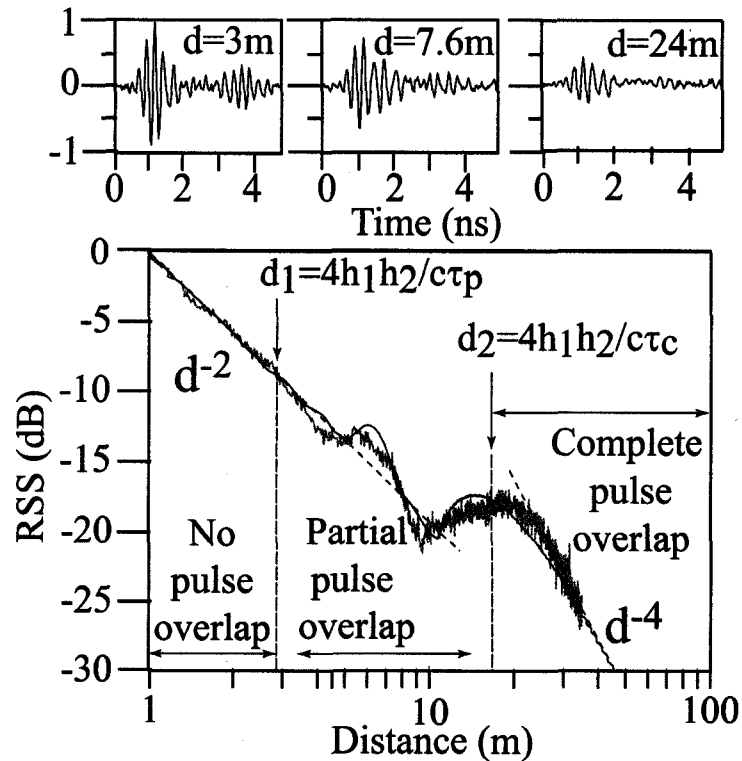


Figure 3.8. The relative path loss as a function of separation distance between the transmitter and the receiver held at 0.5 m above the ground. The bottom panel shows the measured relative path loss (dB) versus separation distance. The dotted (lighter) curve represents the measured data and the darker curve shows the relative path loss calculated from a two-ray model. The measured relative path loss can be categorized into three propagation regimes: (1) Little or no overlap, where the peak power falls approximately as d^{-2} (dashed line), (2) Partial but significant overlap, where the peak power shows fading maxima and minima, (3) Complete overlap, where the peak power falls approximately as d^{-4} (dashed line). The top panel shows the received UWB waveforms at three different locations indicating (i) no overlap (top, left); (ii) partial overlap (top, middle); and (iii) complete overlap (top, right), of the direct and reflected UWB waveform. All three waveform captures in the top panel are normalized to the peak amplitude of the total received waveform.

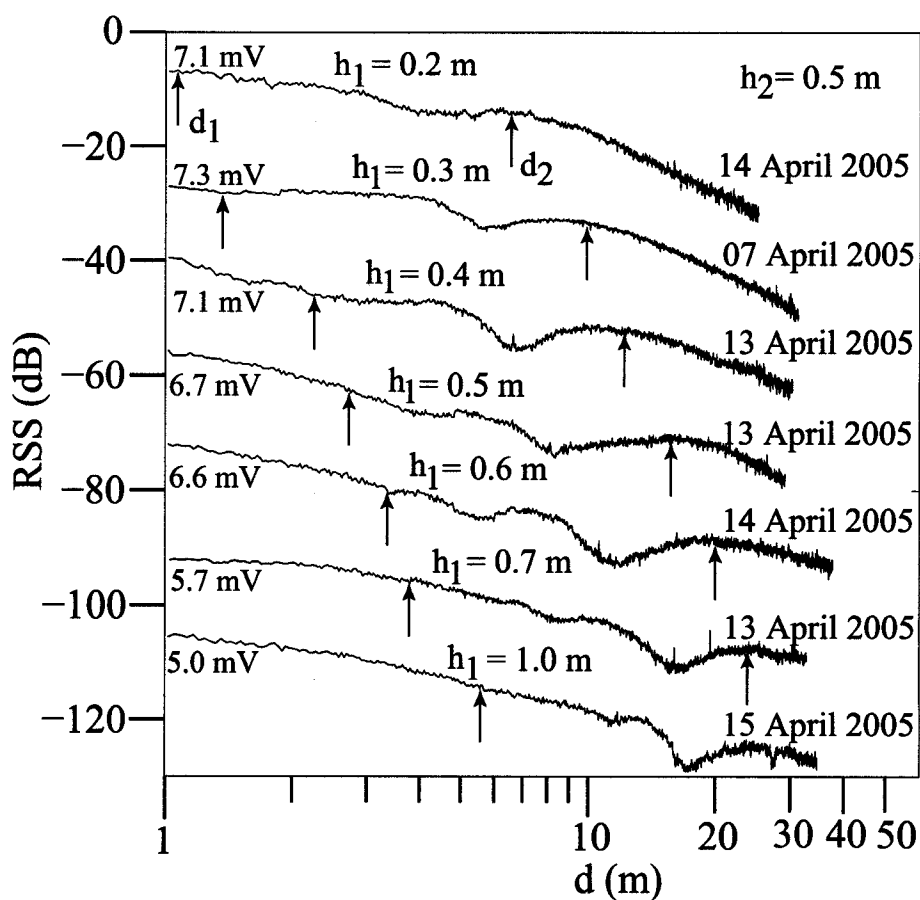


Figure 3.9. Path loss measurement as a function of separation distance between the PulsON200 transmitter and receiver. The transmitting antenna height is varied from $h_1 = 0.2 - 1.0$ m while the receiving antenna height is fixed at $h_2 = 0.5$ m. The receiver locks on to the peak field value of the received pulse after averaging over 16 pulses. Also indicated are the two breakpoints d_1 and d_2 as departures from the d^{-2} and d^{-4} lines.

minima in regime two.

Measurements similar to those shown in Figure 3.8 were carried out as the relative locations of the transmitter and the receiver with respect to each other and with respect to the ground were varied. For all cases the RSS as a function of the horizontal distance between the transmitter and receiver showed features similar to those noted above: three characteristic propagation regimes were found, the first one in which RSS decreased monotonically as d^{-2} , followed by the one in which RSS showed constructive and destructive fading, and the last one in which RSS decreased monotonically as d^{-4} . Figure 3.9 shows RSS versus separation distance d between the two PulsON 200TM transceivers for a fixed receiver height $h_2 = 0.5$ m and for a number of transmitter heights ranging from 0.2 m to 1.0 m.

It is possible to assign characteristic length scales d_1 and d_2 , called the first and second breakpoint distances, that determine the sizes of the three propagation regimes. Section 3.2.2 will theoretically derive these characteristic lengths which depend both on the geometrical parameters (h_1 , h_2 , and d) as well as on UWB pulse properties (τ_p and τ_c , or equivalently B and f_c). It should be noted here that the second break point distance is well known for narrowband (NB) signals propagating over the ground and extensive literature exists on the subject (e.g., see [Bertoni, 2000] and references therein). We also note that recently, Liu *et al.* [2006] observed an unsteady breakpoint in their path loss calculations for short separation distances (≤ 5 m) between the transmitter and receiver.

3.2.1.5 Multiple Reflections from a Layered Ground

The results presented thus far were based on the overlap of the direct and the reflected pulse from the top face of the reflecting surface. This is tantamount to assuming that the surface is semi-infinite. Most surfaces (e.g., wall, ground) are layered. For layered surfaces, multiple primary reflections result, one from each boundary, and then multiple secondary and tertiary reflections from bouncing of waves between individual layers. Figure 3.10 shows three specific cases of received voltage waveform for a pair of P200 transceivers held at 0.5 m

above the ground in the Taku parking lot. The received voltage waveform, captured by the PAT software, showed multiple reflections from layers of snow and ice on the ground in the Taku parking lot. Figure 3.10A shows four distinct pulses, one direct path pulse and three reflected pulses from the multiple layers of snow and ice on the ground. The amplitude and shape of the reflected pulses depend on the electrical properties and the thickness of the various layers. These type of pulses can indicate presence of snow layers on the ground and can be used to calculate the thickness and electrical properties of the snow layers above the ground.

Figure 3.10B shows one direct path pulse and one reflected pulse which is longer in time duration compared to the direct path pulse. This suggests that the pulse reflected from the top and bottom surfaces of the top layer above the ground add and subtract causing a resultant pulse with a time duration longer than the original transmitted pulse. These type of pulses indicate presence of a snow layer on the ground but do not provide information regarding the thickness of the snow layer above the ground. Figure 3.10C shows one direct path pulse and one reflected pulse, both having the same time duration. These type of pulses provide an estimate of the electrical properties of the ground indicating an absence of snow layer on the ground.

3.2.2 Theoretical Formulation

3.2.2.1 A General Time and Frequency Domain Representations of UWB Multipath Propagation

The UWB literature does not provide a time and frequency domain representation of UWB pulses, direct and multiply reflected, that takes into account the wave polarization, the amplitude spectrum, and the reflection coefficient (reflecting surface properties), that will be useful for analytical and numerical development. One such formulation is provided in this section.

This section investigates the propagation of a UWB pulse over a plane reflecting surface. Figure 3.1 shows the geometry of the analysis. For a source of UWB radiation located at

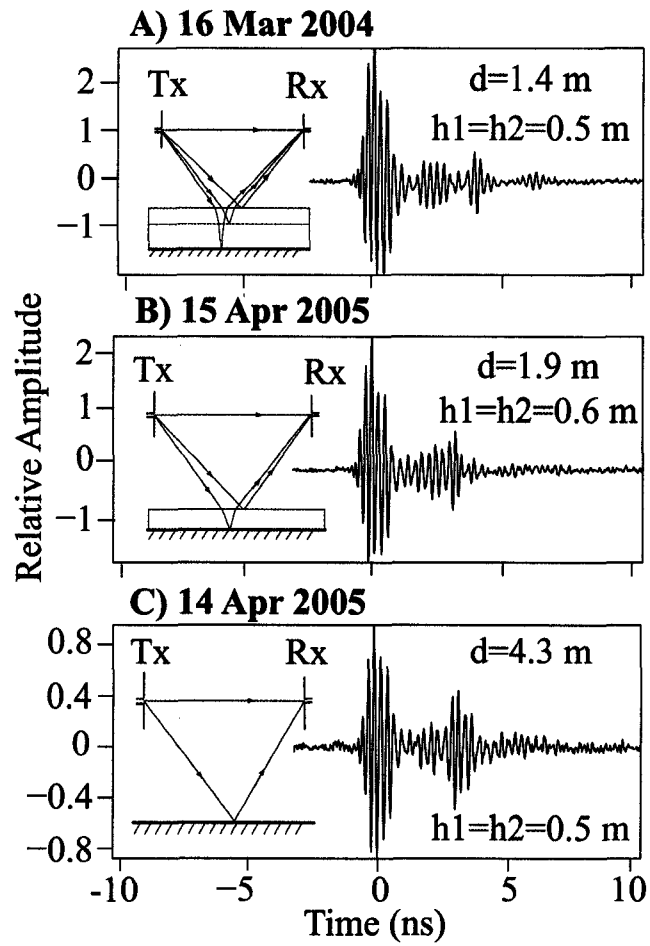


Figure 3.10. Four different types of received voltage waveforms measured by the PulsON 200 receiver in the Taku parking lot measurement.

the origin, the electric field $\mathbf{e}(r, \theta, \phi, t)$ in free space at a point (r, θ, ϕ) in the far field region can be described as follows:

$$\mathbf{e}(r, \theta, \phi, t; \hat{\mathbf{a}}_{\mathbf{T}}) = \sum_{i=1}^2 \frac{e_{0i}(t - r/c, \theta, \phi; \hat{\mathbf{a}}_{\mathbf{T}}) r_0}{r} \hat{\mathbf{p}}_i(\theta, \phi) \quad (3.3)$$

where $e_{0i}(t - r/c, \theta, \phi, \hat{\mathbf{a}}_{\mathbf{T}})$ refers to the UWB pulse electric field components at (r_0, θ, ϕ) in the two mutually perpendicular directions $\hat{\mathbf{p}}_i$, $i = 1, 2$ in the plane perpendicular to the direction of propagation (θ, ϕ) , and $c \approx 3 \times 10^8$ m/s is the speed of light. The vector $\hat{\mathbf{a}}_{\mathbf{T}}$ represents antenna orientation vector which includes the antenna axis and any rotation around this axis. The vector $\hat{\mathbf{a}}_{\mathbf{T}}$ is included in the functional dependence of the electric field to indicate that pulse-radiation from a UWB antenna depends both on the direction of propagation as well as antenna orientation (see Section 3.2.1.3). The UWB electric field representation given in Equation 3.3 takes into account that the far field electric field of an arbitrary source of electromagnetic radiation is transverse. Within the limitation that Equation 3.3 represents far field, this expression is general. In particular, Equation 3.3 allows for different pulse shapes in different directions as expected for a UWB antenna [Venkatasubramanian *et al.*, 2007]. There are certain restrictions on the allowed forms of $e_{0i}(t, \theta, \phi)$. Assuming that the pulse was transmitted at $t = 0$ from a UWB source located at the origin, the following conditions must be satisfied:

$$e_{0i}(t, \theta, \phi; \hat{\mathbf{a}}_{\mathbf{T}}) = 0, \quad t < 0 \quad (3.4a)$$

$$\int_0^{\infty} e_{0i}(t, \theta, \phi; \hat{\mathbf{a}}_{\mathbf{T}}) dt = 0, \quad \text{No DC component} \quad (3.4b)$$

$$\int_0^{\infty} e_{0i}^2(t, \theta, \phi; \hat{\mathbf{a}}_{\mathbf{T}}) dt < \infty, \quad \text{Finite energy} \quad (3.4c)$$

If

$$e_{0i}(r, \theta, \phi, t) = \int_{-\infty}^{\infty} E_{0i}(f, \theta, \phi; \hat{\mathbf{a}}_{\mathbf{T}}) e^{j2\pi ft} df \quad (3.4d)$$

then $|E_{0i}(f, \theta, \phi)|$ should satisfy UWB spectrum limitations specified by the FCC [2002].

It is assumed that both the receiving antenna and the reflecting surface are in the far field of the transmitting antenna. The conditions for the far-field approximation can be obtained as follows. For a radiated narrow band signal, the far field assumption requires that $r \gg \lambda, l$, and $r > 2l^2/\lambda$, where l is the largest dimension of the transmitting antenna and λ is the wavelength of the signal [Kraus and Marhefka, 2001]. For a radiated UWB pulse we can estimate the far field distance by assuming $\lambda \sim 4.4$ cm, wavelength at 6.85 GHz, roughly the center of the UWB band, and $l \sim \lambda/2$. We obtain $2l^2/\lambda = 2.2$ cm.

It is convenient to write the Fourier domain representation of the transmitted pulse $e_{0i}(t)$.

$$\mathbf{e}(r, \theta, \phi, t; \hat{\mathbf{a}}_{\mathbf{T}}) = \sum_{i=1}^2 \int_{-\infty}^{\infty} \frac{E_{0i}(f, \theta, \phi; \hat{\mathbf{a}}_{\mathbf{T}}) r_0}{r} \hat{\mathbf{p}}_i(\theta, \phi) e^{j(2\pi ft - kr)} df \quad (3.5)$$

Without any loss of generality, the geometry shown in Figure 3.1 is considered. In the z - x plane the locations of Tx and Rx are given by $(0, h_1)$ and (d, h_2) , respectively. The signal reaches the receiver via a direct path and via a reflected path as shown in the figure. The plane of incidence is given by the vector joining Tx and Rx and the direction of the normal ($\hat{\mathbf{n}}$) to the surface. In this plane, the directions of propagation of the direct and ray incident on the surface are described by the angles ψ_D and ψ_R , respectively. Since in the z - x plane, the azimuthal angle $\phi = 0$ we shall omit any further explicit reference to it. For the geometry shown in the Figure 3.1, it is convenient to choose $\hat{\mathbf{p}}_1$ to be in the plane of incidence ($i = 1$, TM) and in the plane perpendicular to the plane of incidence ($i = 2$, TE). The electric field of the signal arriving at the receiver by the direct path is given by

$$\mathbf{e}_{\mathbf{D}}(d, h_2, t; h_1, \hat{\mathbf{a}}_{\mathbf{T}}) = \sum_{i=1}^2 \frac{e_{0i}(t - D/c, \psi_D; \hat{\mathbf{a}}_{\mathbf{T}}) r_0}{D} \hat{\mathbf{p}}_i(\psi_D) \quad (3.6)$$

where $D = \sqrt{(h_1 - h_2)^2 + d^2}$ and $\psi_D = \tan^{-1}((h_1 - h_2)/d)$.

Because the reflection coefficient depends on frequency, it is helpful to use frequency domain representation, to describe the electric field of the signal arriving at the receiver by the reflected path.

$$\mathbf{e}_R(d, h_2, t; 0, h_1, \hat{\mathbf{a}}_T) = \sum_{i=1}^2 \int_{-\infty}^{\infty} \frac{E_{0i}(f, \psi_R; \hat{\mathbf{a}}_T) r_0}{D'} \Gamma_i(\psi_R, f) \hat{\mathbf{p}}_i(\psi_R) e^{j(2\pi ft - kD')} df \quad (3.7)$$

where $D' = \sqrt{(h_1 + h_2)^2 + d^2}$, $\psi_R = \tan^{-1}((h_1 + h_2)/d)$ and $\Gamma_i(\psi, f)$ is the reflection coefficient for TM ($i = 1$) and TE ($i = 2$) polarization.

It is possible to give an image source representation for the reflected signal. We consider an image source T'_X of the transmitter located at a distance h_1 below the surface. The distance between the image and the receiver is D' , which gives the total spreading of the reflected signal. The line joining the image source to the receiver R_X makes an angle ψ_I with the reflecting surface (x -axis) such that

$$\psi_I = \psi_R \quad (3.8)$$

Let

$$e_{0i}^I(t, \psi_I; h_1, \hat{\mathbf{a}}_T) = \int_{-\infty}^{\infty} E_{0i}(\psi_R, f; h_1, \hat{\mathbf{a}}_T) \Gamma_i(\psi_R, f) e^{j2\pi ft} df \quad (3.9)$$

Then,

$$\mathbf{e}_R(d, h_2, t; h_1, \hat{\mathbf{a}}_T) = \sum_{i=1}^2 \frac{e_{0i}^I(t - D'/c, \psi_I; h_1, \hat{\mathbf{a}}_T) r_0}{D'} \hat{\mathbf{p}}_i(\psi_R) \quad (3.10)$$

Equation 3.10 has a simple interpretation. The reflected signal at the receiver is direct signal from an image source located at h_1 below the surface and with radiated pulse given

by Equation 3.9, which in turn relates radiation properties of the image source to the transmitter pulse and the reflection coefficients of the surface for the two polarizations.

The total field at the receiver is the sum of the direct and reflected pulses: $\mathbf{e}_D + \mathbf{e}_R$. Both the direct and reflected pulses have two components, one in the plane of incidence and one normal to it.

$$\mathbf{e}(d, h_2, t; h_1, \hat{\mathbf{a}}_T) = \mathbf{e}_D(d, h_2, t; h_1, \hat{\mathbf{a}}_T) + \mathbf{e}_R(d, h_2, t; h_1, \hat{\mathbf{a}}_T) \quad (3.11)$$

Equation 3.11 states that the total electric field at the receiver is sum of the direct and reflected pulses. Each of these pulses has two orthogonal polarizations, which add independently. For each polarization, the pulse shape and peak amplitude will be different for direct and reflected pulses. The direct and reflected pulses arrive at the receiver with time delays D/c and D'/c , respectively. Depending on the differential time delay, $(D' - D)/c$, the direct and reflected pulse may or may not overlap. In order to study how the electric field of the direct and the reflected pulses add, it is convenient to consider the electric field component in one direction: the z -component. We shall find that an exactly analogous analysis can be carried out for the x -component, and that similar results will be obtained.

Past measurements of the complex dielectric constant for commonly found wall materials in indoor propagation environments showed that the real part of the complex dielectric constant shows a 5% deviation from the mean value across the 1-15 GHz frequency range indicating that ϵ can be regarded as independent of the transmission frequency [Davis *et al.*, 2007; Muqabeil, 2003]. The value of the relative dielectric constant remains the same within 5% over the UWB range, σ is constant over the UWB range, and this gives a complex reflection coefficient whose amplitude is the same within 10% and whose phase is linear within 5%, except at the points of inflections where the phase errors of the order of 40% to 50% are calculated. Our calculations show that in the UWB frequency range, the cycle time of the reflected pulse waveform changed by $< 3\%$ from the cycle time of the incident pulse waveform incident on a dry ground with $\epsilon_r = 15$ [Bertoni, 2000] and σ varying from 0.001 S/m to 0.1 S/m.

Hence our calculations show that on the average it can be assumed that the reflection coefficient of a lossy, homogenous reflecting surface is roughly constant over the UWB frequency range at all angles of incidence. Hence $\Gamma(\psi, f) \approx \Gamma(\psi)$ and the transmitted and reflected pulse wave forms are related by simple expressions

$$e_z(d, h_2, t, \hat{\mathbf{a}}_{\mathbf{T}}) = \frac{e_{01}(t - D/c, \psi_D, \hat{\mathbf{a}}_{\mathbf{T}})r_0}{D} \hat{\mathbf{p}}_1(\psi_D) \cdot \hat{\mathbf{z}} + \frac{e_{01}^I(t - D'/c, \psi_R, \hat{\mathbf{a}}_{\mathbf{T}})r_0}{D'} \hat{\mathbf{p}}_1(\psi_R) \cdot \hat{\mathbf{z}} \quad (3.12)$$

In general, the UWB antennas have a planar geometry. We can phenomenologically assign two effective lengths: one along the nominal axis of the antenna; and one perpendicular to it, which can be used to obtain the induced voltage across the antenna terminal. The effective lengths are represented by L_1 and L_2 . The voltage at the receiving antenna terminal is given by

$$v(d, h_2, t) = (L_1 \hat{\mathbf{a}}_{\mathbf{R}} + L_2 \hat{\mathbf{b}}_{\mathbf{R}}) \cdot \mathbf{e}(d, h_2, t, \hat{\mathbf{a}}_{\mathbf{T}}) \quad (3.13)$$

where $\hat{\mathbf{a}}_{\mathbf{R}}$ is a unit vector along the axis of the receiving antenna and $\hat{\mathbf{b}}_{\mathbf{R}}$ is a unit vector in the plane of the antenna and perpendicular to $\hat{\mathbf{a}}_{\mathbf{R}}$.

If it is assumed that the center frequency and the bandwidth of UWB pulses transmitted in various directions are roughly the same (even though the pulse amplitude may vary), then the principal features of the direct pulse and the reflected pulse will remain same within a constant amplitude factor that depends on both the direction of the radiated pulse and the angle of incidence. Note in the experimental section, this assumption was well satisfied for the PulsON 200 antenna. Recent work on an oval dipole antenna [Venkatasubramanian *et al.*, 2007] has shown that the center frequency and the bandwidth of the pulses radiated in different directions are within acceptable bounds for the presented results to hold true for a general case.

To summarize the results thus far, note that each component of the electric field consists

of two pulses, direct and reflected. At the receiver, these pulses generate voltage pulses. It is assumed that the voltage pulses possess the same general character as the electric field pulses. Thus the received signal is considered to be made up of two voltage pulses resulting from the reception of the direct and the reflected electric field pulses. These two voltage pulses have the same τ_c , as shown in Figure 3.8, but different pulse envelopes (shape and amplitude), and different time of arrival. The total signal is the sum of these two pulses. As discussed below, owing to the same τ_c , the resulting overlap of the direct and the reflected pulses can be considered as an in-phase or out-of-phase addition depending on the relative time delays as a fraction of $\tau_c/2$ (modulo $\tau_c/2$). Our analysis of the three propagation regimes is based on this fundamental result.

3.2.2.2 Theoretical Model of the Propagation Regimes: First and Second Breakpoints

The principal features of the data presented in the last section can be explained with the help of the two-ray theory. For the theory presented in this section, it is assumed that the receiver and the ground are in the far field of the transmitting antenna. It is also assumed that the transmitting and receiving antenna are isotropic and are oriented such that they transmit and receive vertically polarized electromagnetic waves. The transmitted UWB pulse is described by two parameters in the time domain: (1) pulse duration τ_p and (2) pulse cycle time τ_c . In general $\tau_p \geq \tau_c$. For a UWB pulse in the 3.1 GHz to 10.6 GHz range with no DC component we expect at least one cycle (one positive and one negative excursion of the field) to be present in the transmitted signal. In the frequency domain, let the pulse be characterized by a bandwidth B and center frequency f_c . The time domain and frequency domain parameters of the UWB pulse are approximately related as follows:

$$B \sim \frac{1}{\tau_p}; f_c \sim \frac{1}{\tau_c} \quad (3.14)$$

The exact relationship between the time and the frequency domain properties depends on the details of the pulse and the definitions of pulse width, cycle time, pulse bandwidth, and pulse center frequency [Bracewell, 1999]. The condition given by Equation 3.4b implies

that $t_p \geq 2\tau_c/2$ or $B \leq f_c$.

As shown in Figure 3.1, in the presence of a single reflecting surface there are two possible paths, direct and reflected, by which a UWB signal can reach the receiver. The path length of the direct signal is D , the distance between the transmitter T and the receiver R , and the path length of the reflected signal is D' , the distance between the image T' of the transmitter and the receiver R .

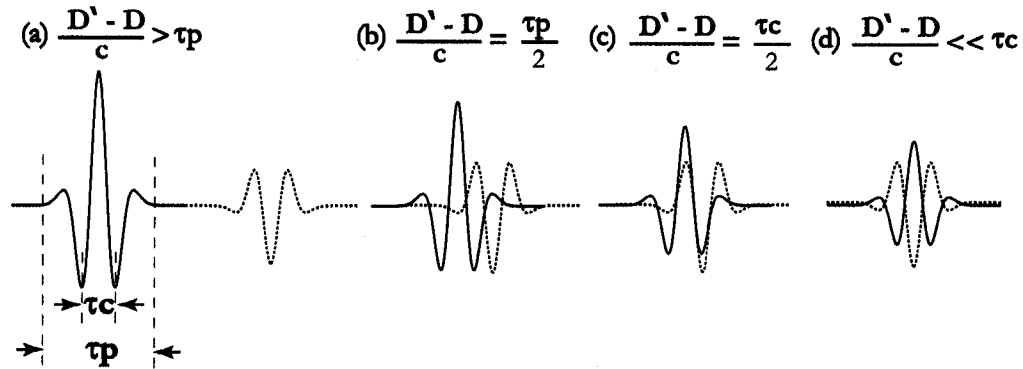


Figure 3.11. Schematic showing the overlap of the direct and reflected pulses in the time domain. The reflected pulse is shown in negative phase, resulting from negative value of reflection coefficient, with respect to the direct pulse. (a) The direct and reflected pulses do not overlap. The differential time delay is larger than the transmitted pulse duration. (b) and (c) The direct and reflected pulses partially overlap leading to constructive and destructive superposition. (d) The direct and reflected pulses completely overlap, adding in opposite phases.

Figure 3.11 schematically shows the signals arriving at the receiver. In free space the time delays for the direct and reflected signals are D/c and D'/c , respectively, where c is the velocity of light. Depending on the difference in the time delays, $(D' - D)/c$, of the signals arriving at the receiver from the direct and reflected paths relative to the pulse duration (τ_p) and cycle time (τ_c), three distinct propagation regimes can be identified (Figure 3.8). In the first regime, where $(D' - D)/c > \tau_p$, the direct and reflected pulses do not overlap. The peak received power in this regime should fall as D^{-2} , the same as that for propagation in free space (note that for $h_1, h_2 \ll d$, $D^{-2} \sim d^{-2}$). In the second regime, where $(D' - D)/c < \tau_p$, direct and reflected pulses partially overlap leading to constructive and

destructive superposition, depending on the relative path lengths. The peak received power in this regime should show fading maxima and minima. In the third regime, where $(D' - D)/c \ll \tau_c$, the direct and reflected pulses completely overlap. Due to the near grazing angle of incidence of the reflected ray, the direct and reflected signals have electric fields of about the same magnitude but opposite phase. Therefore, the electric fields of the direct and reflected pulses almost cancel out, leading to a $\sim d^{-4}$ variation in the peak power for the case when $h_1, h_2 \ll d$.

The boundary between the first and the second regime is defined as:

$$\text{Boundary1 : } (D' - D)/c = \tau_p/2 \quad (3.15)$$

This definition assumes that the significant overlap between the direct and the reflected pulses does not begin until at least half the duration of the reflected pulse overlaps with the direct pulse. This definition is reasonable for those UWB pulses that have a roughly bell shaped envelope, with relatively slow rise and fall times. For pulses with relatively sharp rise time, we may have to modify the right hand side of the above equation.

The boundary between the second and the third regime is defined as:

$$\text{Boundary2 : } (D' - D)/c = \tau_c/2 \quad (3.16)$$

For the case when $h_1, h_2 \ll d$, this definition provides a boundary on which the direct and reflected pulses add in phase, giving a maximum for one last time, before they begin to add in the opposite phase.

In the second regime, the direct and reflected pulses partially overlap, adding in phase or out of phase depending on both the path difference and the sign of the reflection coefficient. If it is assumed that the UWB pulse envelope is bell shaped, a maximum (Max) or minimum (Min) in the peak amplitude of the received pulse follows the relation:

$$\text{Max/Min : } (D' - D)/c = n\tau_c/2, \quad n = 1, 2, \dots, m, \quad (3.17)$$

where $m \sim \tau_p/\tau_c$. Case $n = 1$ gives the maximum identical to that given by Equation 3.16.

In Equations 3.15, 3.16, and 3.17, note that the left hand side term, $(D' - D)/c$, which is determined entirely by the geometry (h_1, h_2, d) , is equated to the properties of the pulses in the time domain. Other pulse characteristics, such as details of the pulse envelope and rise time (τ_r) , may be significant in determining the boundaries between various regimes. By the duality between the time and the frequency domain, the above boundaries can be equivalently defined in terms of frequency domain parameters of the pulse (e.g., center frequency (f_c) , bandwidth (B) , and sidelobe magnitude). To first order, Equation 3.14 can be used to obtain boundaries defined in terms of frequency domain properties of the UWB pulse.

$$\text{Boundary1 : } (D' - D)/c = 1/2B. \quad (3.18)$$

$$\text{Boundary2 : } (D' - D)/c = 1/2f_c \quad (3.19)$$

$$\text{Max/Min : } (D' - D)/c = n/2f_c, \quad n = 1, 2, \dots, m \quad (3.20)$$

There is a natural interpretation of boundaries defined by Equations 3.18-3.20. For example, if both sides of Equations 3.15 is multiplied by c , then

$$D' - D = c\tau_p/2 \quad (3.21)$$

The left hand side is the difference in distance of the receiver from two fixed points T and T' and the right hand side is a constant distance $c\tau_p/2$, which depends on the pulse width. Thus, this represents a hyperbola with T and T' as its two foci and the receiver R given by coordinates (d, h_2) lying on the hyperbola. Similarly, Equations 3.16 and 3.17 also represent hyperbolas. The expressions for these hyperbolas are given below.

$$\text{Boundary1 : } \frac{h_2^2}{c^2\tau_p^2} - \frac{d^2}{(16h_1^2 - c^2\tau_p^2)} = \frac{1}{16} \quad (3.22)$$

$$\text{Boundary2 : } \frac{h_2^2}{c^2\tau_c^2} - \frac{d^2}{(16h_1^2 - c^2\tau_c^2)} = \frac{1}{16} \quad (3.23)$$

$$\text{Max/Min : } \frac{h_2^2}{c^2n^2\tau_c^2} - \frac{d^2}{(16h_1^2 - c^2n^2\tau_c^2)} = \frac{1}{16} \quad (3.24)$$

where, $n = 1, 2, \dots, m$.

Note that Equations 3.22 - 3.24 require that $h_1 > c\tau_p/4$, $nc\tau_c/4$. For $h_1 < c\tau_p/4$, the first regime (no overlap) does not exist, and only partial or complete overlap occurs for all values of h_2 and d ; for $h_1 < c\tau_p/4$, even the second regime does not exist and almost complete overlap occurs for all values of h_2 and d .

The asymptotic forms of Equations 3.22, 3.23, and 3.24 which are generally valid when $h_1, h_2 \gg c\tau_p/4$, $nc\tau_c/4$ and $d \gg h_1$, are given by

$$d \approx \frac{4h_1h_2}{c\tau_p} \approx \frac{4h_1h_2B}{c} \quad (3.25)$$

$$d \approx \frac{4h_1h_2}{c\tau_c} \approx \frac{4h_1h_2f_c}{c} \quad (3.26)$$

$$d \approx \frac{4h_1h_2}{cn\tau_c} \approx \frac{4h_1h_2f_c}{nc}, \quad n = 1, 2, \dots, m \quad (3.27)$$

3.2.2.3 Extension of the Theoretical Model to Finite Wall case for LOS and NLOS propagation

UWB is considered a viable technology for communication in cluttered propagation environments. Past work in narrow band signal propagation has shown that, for outdoor environments, complex finite wall structures can result in a path loss difference of 8-10 dB [Holloway *et al.*, 1997], and, for indoor environments, the delay spread of the propagation

channel is sensitive to the structure and the electrical properties of the walls present in the environment [Zhang and Huang, 2002].

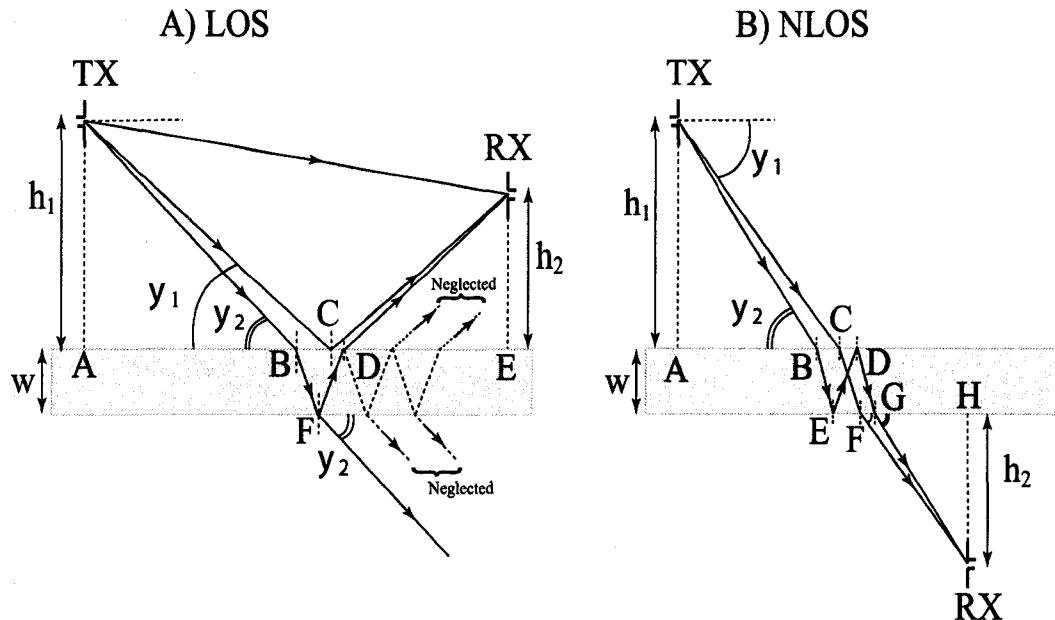


Figure 3.12. Schematic showing the geometry of UWB pulse propagation in the presence of a single finite thickness reflecting surface for LOS and NLOS cases. (A) LOS case - Schematic showing two reflected paths reaching the receiver (RX) from a transmitter (TX) from the top face of the wall (TX-C-RX) making an angle ψ_1 with the wall surface and from the bottom face of the wall (TX-B-F-D-RX) making an angle ψ_2 with the wall surface. (B) NLOS case - Schematic showing two transmitted paths reaching the receiver, one direct (TX-C-F-RX) making an angle ψ_1 with the wall surface and one after two bounces (TX-B-E-D-G-RX) inside the wall making an angle ψ_2 with the wall surface. The transmitter and receiver are located at heights h_1 and h_2 , respectively, from the reflecting surface and separated by a distance d .

The wavelength of UWB signals ranges from 3 cm to 10 cm. The higher order reflections (resonances) inside the wall traverse a path length equal to several wavelengths before reaching the receiver. In our calculations of the time delay difference, $\Delta\tau$, the following assumptions were made: (1) only the first order reflection inside the wall for the line-of-sight (LOS) case (Figure 3.12A) and the first order transmission and second order reflection inside the wall for the non-line-of-sight (NLOS) case (Figure 3.12B) are considered; (2) the

properties of the radiated pulse do not change for the two aforementioned paths; and (3) the transmission angles for the two paths from the axis along the length vector of the radiating antenna are the same ($\psi_1 = \psi_2 = \psi$) or $CB/CA \ll 1$. These assumptions are valid when the wall thickness $w \ll d$, $\sqrt{n^2 - 1} \sim O(1)$ and $h_1/h_2 \sim O(1)$.

Two cases are considered:

1) When the transmitter and the receiver are on the same side of a finite thickness wall - LOS case

Consider the time difference of arrival, $\Delta\tau$, of the electric field pulse reaching the receiver after reflection from the top face (path TX-C-RX) and the bottom face (path TX-B-F-D-RX) of the wall as shown in Figure 3.12A.

$$\Delta\tau = \frac{2nw}{c} \sqrt{\frac{(n^2 - 1)d^2 + n^2(h_1 + h_2)^2}{n^2(d^2 + (h_1 + h_2)^2)}} \quad w \ll d \quad (3.28)$$

$$\Delta\tau = \frac{2nw}{c} \quad d = 0, \text{ normal incidence} \quad (3.29)$$

$$\Delta\tau = \frac{2w\sqrt{n^2 - 1}}{c} \quad d \gg h_1, h_2, \psi \rightarrow 0^\circ, \text{ grazing incidence} \quad (3.30)$$

where n is the refractive index of the wall, w is the wall thickness, d is the transmitter-receiver separation distance, and h_1 and h_2 are the transmitter and receiver heights from the reflecting wall surface.

2) When the transmitter and the receiver are on opposite sides of a finite thickness wall - non-line-of-sight. The time difference of arrival, $\Delta\tau$, of the electric field pulse reaching the receiver from the two transmitted rays, one direct (path TX-C-F-RX) and one after two

bounces (path TX-B-E-D-G-RX) inside the wall as shown in Figure 3.12B.

$$\Delta\tau = \frac{2n^2w}{c\sqrt{n^2 - \cos^2\psi}} \quad w \ll d \quad (3.31)$$

$$\Delta\tau = \frac{2nw}{c} \quad d = 0, \psi = 90^\circ \text{ normal incidence} \quad (3.32)$$

$$\Delta\tau = \frac{2w\sqrt{n^2 - 1}}{c} \quad d \gg h_1, h_2, \psi \rightarrow 0^\circ, \text{ grazing incidence} \quad (3.33)$$

For the above two cases, the overlap of the electric field pulses reaching the receiver from two propagation paths due to a finite wall depends on the width of the wall w , the electrical properties of the wall (ϵ_r, σ) , and the radiated pulse properties (τ_p, τ_c, f_c, B) . For $\Delta\tau > \tau_p$ there is no overlap between pulses reaching the receiver from two different propagation paths and hence both d_1 and d_2 are unaffected as $\tau_c \leq \tau_p$. For $\Delta\tau < \tau_p$ there is overlap between pulses reaching the receiver from two different propagation paths. For small d , the pulse overlap affects the first break point distance d_1 . But as d increases the reflection coefficient of the wall $\Gamma_w \rightarrow -1$ and hence the path through the wall is very weak to make any significant contribution to the overall electric field pulse at the receiver. Hence d_2 remains unaffected for most values of time delay.

Most walls inside buildings are ~ 5 cm to 30 cm thick [Bertoni, 2000]. For example, for the LOS case, the time delay difference for the PulsON200TM waveform ($\tau_p = 1.25$ ns, $\tau_c = 0.2$ ns) normally incident ($d=0$) on a 5 cm concrete wall ($\epsilon_r = 6$, $\sigma = 0.01$) [Bertoni, 2000] is ~ 0.8 ns. In comparison to a semi-infinite concrete wall, the above mentioned case would cause an elongation in the second propagation regime due to constructive and destructive interference of the direct and the reflected pulses but the second breakpoint remains unaffected. This result agrees with previous numerical work by Heidary [2004] on UWB pulse reflection from a three layer lossy wall. His results showed that the τ_c of the overall reflected pulse waveform remains the same within 5% but the τ_p of the pulse changes by up to three times the original pulse width depending on thickness and properties of the various wall layers. It should also be noted that structures present inside the wall (eg. metal studs) could result in a strong reflection reaching the receiver and hence could also affect

the first breakpoint distance.

3.2.2.4 Comparison of the Theoretical model with Experiments

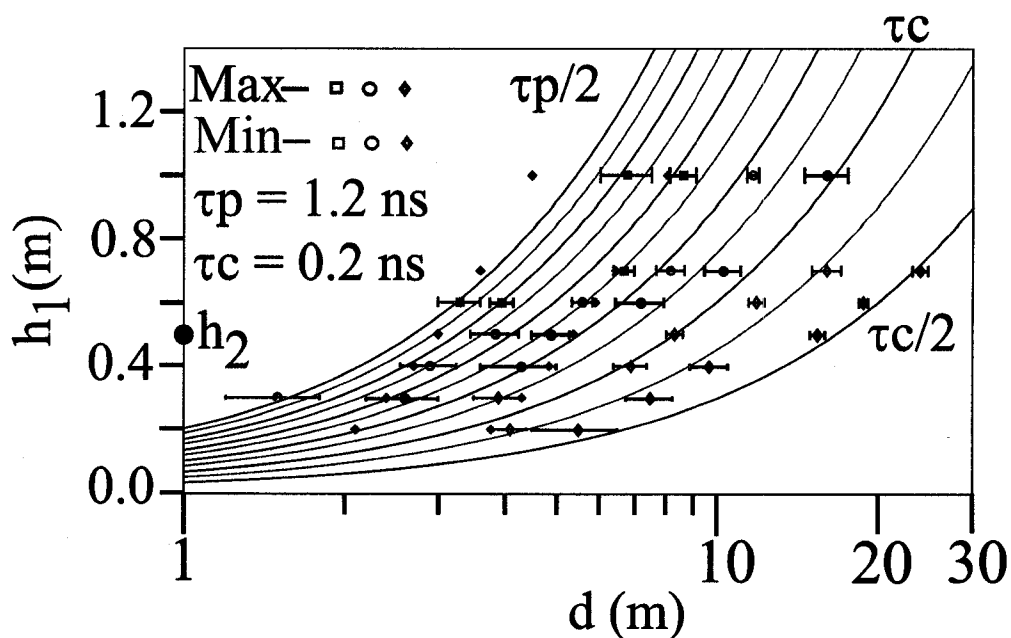


Figure 3.13. Comparison between the the maxima and minima distance predicted by the hyperbola model and measured from the signal strength data. The solid black and red lines show the hyperbolas corresponding to maxima and minima in the peak amplitude of the received voltage when the time difference between the direct and the reflected path pulses is $\Delta = n\tau c/2$. The measured maxima and minima in the path loss curves are shown as black (maxima) and red (minima) squares (first), circles (second) and diamonds (third) respectively starting from the closest distance between the transmitter and receiver. The transmitter height h_1 is varied from 0.2 m to 1.0 m. The receiver height h_2 is held fixed at 0.5 m (shown by filled black circle). The measurements are done using the PulsON200 UWB transceivers. The transmitted pulse has pulse width $\tau_p = 1.2$ ns and cycle time $\tau_c = 0.2$ ns.

Figure 3.13 shows the comparison of the hyperbolas calculated using the theoretical model with the measured data. The receiver and its image on the other side of the reflecting surface (ground) are located on the two foci of the hyperbola. The transmitter is located on the hyperbola curves. The red curves show the minima and the black curves show the

maxima as the separation distance between the transmitter and receiver is changed. The black and the red diamonds, circles and squares show the maxima and minima measured from the received signal strength curves using the approach detailed in Appendix B.3. The measured maxima and minima locations show excellent agreement with the theoretical predictions within $\pm\tau_c/2$. Implications of this result for communication and navigation applications is discussed in section 3.5.

The locations of the maxima and the minima are calculated as

$$d_n = \sqrt{\frac{16h_1^2h_2^2}{n^2c^2\Delta^2} + \frac{n^2c^2\Delta^2}{16} - (h_1^2 + h_2^2)} \quad (3.34)$$

where c is the speed of light and $\Delta = \tau_c/2$.

The propagation of a UWB pulse in the presence of a single infinite/finite thickness wall is highly idealized. Several UWB applications are targeting short range (< 5 m) cluttered propagation environments inside buildings. Hence, measurements and numerical simulations of UWB pulse propagation in a hallway and a room are presented in the next section.

3.3 UWB Pulse Propagation inside a Building

The band-limited impulse response of a hallway and a room is measured using a vector network analyzer. Three specific transmitter-receiver configurations are chosen representative of the propagation scenarios commonly encountered inside buildings. The FDTD code, discussed in Chapter 2, is used to calculate the channel impulse response and is compared with measurements.

3.3.1 Measurements

The top panel of Figure 3.14 shows the schematic of the ultra wideband wave propagation experiments done inside a hallway and a room in the Duckering building at UAF on 26 June 2006. A pair of oval dipole antennas, discussed in Chapter 2, are connected to the two ports

of a vector network analyzer (VNA). The VNA measures the scattering parameters in 1601 equally spaced points between 300 kHz to 9 GHz. The transmitting oval dipole antenna is connected to port 1 of the VNA and placed in the center of the Duckering hallway. The local coordinate system chosen was: the z -axis along the local vertical upward from the floor, the x -axis along the length of the hallway and the y -axis along the breadth of the hallway in the cross product direction of the z -axis and the x -axis. The origin of the coordinate system is at the transmitting antenna location. Three receiver locations are chosen: (1) non-line-of-sight propagation (NLOS) in the hallway with a corner obscuring the direct LOS between the transmitter and receiver (Point A); (2) line-of-sight (LOS) propagation between the transmitter and the receiver separated by 14 feet (Point B); (3) NLOS through-the-wall propagation from the hallway to a laboratory classroom. For all three cases the transmitting and receiving antenna are held on a tripod 1.37 m above the ground.

The overall transfer function of the transmitting antenna-propagation channel-receiving antenna system is $H(\omega)$ which is related to the forward transmission coefficient measured by the VNA as

$$H_t(\omega)H_{ch}(\omega)H_r(\omega) = S_{21}(\omega)/2 \quad (3.35)$$

where $H_t(\omega)$ is the transmitting antenna transfer function, $H_r(\omega)$ is the receiving antenna transfer function, and $H_{ch}(\omega)$ is the propagation channel transfer function. $\omega = 2\pi f$ is the radian frequency. The antenna transfer functions are measured in the anechoic chamber when the two antennas are held fixed along the local vertical with their broadside directions facing one another, as discussed in Chapter 2. The antenna response is assumed to be constant over a wide range of transmission and reception angles so that the receiving pulse amplitude at different angles of arrival may be weighted by the radiation pattern of the antenna but not distorted.

The band-limited impulse response of the channel $h_{ch}(t)$ is calculated after zero padding the channel transfer function from 9 GHz to 200 GHz which provides an interpolated time

resolution of 5 ps.

$$h_{ch}(t) = \frac{1}{2\pi} \int \frac{S_{21}(\omega)e^{-j2\pi ft}}{2H_t(\omega)H_r(\omega)} df \quad (3.36)$$

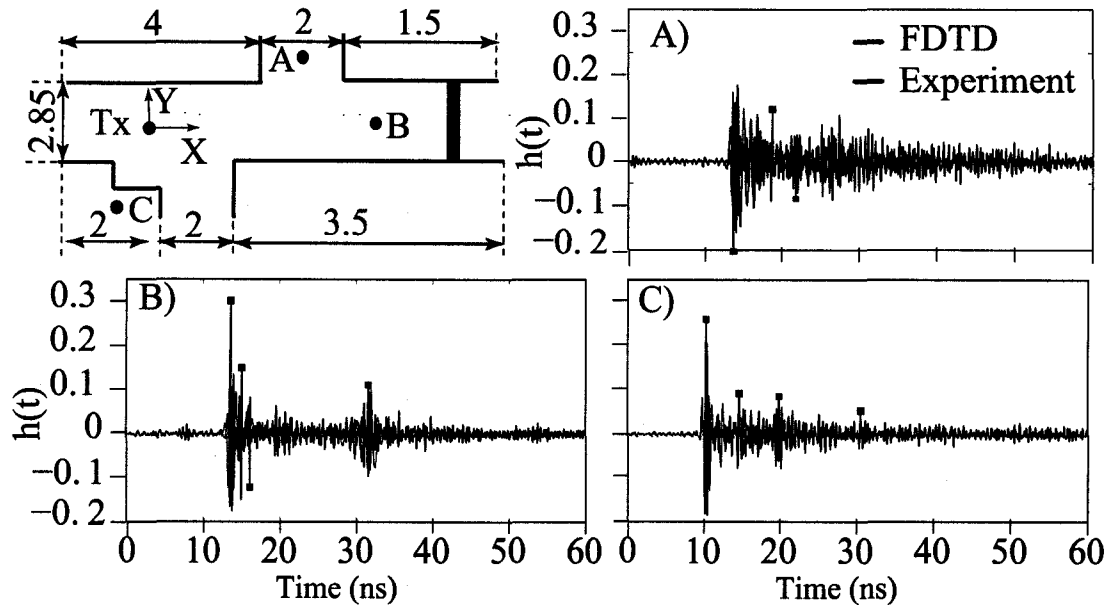


Figure 3.14. Measurement and simulation of UWB pulse propagation inside a hallway in the Duckering building at UAF. The top panel shows the geometry of the hallway. All the dimensions are in meters. The bottom panel shows the comparison of the measured (black curve) and the simulated (red curve) band-limited impulse response for the NLOS corner (left plot), LOS in hallway (middle plot) and NLOS through-the-wall propagation (right plot). The black dots show the peak amplitude of the multiple propagation paths for each of the propagation scenarios A, B and C, respectively.

The three plots in the bottom panel of Figure 3.14 show, as a black curve, the band-limited impulse response for the three receiver locations A, B and C. The impulse response clearly shows multiple pulses delayed in time and scaled in amplitude by the free space spreading loss and the reflection coefficient of the walls of the hallway. The ground of the hallway is 10 cm thick concrete ($\epsilon_r = 4.44$, $\sigma = 0.001$ S/m) and the side walls 6 cm thick are sheetrock ($\epsilon_r = 2.2$, $\sigma = 0.002$ S/m) [Bertoni, 2000]. The hallway roof is a false ceiling that covers several metal pipes and wires and is assumed to be a perfect reflector. The

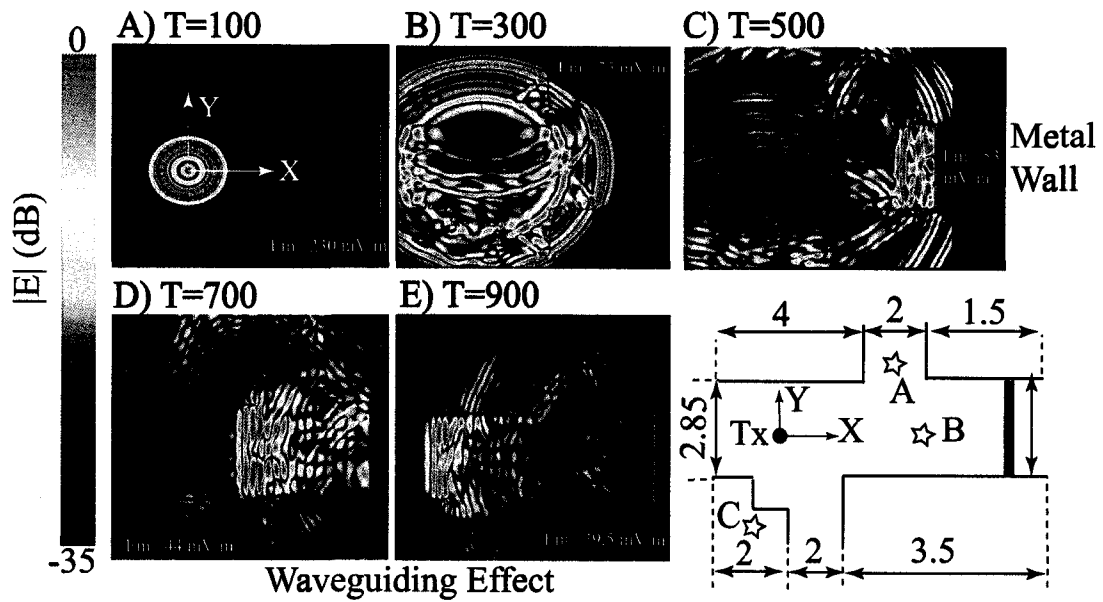


Figure 3.15. Time snapshots of the FDTD calculation of the UWB peak electric field amplitude along the length of the hallway, across the corner, and inside the laboratory room. The simulation geometry is shown in the bottom right panel. All the dimensions are in meters.

hallway is 2.85 m high by 30 m long by 2.8 m wide.

For the LOS case B (middle plot in bottom panel of Figure 3.14), using the formulae for direct and reflected path lengths discussed in the previous section, (1) the time of arrival of the first arriving direct path pulse is 14.4 ns, (2) the time of arrival of the reflection from the concrete ground is 16.9 ns, (3) the time of arrival of the reflection from the metal ceiling is 17.3 ns, (4) the time of arrival of the reflection from either side wall is 17.11 ns, and (5) the time of arrival of a perfect reflection from a 20 cm thick metal door, 3.7 ft behind the receiver at location B, is 21.9 ns. The measured impulse response shows the strongest peak at 14.4 ns. The impulse is fairly broadened from $14.4 + 3$ ns, owing to the first order bounces from the roof, ceiling and side walls overlapping with the direct path. The reflection from the metal door is seen at 21.91 ns. Similarly in the measured impulse response of the NLOS cases A and C, the distinct dominant paths can be separated out to point out the contributing reflecting surfaces. The envelope of the impulse responses in all three cases show a clustering of multiple path pulse and an exponential decay of their amplitudes. This feature closely follows the modified Saleh-Valenzuela double exponential model for UWB propagation discussed in [Molisch, 2005 and references therein].

3.3.2 FDTD Simulations

The problem geometry shown in the bottom right panel of Figure 3.15 is simulated using the parallel FDTD code developed at UAF and discussed in Chapter 2. The spatial domain of the simulation was $750 \times 800 \times 280$ mesh points with a spatial resolution of 1 cm corresponding to a maximum frequency of 3 GHz. The time resolution calculated by Courant condition is 1.89 ps. The excitation voltage waveform is a Gaussian waveform with a pulse width of 1 ns.

The red curve in the bottom panel of Figure 3.14 shows the calculated time domain impulse response. For all the three scenarios, the time of arrival of the strongest pulse, calculated using FDTD, shows excellent agreement ($< 1\%$) with the measured data. The FDTD simulation predicts only the first few multiple propagation paths (~ 5 or 6 peaks)

observed in the measured data. This is because of a lack of spatial and temporal resolution in the FDTD code. The FDTD code would require a spatial resolution of 3 mm to cover the entire VNA frequency range from 300 kHz to 9 GHz. The memory available for the simulations permitted a minimum spatial resolution of 1 cm which covered a frequency range from DC to 3 GHz. The memory required for this simulation was ~ 8 GB.

Figures 3.15 A-E show the snapshots in time of the electric field amplitude in the simulated hallway and room geometry shown in the top panel of Figure 3.14A. The electric field amplitude maps clearly show the wave guiding effect of the hallway and the effect of the metal wall behind the receiver at location B. The metal wall re-radiates the incident electromagnetic energy, thereby causing a strong signal to propagate along the hallway with its strength falling off slower than in free space as seen by the peak electric field amplitudes in time steps C, D, and E.

3.4 Summary of Results

The following results were presented in this chapter: (1) time domain measurements on ultra-wideband (UWB) pulse propagation over the ground show the presence of three distinct propagation regimes separated by two characteristic distance scales d_1 and d_2 , called the first and the second breakpoint distances, which depend both on the geometrical parameters such as the heights of the transmitter (h_1) and the receiver (h_2) over the ground as well as on UWB pulse properties such as pulse duration (τ_p) and cycle time (τ_c). For a given transmitter height h_1 , the loci of first and second breakpoints in the (d, h_2) plane are hyperbolas with the transmitter and its image as the foci; (2) frequency domain measurements and FDTD simulations of UWB pulse propagation inside a hallway and a room show excellent agreement for the time of arrival and the amplitude of the first three dominant paths.

3.5 Discussion

Given a pulse with certain τ_p and τ_c , the propagation regimes can be determined. As discussed below, the propagation regimes have important implications for various applications of UWB technology.

3.5.1 Range of Propagation Regimes Consistent with FCC Regulation

Because the UWB band is controlled by FCC, it is important to determine the limits on the sizes of three propagation regimes consistent with FCC regulation Part 15, IEEE 802.15B. According to the FCC regulation, the minimum bandwidth is 500 MHz, corresponding to $\tau_p = 2$ ns and the maximum bandwidth is 7.5 GHz, corresponding to 130 ps. Assuming the transmitter and receiver heights $h_1 = h_2 = 1$ m, the size of the first regime ($d_1 \sim 4h_1h_2B/c$) ranges between ~ 6.7 m and ~ 100 m. The size of the regime scales linearly with both h_1 and h_2 . The minimum and maximum values of f_c are 3.35 Hz (assuming $B=500$ MHz) and 10.35 GHz (assuming $B=500$ MHz). These correspond to the third regime ($d_2 \sim 4h_1h_2f_c/c$) ranges of 44.7 and 138 m. Again the distance at which the third regime starts scales linearly with h_1 and h_2 . When $d_1 < d_2$, the second regime size is simply $d_2 - d_1$. In the extreme case when $B \sim f_c$, we have $d_1 \sim d_2$ and second regime disappears. Figure 3.16A shows the dependence of d_1 and d_2 given B and f_c and 3.16B shows the dependence of f_c and B on d_1 and d_2 . These figures may be useful in the design of UWB pulse properties in a given situation.

3.5.2 Effect of Finite Thickness Walls on UWB Receiver Performance

Finite thickness reflecting surfaces or layered reflecting surfaces cause the incident signal to bounce back and forth inside the wall surface thereby resulting in echoes or an elongated reflected signal depending on the time duration of the incident signal. The UWB received voltage measurements, in Figure 3.10A and 3.10B, showed an elongation of the duration of the pulse. To further quantify the relation between the width and the electrical properties of the reflecting surface and the time duration of the received voltage waveform, ray tracing

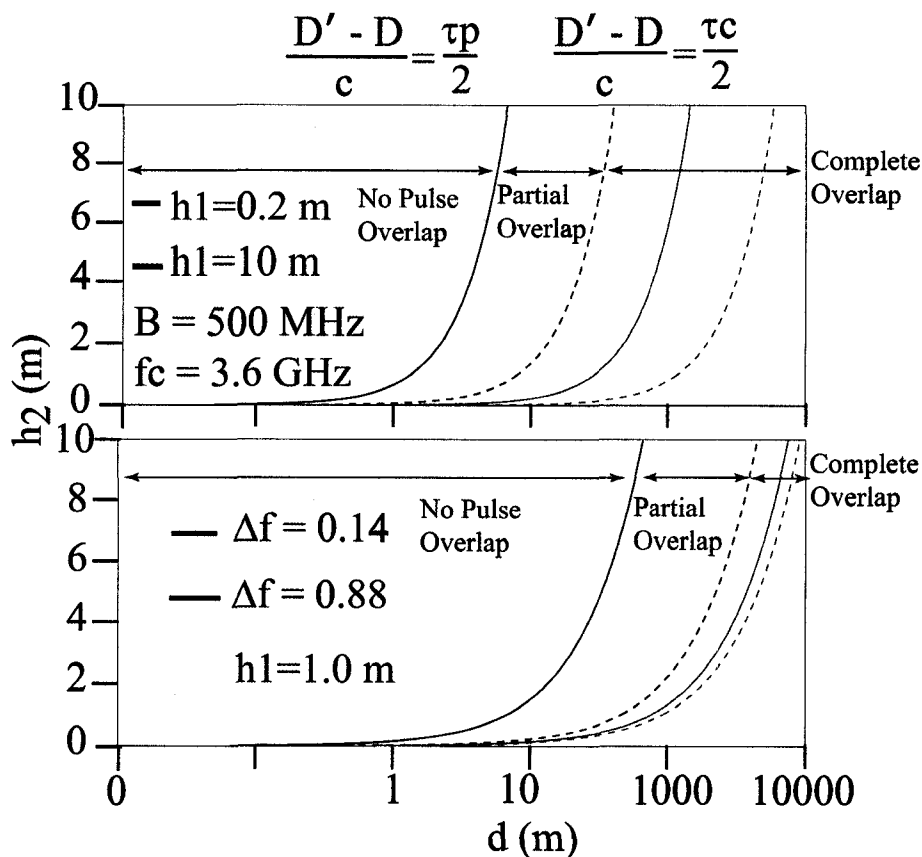


Figure 3.16. Calculation of the three propagation regimes for varying pulse and geometrical parameters. The solid lines show the transition between the first regime (no overlap) and the second regime (partial overlap). The dotted lines show the transition between the second regime and the third regime (complete overlap). The receiver height h_2 is varied from 0.2 - 10 m. In the top panel, the two transmitter heights chosen are $h_1 = 0.2$ m and $h_1 = 10$ m respectively. The transmitted pulse has a transmission bandwidth $B = 500$ MHz and $f_c = 3.6$ GHz. In the bottom panel, the transmitter $h_1 = 1.0$ m and the fractional bandwidth of the transmitted pulse is chosen as 0.14 and 0.88 respectively. The bandwidth for the two cases is 500 MHz and 6 GHz respectively and the center frequency for the two cases is $f_c = 3.6$ GHz and $f_c = 6.85$ GHz respectively.

calculations were done for a 30 cm thick concrete wall ($\epsilon = 4.44$, $\sigma = 0.001$ S/m [Bertoni, 2000]). The problem geometry is shown in Figure 3.17A. A 1 ns long sinc pulse (Figure 3.17B) is radiated and received by a pair of isotropic antennas separated by a distance of 10 m. Figure 3.17C shows the direct path voltage at the terminals of the receiving antenna. Figure 3.17D shows the reflected path voltage for the transverse electric (TE) and the transverse magnetic (TM) polarization. Figure 3.17E shows the amplitude of the direct and the reflected electric field pulse for TE and TM polarization respectively in one figure to show the relative magnitude and placement in time of these two parts of the received signal. Note that the polarization of the direct and reflected pulse is different.

From these calculations it is observed that the width of the wall plays a significant part in determining not only the parameters of the reflected UWB pulse but also the pulse shape unlike narrow band pulses ($> 1 \mu\text{s}$) whose pulse shape remains unaltered. Therefore, the idea of using a correlation receiver might not work very well when the wall widths cause pulse propagation time inside the wall to be larger than the pulse duration. The pulse undergoes shape distortion as it reflects off the wall owing to interference between waves reflected of the front and back face of the wall. This would increase the multipath interference and is crucial in deciding the width of the UWB pulse. The shape distortion of the pulse places a question mark on the efficiency of pulse shape based modulation techniques [Ghavammi *et al.*, 2007] especially in cluttered indoor environments. Our calculations also show delayed pulses coming from the back face of the wall. This could cause errors in the demodulation at the receiver for modulation schemes based on pulse position [Scholtz, 1993].

3.5.3 Extension of the Theoretical Model to LOS and NLOS Scenarios With More Than Two Propagation Paths

The theoretical model can easily be extended to multiple propagation paths involving one direct path and several reflected paths. Consider a two reflecting surface case, which may result from one finite thickness wall considered earlier or two semi-infinite surfaces, such as the space between a parallel plate waveguide (top panel of Figure 3.14). In this case,

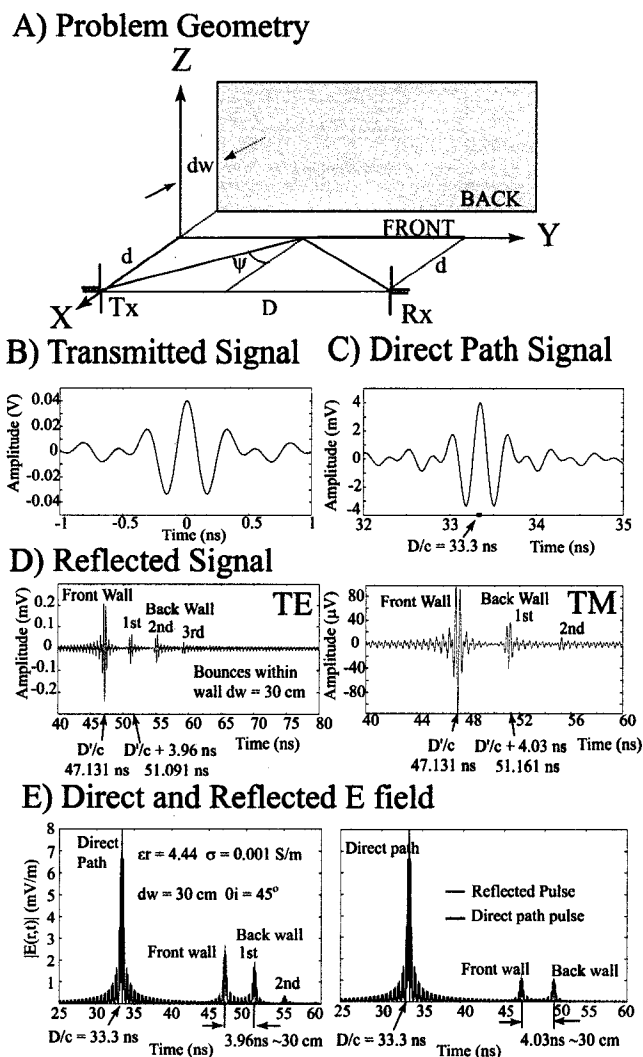


Figure 3.17. Ray tracing simulation of UWB pulse propagation in the presence of a 30 cm concrete wall. A) Problem geometry. B) Transmitted pulse. C) Contributions of the direct pulse to the received signal. D) Contributions of the reflected pulse with transverse electric (TE) and transverse magnetic (TM) polarization to the received signal. E) relative magnitude and placement in time of the direct and reflected pulse in one figure for TE and TM polarization respectively. Note that the polarization of the direct and reflected pulse is different. Clearly multiple reflections within the wall alter the amplitude and phase of each Fourier component of the transmitted uwb pulse causing a change in pulse shape in the frequency domain and a pulse spreading in time domain.

consider a direct source and two image sources contributing to three principal paths and many other paths resulting from multiple reflections between the two walls. To a first approximation, this case can be treated as follows: calculate the breakpoints for each of the walls separately. Then, a first propagation regime of direct path only, followed by a second regime of overlap which will contain the first overlap of two UWB pulses and then for that of three. The second regime will continue until the second breakpoint (lower value of the two) when the direct and the reflected path will cancel out, but the third path will continue to contribute to RSS as $1/d^2$. At large enough d ($d \gg h_1, h_2$) all paths will contribute equally and we will get a sum of N $1/d^2$ kind of terms adding in or out of phase, giving a power fall off larger than $1/d^2$. This is essentially the waveguide effect in which multiple paths contribute to the power in random phase. With a larger number of reflecting surfaces, we can envision a similar result: a region of no overlap, followed by a region of overlap in which direct path adds up constructively or destructively giving max. and min., followed by a region in which the direct path cancels out with the first arriving reflected path and other propagation paths add up in random phases leading to waveguide type of behavior. There is still three propagation regimes separated by the first and the second breakpoints estimated using the smallest of h_1 values. The character of the first and the second regime is qualitatively the same as that of the single wall case in the sense that the first regime is a "free space regime," the second regime will consist of maxima and minima separated roughly by the same distance as the single reflecting wall. The third regime will be more complicated with rapid maxima and minima as the number of paths overlapping increases and the eventual falls off as in the case of a waveguide. This completes the discussion of UWB pulse propagation inside a room or a hallway with one line of sight path.

Now consider the NLOS case with no direct path between the transmitter and the receiver. Each of the multiple propagation paths reaching the receiver will contribute a pulse with the same τ_c but with different τ_p , amplitude and envelope depending on the thickness and the dielectric constant of the reflecting surface. There will be a shortest path, which may give us a first regime. It should be noted that the signal strength in this regime

may fall off differently from free space $1/d^2$ fall off and will depend on the nature of the propagation of the first arriving pulse. Then there will be a second regime which will start at the first break point. Assuming the shortest NLOS pulse has a shape with a central maximum and a pulse width $\tau_{p1} > \tau_p$, a larger first regime is expected (see Figure 3.16). The third regime after the second break point will remain the same as the LOS case because τ_c remains the same. Note that the line joining the transmitter and receiver need not be normal to the wall. Each pulse arriving at the receiver has an amplitude, A_n , pulse width, τ_{pn} and cycle time, τ_{cn} . Each pulse arrives with a certain delay τ_{gn} . We have the same situation as discussed above for the waveguide case. Again three regimes are expected: a first regime where the RSS falls off as the peak amplitude of the first arriving pulse, a second regime where maxima and minima are observed in the RSS due to overlap between the first and the second arriving pulses, and a third regime in which the first and the second arriving pulses cancel out and the other multipath pulses add incoherently.

3.6 Concluding Remarks

The dependence of multipath propagation effects on UWB pulse characteristics has profound implications for the use of UWB technology in communication and navigation. The results presented in this chapter suggest a new method of secure communication. To illustrate this method, two hypothetical examples, one involving secure communication between two parties (e.g., two soldiers) and one involving secure communication among multiple sensors (e.g., a network of sensors gathering intelligence) is discussed. Consider transmission between two parties, Alice and Bob. We can imagine both of them to be located at maximum signal locations. The reciprocity discussed above makes this possible. Now both Alice and Bob can vary their transmitted pulse properties (f_c , B) in any preconceived manner such that they remain located on one maximum or the other. An enemy, Eve (eavesdropper), located at a different location will observe a signal that fades in and out. A further level of security can be obtained by using two orthogonal antennas and transmitting on one or the other in a prescribed manner. When dealing with a sensor network communicating with

a base station, it can be envisioned that sensors will be located on the maximum signal strength locations. Here again the f_c and B can be varied in a prescribed manner. Of course, in this case, it is clear that there may be certain restrictions on how f_c and B can be varied because it would be favorable that all the sensors lie on maximum signal amplitude locations all the time.

The work presented here indicates that the propagation channel and the antennas place a bound on the minimum achievable bit error rate of an UWB communication system. This is the topic of the next chapter where a modular simulation approach is developed in MATLAB to calculate the bit error rate of two UWB receiver models taking into account the antenna and the propagation channel measurements presented in Chapter 2 and this chapter.

Chapter 4 Numerical Model of a UWB Matched Filter Receiver and a Rake Receiver

4.1 Objective and Significance

The objective of this chapter is to develop a MATLAB-based numerical model of a time hopping pulse position modulated (TH-PPM) UWB communication system with two commonly used UWB receivers namely the matched filter and the rake receiver. The experimental results of the antennas and the propagation channel from chapters two and three are incorporated in the numerical model to calculate the bit error rate of the two receiver models for specific antenna and propagation channel configurations. The effect of thermal noise and multi user interference are also included in the calculations.

A lot of research has been done on the performance of TH-PPM based UWB communication systems [Durisi *et al.*, 2003; Win and Scholtz, 2000]. Past antenna [Schantz, 2005] and propagation [Molisch, 2005] work as well as work in chapters two and three clearly suggest that the antenna and the propagation channel place a stringent bound on the performance of a UWB system. Most numerical and analytical calculations of bit error rate of a UWB communication system assume omnidirectional antennas and a statistical propaga-

tion model [Dibenedetto and Giancola, 2004]. This omits a separate thorough evaluation of the pulse distortion caused by the antenna and the propagation channel on the UWB receiver performance. Most available channel measurements do not separate the antenna effects from the effects of the propagation channel [Cramer *et al.*, 2002]. Recently, Sibelle *et al.* [2005] have provided a simulation framework to calculate the bit error rate of UWB receivers for measured UWB antenna response. Wang *et al.* [2005] calculated the bit error rate of a UWB communication system for a pair of thin wire dipoles and square loops simulated using finite difference time domain calculations. Their results showed that high gain and well matched antenna pairs reduce the bit error rate of a UWB communication system. Zhang and Brown [2006] have computed the bit error rate of a binary phase shift modulated UWB system with simulated time domain response of a discone antenna and a ray tracing propagation model. Their results showed that pulse dispersion of the antenna in directions other than its main beam direction dominated the bit error rate of the UWB communication link. The work presented in this chapter has several unique features compared to the past work: (1) it computes the bit error rate of two UWB receivers for the measured transmitting and receiving antenna response for two specific UWB antennas: an omnidirectional oval dipole and a directional horn antenna; (2) it computes bit error rate as a function of the measured radiation pattern of an oval dipole antenna; (3) it calculates bit error rate for line-of-sight and non-line-of-sight propagation channel measurements inside a hallway.

The first section of the chapter discusses the objective and the significance of the receiver simulation work presented in light of work done in the past. The second section describes the MATLAB-based UWB system model developed. The third section presents case studies to quantify the effects of individual system parameters such as noise, antenna, multipath and multi-user interference on bit error rate of the two UWB receivers simulated. The fourth section summarizes the results presented in this chapter. The fifth section discusses the implications of the results presented for communication, navigation and radar applications and the sixth section presents concluding remarks.

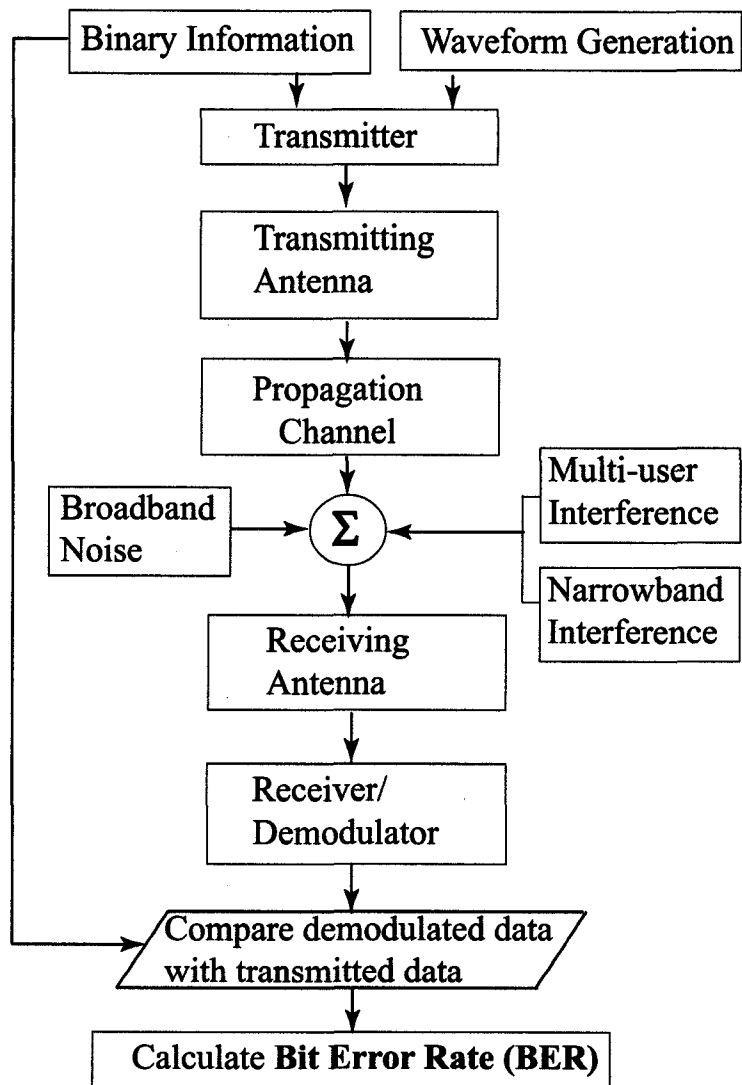


Figure 4.1. Block diagram of the numerical model of an UWB communication link from signal generation to information retrieval.

4.2 Simulation Model of a UWB Communication System

Figure 4.1 shows the block diagram of the end-to-end UWB communication system model. The transmitter model encodes the binary information that needs to be transmitted on a sequence of UWB pulses generated by the waveform generation model. The information is modulated by altering the pulse-to-pulse interval and applied to the transmitting antenna. The transmitting antenna model transforms the input pulse sequence into the frequency domain, and computes the complex spectrum of the radiated electric field at the receiving antenna location, in the far field of the transmitting antenna, via FDTD calculations or measured band-limited impulse response. The radiated vector electric field is a function of both the signal from the signal generator and the characteristics of the antenna. The propagation model calculates the multiple propagation paths by which the radiated electric field waveform reaches the receiving antenna location from the transmitting antenna location using either finite difference time domain calculations or frequency domain measurements. This model assumes that the transmitting and the receiving antenna are isotropic in nature. Thermal noise and undesired interference signals may be added to the received UWB signal transformed back into the time domain. Thermal noise is modeled as additive white Gaussian noise (AWGN) and the interfering signal may include a single frequency sinusoidal signal or an UWB signal with a different pseudo-random sequence of pulses. The receiving antenna model converts the incident electric field vector into a voltage signal at the antenna terminals, via FDTD calculations or measured band-limited impulse response. The received voltage signal is input to the UWB receiver model, where it is processed to extract the binary information that was encoded onto the UWB signal by the signal generation model. The extracted binary information is compared with the original transmitted information to calculate the bit error rate (BER) of the UWB communication link.

4.2.1 Waveform Generation Model

Figure 4.2 shows the UWB waveform generation model. The UWB waveform can be defined by either an equation or a data file. UWB waveforms can generally be grouped into two

categories: (1) Baseband impulses that have ultra-short pulse widths $\tau < 1$ ns with correspondingly ultra-wide spectra (> 1 GHz), (2) Pulse modulated RF sine waves, in which the pulse width is typically only a few cycles of the RF center frequency. Figure 4.3 shows examples of the normalized UWB pulses and their spectra generated by the waveform generation model.

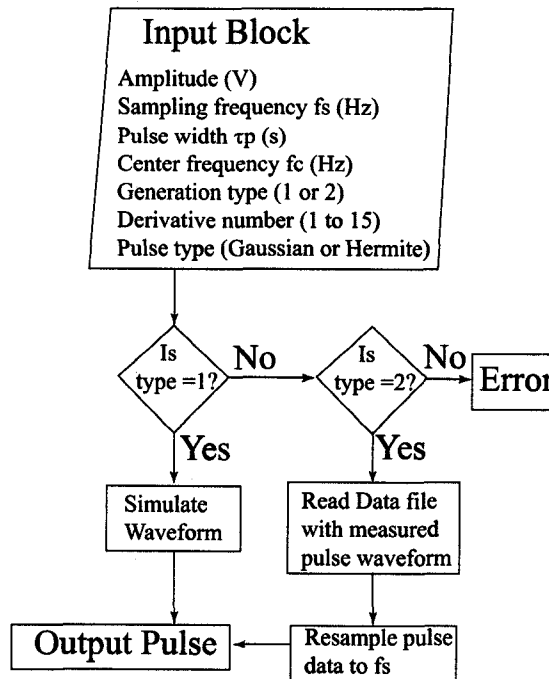


Figure 4.2. Block diagram of the UWB waveform generation model.

4.2.2 Transmitter Model

Figure 4.4 shows the block diagram of the transmitter model. The input UWB waveform is generated by the waveform generation model. The position of the pulses in the time domain waveform is altered based on: (1) Orthogonal Pseudo-random Noise (PN) sequence for spectral shaping and/or code division multiple access (CDMA). For multi-user applications, the pulse delay is dithered in time by a unique PN code $C(i)$ for each user. A PN code generator is used based on the number of frames and number of slots in each frame. The

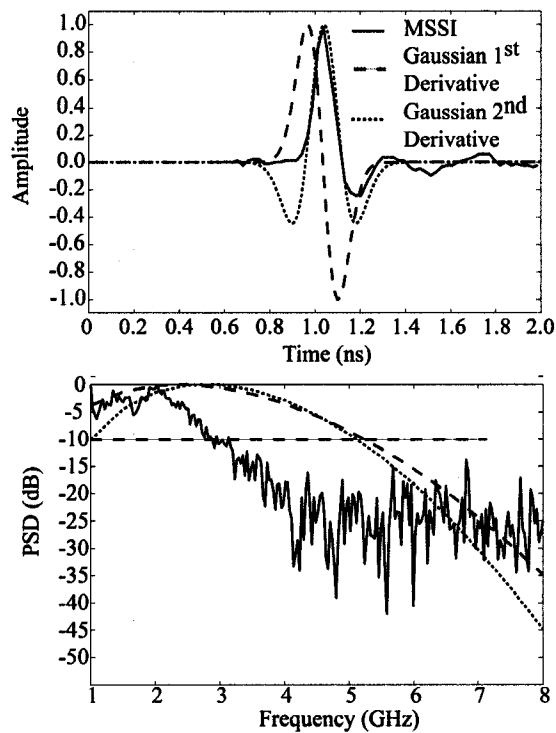


Figure 4.3. Normalized waveforms and spectra for the measured MSSSI pulse (solid line) and the simulated first and second derivatives of the gaussian pulse (dotted lines) with a pulse width of 0.6 ns. The MSSSI pulse has a pulse width of 0.7 ns.

frame number is determined by pulse repetition rate. For example, if there are M pulses used to represent one bit information, the frame number equals to M . The number of slot in each frame is determined by number of users. For example, if each frame contains N slots, the maximum number of users in the system is 2^N . (2) Pulse Position Modulation (PPM) by a equiprobable binary sequence [0 or 1] generated by the `rand()` function in MATLAB. The PPM modulation scheme adds an additional time shift of δ to '1' bits, but no additional time shift to '0' bits. The m-files used in this model are listed in Appendix C.

Figure 4.5 shows an example of a sequence of pulses generated by the transmitter block with and without PN code generation. The top left panel shows a sequence of pulses uniformly spaced every 10 ns and the bottom left panel shows the sequence of pulses shifted in time by a PN code. The top right panel shows that uniform spacing of pulses causes sharp spectral peaks spaced every 100 MHz apart. These peaks cause unwanted interference with coexisting narrow band systems at specific frequencies inside the UWB bandwidth. The bottom right panel shows that the peaks can be removed by dithering the pulse sequence which randomly alters the phases of the frequency domain components thereby “whitening” or flattening out the spectrum of the signal. The overall envelope of the signal spectrum follows the spectrum of the individual waveform.

4.2.3 Transmitting Antenna and the Propagation Channel Model

The time domain voltage signal for user 1, $s_t^1(t)$, generated by the transmitter model, is applied to the transmitting antenna model shown in Figure 4.6. The transmitting antenna impulse response $h_t(\theta_t, \phi_t, t)$ is either calculated using FDTD or measured as described in Chapter 2. The antenna impulse response is Fourier transformed to get the antenna transfer function in the frequency domain, $H_t(\omega, \theta_t, \phi_t)$, which is multiplied with the spectrum of the UWB signal generated at the transmitter output, $S_t^1(\omega)$ and inverse transformed to obtain the complex radiated electric field waveform, $E_{rad}(\theta_t, \phi_t, t)$ in the far field of the

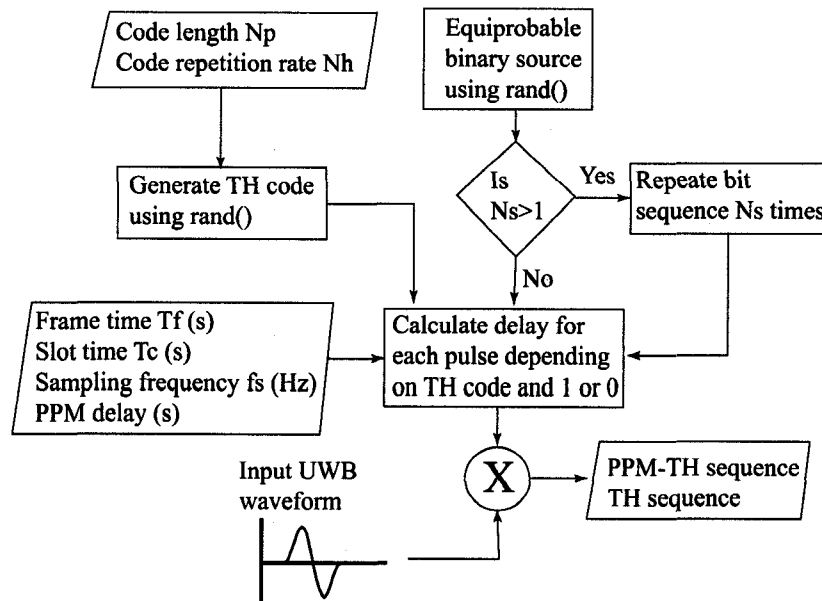


Figure 4.4. Block diagram of the UWB transmitter model.

transmitting antenna given as

$$E_{rad}(\theta_t, \phi_t, t, \hat{p}) = IFFT(H_t(\omega, \theta_t, \phi_t, \hat{p})S_t^1(\omega)) \quad (4.1)$$

where \hat{p} is the polarization vector. The orientation of the electric field vector in the far-field defines the polarization of the radiated signal for each transmission angle. Hence there are two separate band-limited impulse responses for each transmission angle (θ_t, ϕ_t) to fully represent the most general antenna behavior with arbitrary polarization characteristics. In this chapter, only the vertically polarized components will be considered though horizontally polarized components are also available (discussed in Chapter 2) and will follow the exact same procedure detailed here.

Figures 4.7 shows the block diagram for the the propagation channel model. The transient response of the propagation channel can be either measured or simulated (using FDTD) to calculate the radiated electric field waveform at the receiving antenna location $E_{rec}(\theta_t, \phi_t, t, R, \hat{p})$ given as

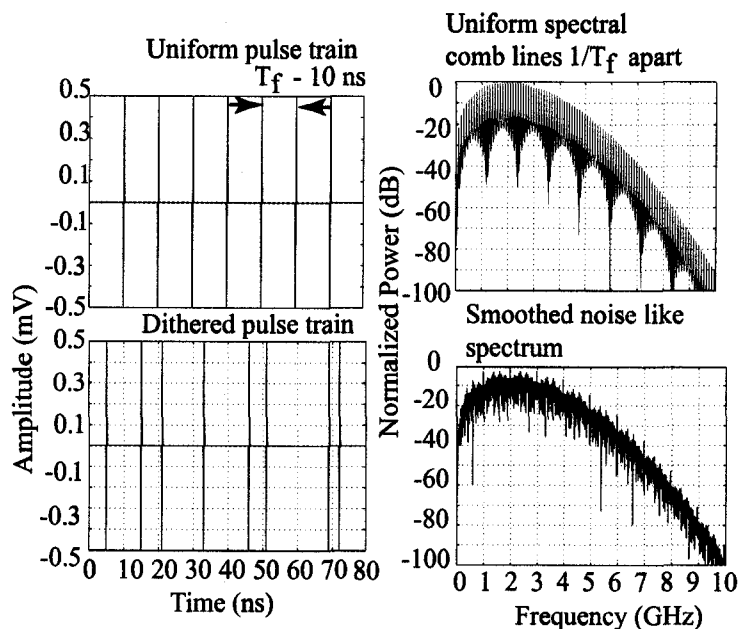


Figure 4.5. Example of a dithered and un-dithered pulse train generated by the transmitter model. The inputs to the model are $Pow = -30$ dBm, $f_s = 50$ GHz, $T_f = 3$ ns, $N_s = 5$, $T_c = 1$ ns, $N_h = 3$, $N_p = 5$, $T_m = 0.5$ ns, $dPPM = 0.5$ ns, bits [1 0] and time hopping (TH) code [1 0 1 0 2].

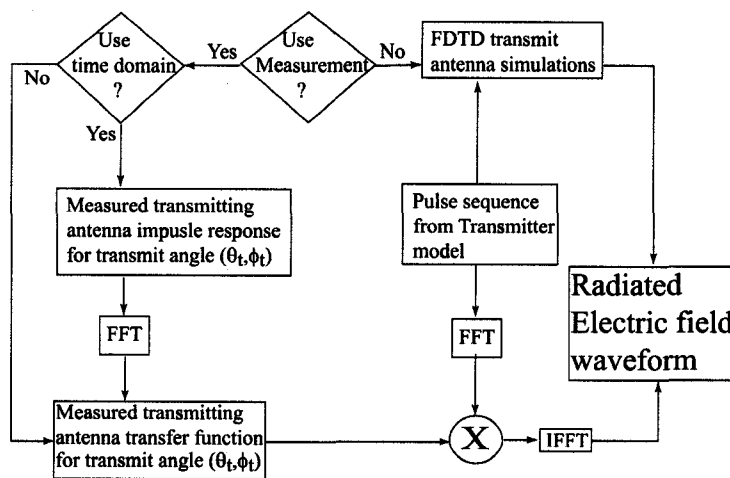


Figure 4.6. Block diagram for transmitting antenna model.

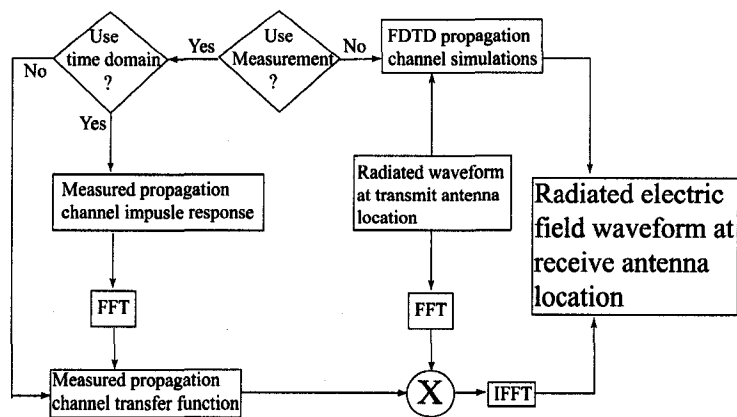


Figure 4.7. Block diagram for propagation channel model.

$$E_{rec}(\theta_t, \phi_t, t, R, \hat{p}) = IFFT(FFT(E_{rad}(\theta_t, \phi_t, t, \hat{p}))H_{ch}(\omega, R)) \quad (4.2)$$

where R is the separation distance in meters between the transmitter and the receiver.

4.2.4 Noise and Interference Model

Background noise and signals from other undesired source may be added to the radiated electric field waveform at the receiving antenna location to evaluate the system performance in the presence of noise and interference. The background noise is modeled as a zero mean Gaussian noise with variance $N_0/2$ where N_0 is the average noise spectral density. The background noise is added either as the ratio of the energy in one bit to the noise spectral density E_b/N_0 or the energy in one pulse to the noise spectral density E_p/N_0 as follows

$$\begin{aligned} E_p &= (1/N_p) \int |s_t^1(t)|^2 dt \\ N_0 &= E_p/10^{\frac{E_p/N_0}{10}} \\ \sigma &= \sqrt{N_0/2} \end{aligned} \quad (4.3)$$

where E_p is the energy per pulse, N_0 is the noise spectral density and σ is the noise standard deviation. Or

$$\begin{aligned} E_b &= (1/N_b) \int |s_t^1(t)|^2 dt \\ N_0 &= E_b/10^{\frac{E_b/N_0}{10}} \\ \sigma &= \sqrt{N_0/2} \end{aligned} \quad (4.4)$$

where E_b is the energy per bit. One bit can be spread over multiple pulses to improve the spreading gain of the system. If one bit is spread over N_s pulses then $E_b = N_s E_p$. So for the same dB value, E_p/N_0 introduces more noise than E_b/N_0 . For the rest of the simulation E_b/N_0 is used.

Past work has shown that UWB has multiple sources of interference from coexisting narrowband systems [Kissick, 2001]. Of particular importance is the potential interference of GPS and navigational bands, and cellular phone bands with UWB [FCC, 2002]. There is considerable work done in the study of degradation in UWB system performance due to single frequency and multiple frequency interfering signals [Choi and Stark, 2002 and references therein]. If the frequency of the interfering signal is known several techniques are proposed to avoid the interference to the UWB signal [Taha and Chugg, 2002; Wang *et al.*, 2003]. Interference could also occur due to multiple UWB sources transmitting at the same time and in the same frequency range as the information signal thereby polluting the received pulse sequence [Reed, 2005 and references there in].

In our simulations, the undesired interference signal is modeled as a single frequency (tone) signal or an UWB signal with a different PN sequence than the desired UWB source signal to evaluate multi-user performance using Code Division Multiple Access (CDMA). The additional UWB sources have the same average transmit power as the desired signal.

4.2.5 Receiving Antenna Model

Figure 4.8 shows the block diagram of the receiving antenna model. The band-limited impulse response, $h_r(\theta_r, \phi_r, t)$ of the receiving antenna is either calculated via FDTD or measured as discussed in Chapter 2. The impulse response is dependant on the angle of arrival of the transmitted signal (θ_r, ϕ_r) , and the polarization of the signal relative to the receiving antenna. It is important to note that the current simulation model does not include separate impulse responses for each receive angle (θ_t, ϕ_t) and only accounts for the receiver held along the local vertical with its broadside direction facing the transmitting antenna.

Figure 4.9 shows a single frame of the generated pulse sequence $s(t)$ (black dashed curve), the received pulse sequence in the anechoic chamber (black dotted curve), and the received pulse sequence in a line-of-sight (LOS) hallway. The parameters for the generated pulse sequence shown are: average transmission power $P_t = 0$ dBm; pulse width $\tau_p = 1$ ns; and data rate $R_b = 100$ Mbps. The received pulse sequence is derived as described earlier by convolving the generated sequence with the band-limited impulse response of the transmitting and receiving commercial horn antennas, and the band-limited impulse response of the LOS hallway shown in case B of Figure 3.14. For the anechoic chamber scenario the pulses propagate in free space and so the propagation channel resembles an all pass filter. Additional zero crossings are introduced in the received voltage waveform by the transmitting and receiving horn antenna pair. There is no noise or interference added to the signal at the input to the receiving antenna model. This is done to isolate the effects of the antenna and the propagation channel on the generated UWB waveform. Note also that the received voltage waveform after multipath propagation spills over to the next time frame and alters the transmitted signal in the next frame. This indicates that multipath places a maximum bound on the achievable data rate of an UWB communication system for a given set of transmitted UWB pulse properties.

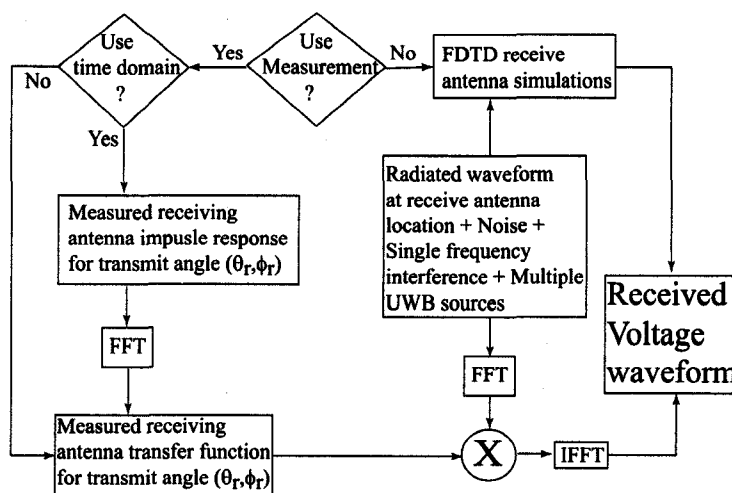


Figure 4.8. Block diagram for the receiving antenna model.

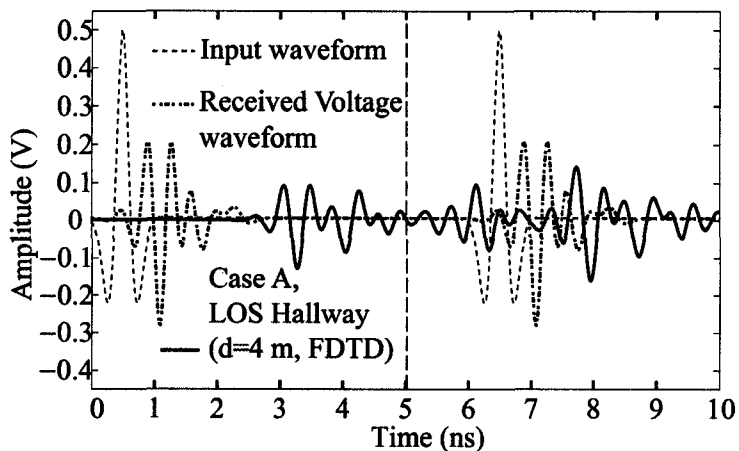


Figure 4.9. Example of the received voltage waveform for a pair of horn antenna 4 m apart in a line of sight hallway. The broadside received voltage waveform for a pair of horn antennas separated by a distance of 2 m in the anechoic chamber is measured using a DSO as discussed in chapter 2. The propagation channel impulse response is calculated from the FDTD simulations for the case B discussed in Figure 3.14 of chapter 3 and convolved with the received voltage waveform.

4.2.6 Receiver Model

Two commonly used receiver models are discussed in this section: (1) matched filter receiver and (2) rake receiver. The rake receiver with a single correlation path or finger is identical to the matched filter receiver. The effect of antenna and propagation channel on the bit error rate performance of these receivers is calculated using these models.

4.2.6.1 Matched Filter Receiver Model

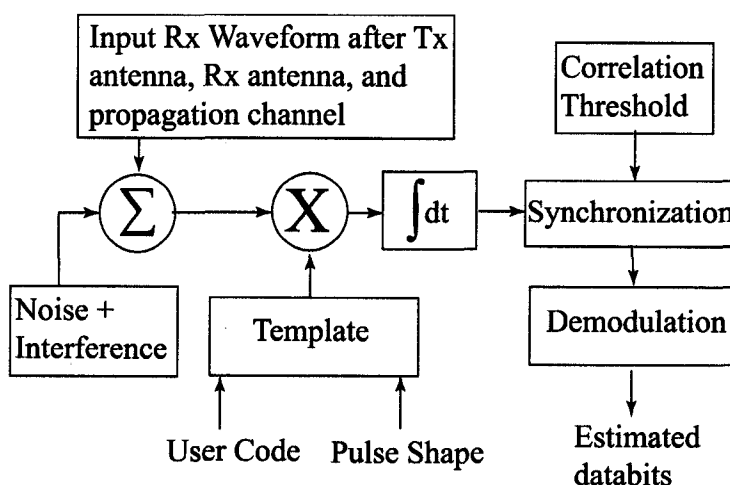


Figure 4.10. **Block diagram of the basic receiver model.** The various functional blocks in the model perform template generation, correlation, synchronization, acquisition and demodulation.

The matched filter correlation receiver is considered as the optimum receiver for pulsed antipodal (+/-) binary (0/1) communication [Proakis, 1995]. Figure 4.10 shows the block diagram for the correlator/matched filter receiver model. A correlator multiplies the received voltage waveform with a template waveform and then integrates the output of that process to yield a single DC voltage. The samples over a single bit time are multiplied and summed. With the proper template waveform, the output of the correlator is a measure of the relative position in time of the received pulses. The FCC regulations [FCC, 2002] place stringent bounds on the average transmit power of UWB systems. Hence UWB systems

are buried in the noise of other narrow band signals. To detect the UWB signals each bit of information is spread over multiple pulses and correlator output of the pulses are added together to average the noise and thereby raise the available signal energy above the noise floor. This process is called pulse integration and permits UWB receivers to acquire, track and demodulate UWB signals significantly below the noise floor. This also places bounds on the maximum achievable data rate of an UWB system.

Figure 4.11A shows the block diagram of the template waveform generator. The template waveform, identical to the generated UWB waveform, is matched to the received UWB waveform to decode the received information. The template uses the same PN sequence as the transmitter to generate the signal $w_0(t)$, which represent a '0' bit of information. As discussed in the PPM modulation part, there is an additional time delay δ associated with the waveform representing a '1' bit of information. The signal $w_1(t)$ is generated by adding a time delay to the $w_0(t)$. To identify if the received waveform represents a '0' or '1', the template must include both the '0' and the '1' bit waveform. The template signal $v(t) = w_0(t) - w_1(t)$ is generated as the template [Scholtz, 1993]. An example of template is shown in Figure 4.11B.

Figure 4.12A shows the block diagram for waveform acquisition. The correlator multiplies the received voltage waveform, $r(t)$ and the template waveform $v(t)$ to get the correlation history $C(t)$, given as

$$C(t) = \int_{-\infty}^{\infty} v(t - \tau)r(t)d\tau \quad (4.5)$$

where τ is a sample by sample time shift. At the time when a bit ('0' or '1') is transmitted, a peak value in the correlation is observed in the correlation history. Figure 4.12B shows an example of a correlation history for a '0' bit followed by a '1' bit. Each bit is spread over 4 pulses. Each pulse is the second derivative of the gaussian waveform. After the correlation is done, the receiver will first find the maximum values (C_m) of the correlation result in each bit time. Those peak values will indicate the time when a bit of information was transmitted. If there is no noise, all of the peak values will be the result of perfect

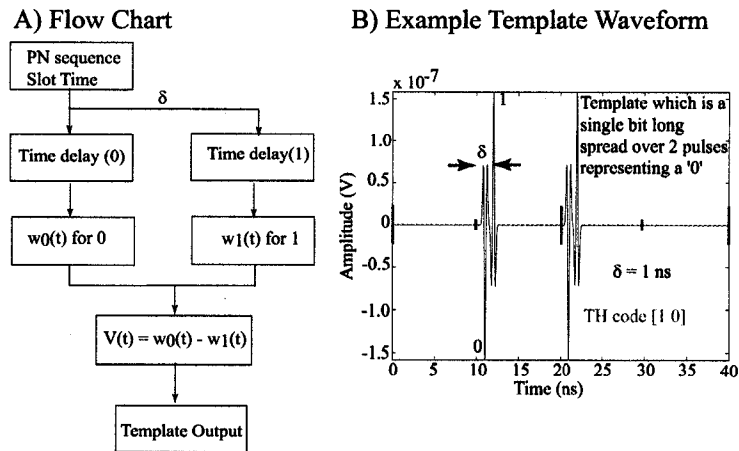


Figure 4.11. **Block diagram and output of the template generator model.** A) The template uses the same PN sequence as the transmitted signal to generate the signal which represents a bit '0'. The signal representing a bit '1', $w_1(t)$ has a additional time delay δ . To identify the transmitted information, the template waveform must include both the '0' and '1' bit waveform [Scholtz, 1993]. B) Example of a template output generated by the model.

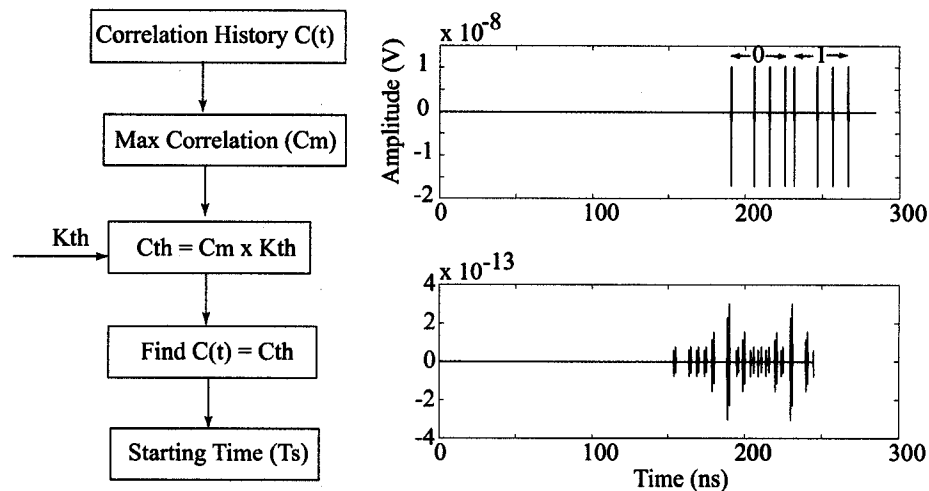


Figure 4.12. **Block diagram and output of the acquisition model.** A) Block diagram of the logical flow for signal acquisition in a matched filter receiver. B) A correlation history at the receiver when a message [0 1] is transmitted. Note that the receiver locks on to the starting time of each of the data frames in the received signal.

correlation and have the same value. In the presence of noise, the peak value will vary depending on the standard deviation of the noise. A coefficient (Kth) is used to indicate the variation of those peak values. This value needs to be set by trial and error. A threshold (Cth) value of correlation is set by scaling the maximum correlation with the coefficient Kth. The first position $C(t) = Cth$, is considered the start of the message signal. As discussed the peak value of the correlation corresponds to the start of a sequence of pulses corresponding to a bit. Hence the correlations will help synchronize the bit time and the frame time of the transmitted sequence of pulses but has no clue of determining if the transmitted bit was a '0' or a '1'. The additional delay associated with a '1' bit requires a synchronization bit to be transmitted at the beginning of a message sequence. In this model the synchronization bit is set to '0'. This means the transmitter needs to send a '0' before all the message information starts.

After the synchronization is achieved, the receiver starts to demodulate the received signal as shown in the block diagram in Figure 4.13. The start time T_s of the pulse sequence is calculated from the index of the maximum correlation calculated in the previous step. The criterion for demodulation is

$$Z = \int_{nT_s}^{nT_s+T_b} v(t-\tau)r(t)d\tau \quad (4.6)$$

where T_b is the time duration of the received signal corresponding to one bit of information and n ranges from 0 to the total number of bits, *numbits*. If the value of Z is greater than zero, a '0' bit is detected in the received signal. If the value of Z is less than zero, a '1' bit is detected in the received signal. This criterion is based on the shape of the template waveform [Scholtz, 1993]. This process is repeated every bit time till the last bit of information is decoded. The decoded information signal is compared with the transmitted information signal to calculate the number of bits in error or the bit error rate (BER). As the noise in the system is a random variable the simulations are repeated 50 times and an average bit error rate is calculated. The simulations were run 50 times because that reduced the difference in the calculated average bit error rate to $< 1e-3$ with a simulation time of

35 minutes.

Figures 4.14A and 4.14B show the case of one and two transmitting UWB signals received by a matched filter receiver 10 m away from the transmitting source(s). In both cases the transmitted bit energy to noise ratio is 5 dB. The bottom panels show the correlation history and the start time of each bit transmitted as detected by the matched filter receiver.

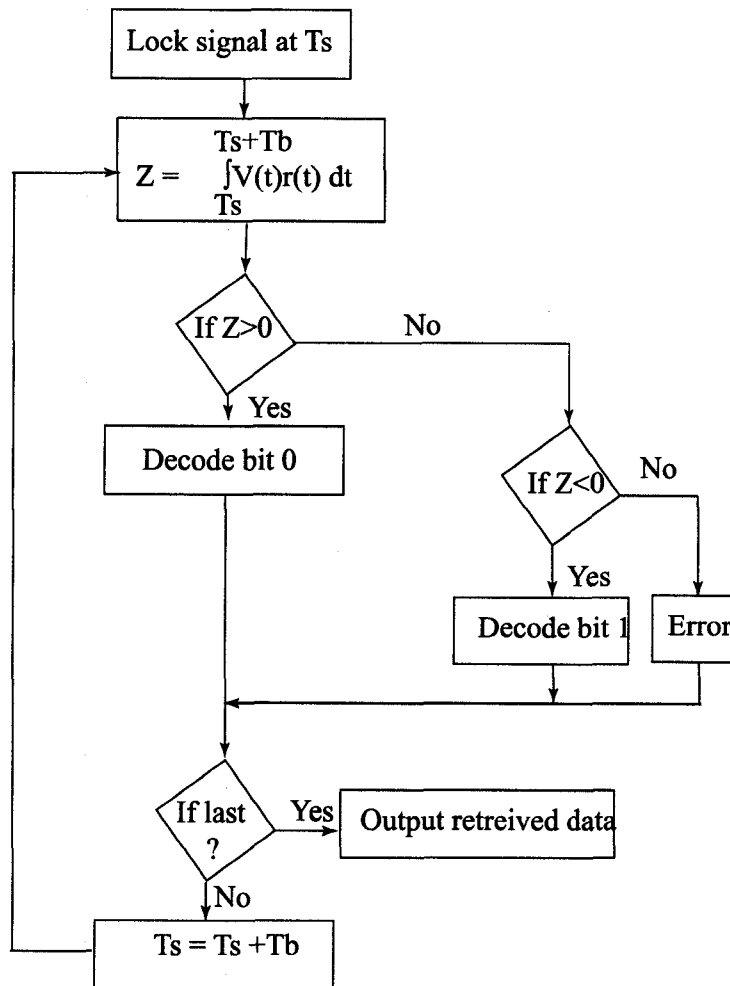


Figure 4.13. Block diagram for demodulation of the transmitted information from the received signal.

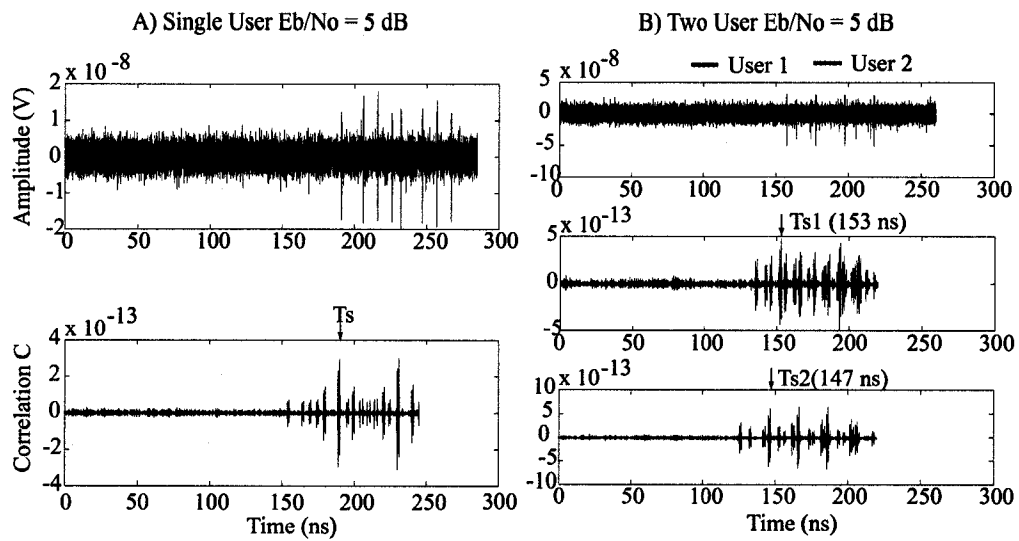


Figure 4.14. Example of pulse sequence with single and two UWB users transmitting with a 5 dB ratio of received bit energy to noise spectral density. The background noise is zero mean Gaussian noise with standard deviation $N_0/2$, where N_0 is the average noise spectral density. Concurrent UWB users cause collision of pulses occupying a single time slot. This causes errors in decoding the transmitted information.

4.2.6.2 Rake Receiver Model

The propagation channel causes multiple copies of the transmitted signal to reach the receiver delayed in time and scaled in amplitude depending on the properties of the channel. This introduces a redundancy in the received signal that is exploited by the rake receiver [Dibenedetto and Giancola, 2004].

Figure 4.15 shows the block diagram of a rake receiver with two fingers. The rake receiver is essentially a bank of L correlator/matched filter receivers with template waveforms which are delayed replicas of the original transmitted waveform. The demodulated outputs Z_l from each of the l fingers from 1 to L is combined to calculate whether a '0' or a '1' is detected. The model implements two methods of combining the correlator variables namely, (1) maximum ratio combining, and (2) selective combining. The maximum ratio combining method involves normalizing the l correlator output array to the maximum amplitude of the array in the 1 to L rake branches and then summing them up to calculate the net correlator output Z_{TOT} which is used for detection. Selective combining involves selecting a specified number S of strongest correlation outputs and summing them up to calculate Z_{TOT} .

The delay spread of a typical UWB propagation channel inside a building is approximately 5 to 14 ns [Foerster *et al.*, 2003]. An UWB signal has a bandwidth of 7.5 GHz and the number of possible multipath components for a 10 ns delay spread channel is ~ 75 . This would mean that to collect 100% of the free space energy, 75 rake branches are required. Clearly this is not possible. Hence careful choice of the number of rake branches that would provide a compromise between complexity and achievable BER performance for a specific configuration of antennas and the propagation channel is studied in the next section. The details of the m-files for each of the models are explained in a separate internal report [Venkatasubramanian, 2007].

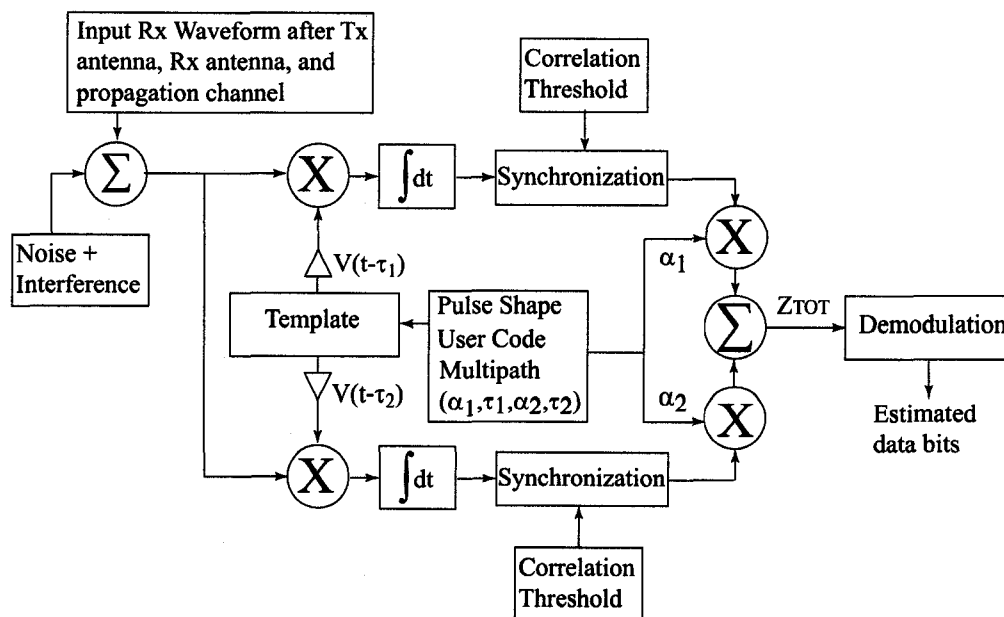


Figure 4.15. **Block diagram for a two arm rake receiver model.** Adapted from DiBenedetto and Giancola [2004].

4.3 Simulation Results - Case Studies

This section presents the simulated bit error rate performance for the following test cases to independently demonstrate the effect of the transmitting and receiving antenna and the propagation channel on the performance of a matched filter and a rake receiver. The three test cases considered are:

1. Case A - The effect of the transmitting and receiving antenna on the performance of a UWB communication system when the system is operating inside the anechoic chamber.
2. Case B - The effect of orientation of the transmitting antenna on the performance of a UWB communication system operating inside the anechoic chamber with two identical antennas.
3. Case C - UWB propagation channel effects on the performance of a UWB communica-

tion system operating in a line-of-sight (LOS) hallway and a non-line-of-sight (NLOS) room.

The simulation parameters for the UWB binary PPM system are listed in Table 4.1. The two identical antenna pairs chosen are the commercial Sunol Sciences DRH-118 broadband horn antennas and the oval dipole antennas that were discussed in detail in Chapter 2. These two antennas were chosen because the horn antenna is a directional high gain antenna which has been modified for an uniform gain of 10 ± 1.5 dB over a bandwidth of 1 GHz to 18 GHz. The oval antennas is a omnidirectional antenna with a dipole-like pattern in the 2 GHz to 6 GHz frequency range with a gain of 1.7 ± 0.5 dB.

Table 4.1. **Input parameters for the UWB communication system simulations presented in this chapter.**

Average Transmit Power P_T	0 dBm
Sampling frequency f_s	25 GHz
Center frequency f_c	3 GHz
Pulse width τ_p	0.5 ns
Data rate R_b	125 Mbps
PPM shift δ	0.5 ns
Pulses per bit N_s	1
Total Number of bits transmitted	10000
Input Pulse Shape	Gaussian

4.3.1 Case A - Effect of the Transmitting and the Receiving Antenna on the Bit Error rate of a Matched Filter and a Rake Receiver

The effect of the transmitting and the receiving antenna on the bit error rate of a matched filter and a rake receiver is calculated. The input parameters are as shown in Table 4.1. Figures 4.16A and 4.16B show the transmitting and receiving antenna impulse for the horn and the oval dipole antennas, discussed in detail in Chapter 2. The transmitting antenna response is shown as a black curve and the receiving antenna response is shown as a red curve. Note that the horn antenna impulse response has a narrower time duration (~ 0.6

ns) compared to the oval antenna (~ 1.25 ns). Also note that the horn antenna has a narrower cycle time (~ 0.25 ns) compared to the oval antenna (~ 0.35).

Figure 4.16C shows the calculated bit error rate as a function of transmitted bit energy (E_b) to noise spectral density (N_0), E_b/N_0 , for a matched filter receiver with an oval-to-oval (red curve) and a horn-to-horn (black curve) communication link. The horn-to-horn communication link has a gain of 20 dB compared and the oval-to-oval link has a gain of 3.4 dB. In spite of the reduced gain, the oval antennas show a lower bit error rate than the horn antennas for a $E_b/N_0 = 10$ dB. This is because the horn antennas have additional ringing in their impulse response due to the limited bandwidth of the measurement (300 kHz to 9 GHz) compared to the bandwidth of the antennas (1 GHz to 18 GHz). So this implies that the matched filter receiver is sensitive mainly to the time dispersion of the antennas and not the gain of the antennas. This would also mean that a comparable bit error rate performance can be achieved with a low gain, dispersion-less antenna rather than a higher gain dispersive antenna.

Figures 4.16D, 4.16E, and 4.16F show the calculated bit error rate as a function of E_b/N_0 for a rake receiver with 2, 10, and 20 fingers/branches, respectively. The rake receiver can use the additional ringing and the higher gain of the horn antenna therefore performs better for the horn antenna pair compared to the oval antenna pair. The difference in the bit error rate increases from a factor of 2 for a rake with 2 branches to a factor of 8 for a rake with 20 branches. Larger than 20 branches showed marginal improvement in the rake performance.

4.3.2 Case B - Effect of the Transmitting Antenna Orientation on the Bit Error Rate of a Matched Filter and a Rake Receiver

The effect of the orientation of the transmitting oval dipole antenna on the bit error rate of a matched filter and a rake receiver is calculated. The receiving horn antenna is held fixed with its broadside direction facing the transmitting oval dipole antenna. The measured band-limited impulse response of the oval dipole antenna in the vertical and the horizontal plane, discussed in detail in chapter 2, is used in the calculations presented in this section.

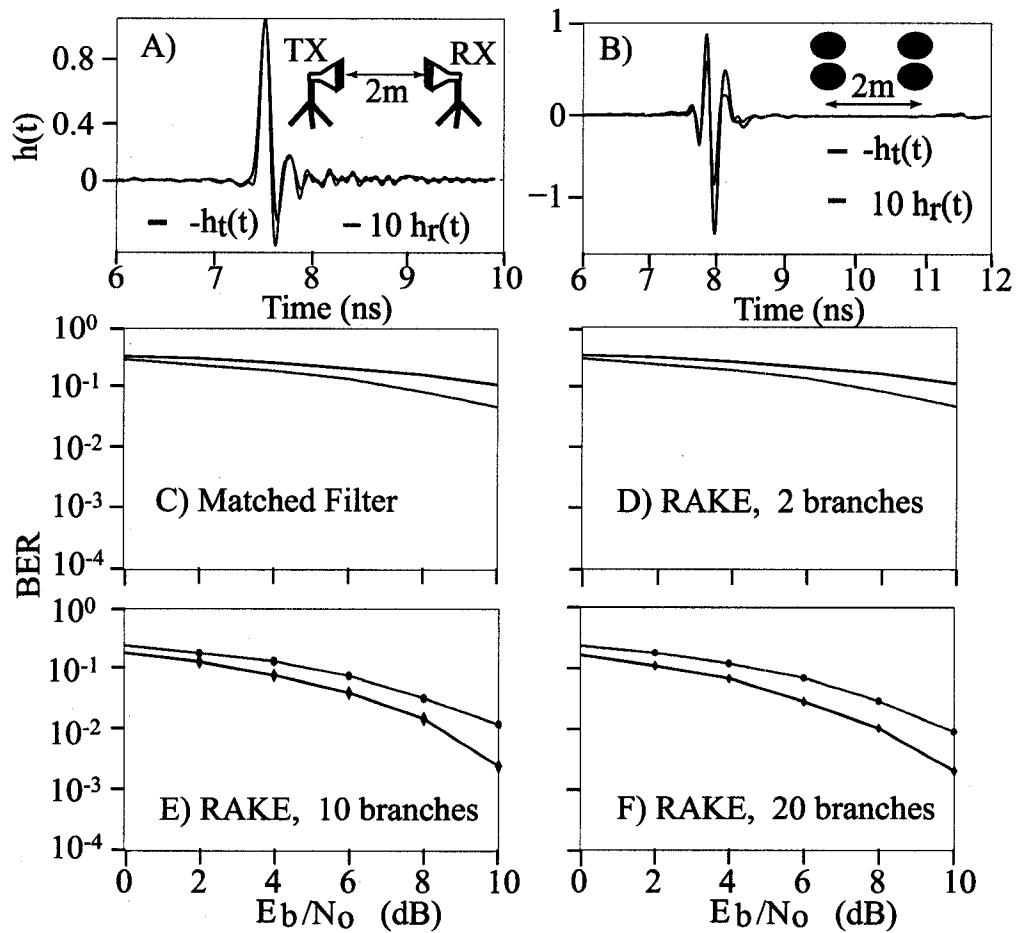


Figure 4.16. Bit error rate performance curves as a function of transmitted bit energy (E_b) to noise density (N_0) ratio for a matched filter and a rake receiver with two identical antenna pairs in the anechoic chamber. (A) The band-limited impulse response of a horn-to-horn antenna system 2 m apart in the anechoic chamber. (B) The band-limited impulse response of an oval-to-oval antenna system 2 m apart in the anechoic chamber. (C) Matched filter receiver. (D)-(F) rake receiver with 2, 10, and 20 branches, respectively.

Figures 4.17A and 4.17B show the measured band-limited impulse response of the oval dipole antenna for two orientations angles of the antenna in the vertical and the horizontal planes, respectively. Figure 4.17C shows the bit error rate as a function of E_b/N_0 for a matched filter receiver model for the input parameters listed in Table 4.1. There is a factor of 100 improvement in the bit error rate of the matched filter when the oval antenna is radiating in the broadside ($\theta = 90^\circ$) direction compared to the oval antenna radiating along its axis ($\theta = 0^\circ$) in the vertical plane. This is because: (1) the amplitude of the radiated pulse drops by 15 dB from the broadside direction to the direction along the axis of the oval, and (2) the time duration of the impulse response increases by a factor of 5 from the broadside direction to the direction along the axis of the oval. The time duration of the impulse response is the duration containing 90% of the total energy contained in the impulse response as discussed in Appendix B.1. In the horizontal plane the oval antenna shows comparable performance in the ($\phi = 90^\circ$ and ($\phi = 0^\circ$)) directions with a 10% improvement in the bit error rate for the ($\phi = 0^\circ$) direction owing to increased amplitude in this direction.

Figures 4.17D, 4.17E, and 4.17F show the bit error rate as a function of E_b/N_0 for a rake receiver with 2, 10, and 20 branches. As the number of branches increases the rake receiver captures more of the transmitted energy in different directions. For a rake receiver with 20 branches the bit error rate performance has $< 10\%$ variation in all directions. It should be noted that the rake receiver requires prior knowledge of the impulse response of the antennas in different directions. Hence the performance of the rake receiver depends on the accuracy with which the antenna response is estimated and the number of branches in the rake. An increase in the number of branches also means increased complexity and more power consumption at the receiver but these practical limitations will not be considered in this thesis.

Figure 4.18 shows the bit error rate performance as a function of E_b/N_0 for a rake receiver with two branches and perfect knowledge of only the antenna impulse response in the broadside direction in the elevation plane. As can be seen the bit error rate increases

by up to a factor 200 for $\theta = 60^\circ$, 30° , and 0° , respectively, for $E_b/N_0 = 10$ dB. This calculation provides a quantitative estimate of the effect of error in the estimation of the impulse response used by the rake receiver on its bit error rate performance. The figure also shows that the best achievable bit error rate for a rake receiver with 2 branches and a transmitted $E_b/N_0 = 10$ dB is 10^{-2} . This means that 1 bit is in error for every 100 bits transmitted.

4.3.3 Case C - Effect of the UWB Propagation Channel on the Bit Error Rate of a Matched Filter and a Rake Receiver

The effect of the propagation channel on the bit error rate as a function of E_b/N_0 for a matched filter and a RAKE receiver with 2, 10, and 20 branches, respectively, is calculated. The results in the previous section showed that the transmitting and receiving antenna distort the pulse and this caused degradation in the bit error rate of the UWB receivers. The propagation channel would further distort the pulse and therefore it is expected that it would further degrade the bit error rate performance of the UWB receivers. Hence the range of the E_b/N_0 over which the calculations are performed is increased to 20 dB from 10 dB. The measured band-limited impulse response of the propagation channel for the line-of-sight (LOS) scenario, presented in Chapter 3 (as Case B in Figure 3.14), is used in the bit error rate calculations. Figure 4.19A reproduces the empirical band-limited impulse response for the LOS case. Figure 4.19B shows the bit error rate as a function of E_b/N_0 for a matched filter (solid blue curve) and a rake receiver with 20 (solid red curve) and 200 (solid black curve) branches. The circles represent an oval-to-oval antenna link and the diamonds represent horn-to-horn antenna link. The matched filter receiver shows an improved performance for the oval antennas compared to the horn antennas similar to the result observed in Figure 4.16. The rake receiver shows an improvement in bit error rate by a factor of 20 when the horn antennas are used instead of the oval dipole antennas. An increase in the number of rake branches by a factor of 10 improves the bit error rate only by a factor of 3. This suggests that the propagation channel places a stringent bound on

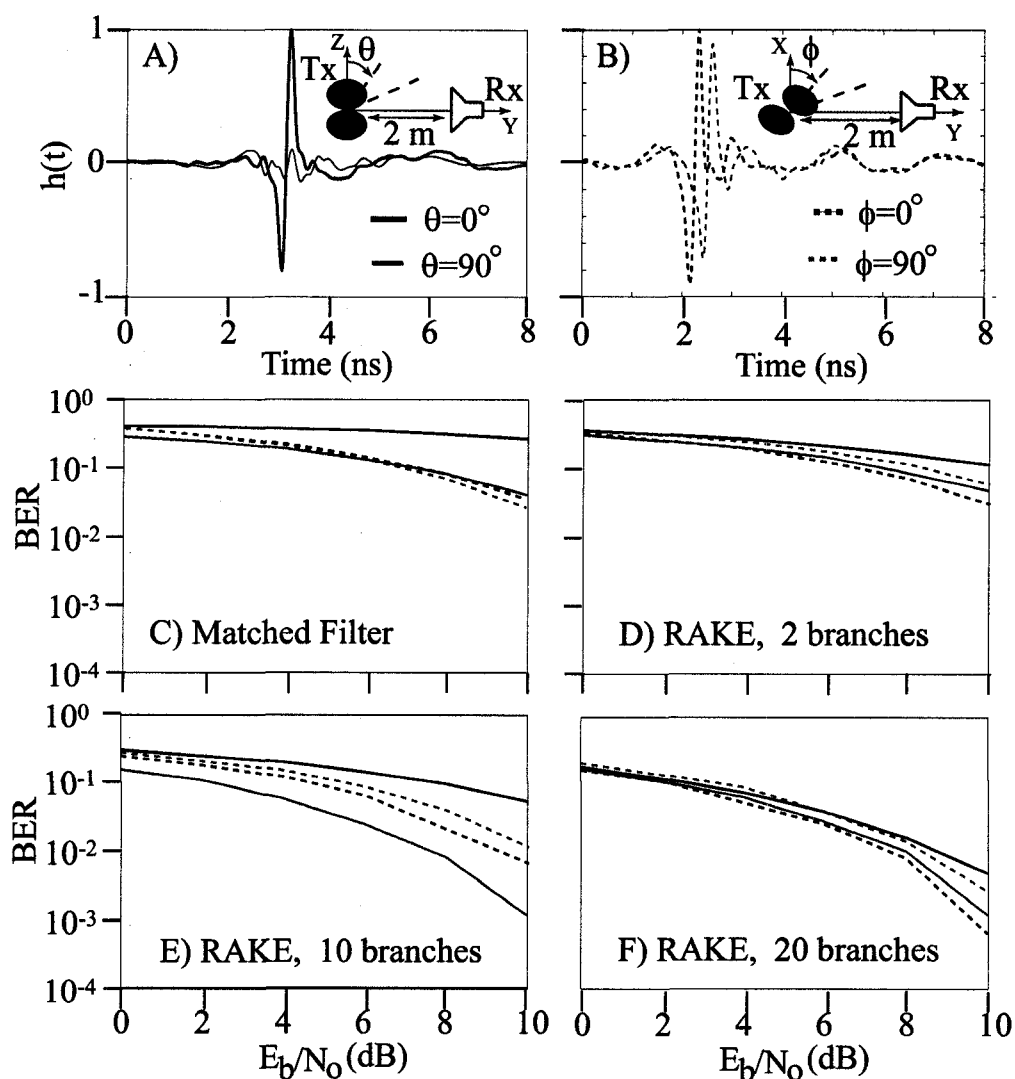


Figure 4.17. The effect of transmitting antenna orientation on the bit error rate as a function of E_b/N_0 for a matched filter and a rake receiver. (A) The band-limited impulse response of a oval-to-horn antenna system 2 m apart in the anechoic chamber with the oval antenna radiating along the $\theta = 90^\circ$ direction (solid red curve) and $\theta = 0^\circ$ direction (solid black curve) in the vertical plane. (B) The band-limited impulse response of an oval-to-horn antenna system 2 m apart in the anechoic chamber with the oval antenna radiating along the $\phi = 90^\circ$ direction (dotted red curve) and $\phi = 0^\circ$ direction (dotted black curve) in the horizontal plane. (C) BER as a function of E_b/N_0 for a matched filter receiver. (D)-(F) BER as a function of E_b/N_0 for a rake receiver with 2, 10, and 20 branches, respectively. The solid red BER curves represent antenna orientation angles in the vertical plane and the dotted curves represent the antenna orientation angles in the horizontal plane.

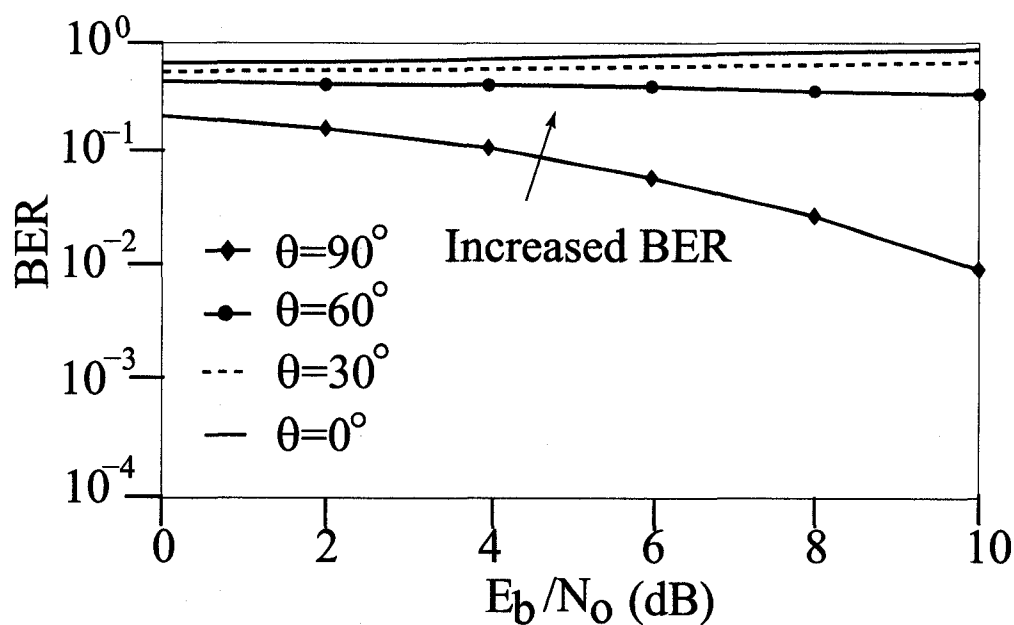


Figure 4.18. Effect of template selection on the bit error rate of a rake receiver.

the performance of a UWB receiver.

4.4 Summary of Results

The calculations presented in the previous section illustrate the following key results: (1) A modular simulation approach has been developed to calculate the bit error rate as a function of E_b/N_0 for two UWB receiver models incorporating the empirical impulse responses of the antennas and the propagation channel. The simulation approach permits independent investigation of the relative importance of factors such as antenna pattern and propagation channel effects on the transmitted waveform and the related degradation in system performance. (2) The bit error rate of a matched filter and a rake receiver are strongly affected by the orientation of the transmitting and the receiving antenna. An increase in bit error rate by up to a factor of 100 is observed for the matched filter receiver as the antenna is rotated in the vertical plane. (3) The matched filter receiver is more sensitive to the time

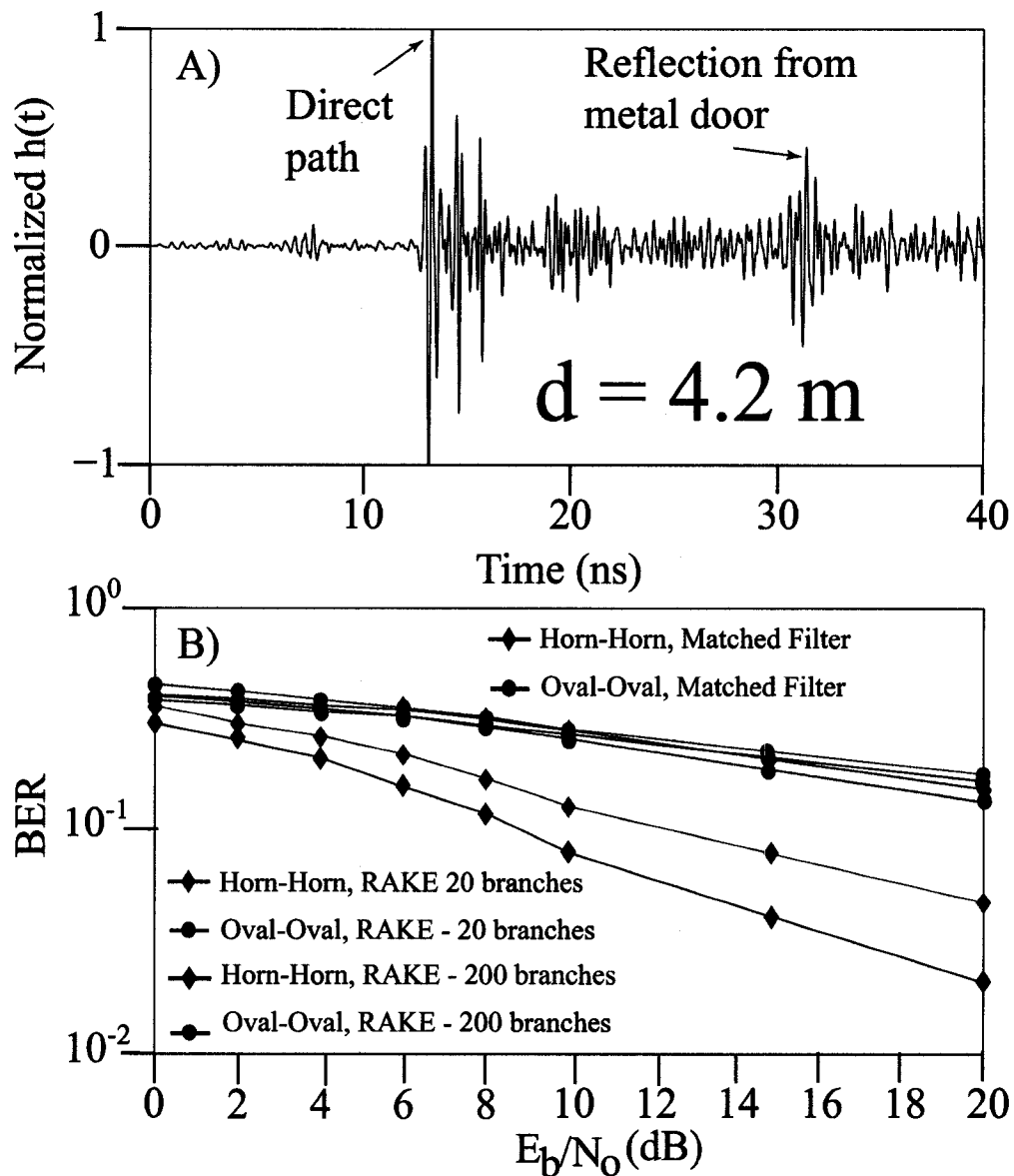


Figure 4.19. The effect of the propagation channel on the bit error rate as a function of E_b/N_0 for a matched filter and a RAKE receiver with 20, and 200 branches.

dispersion of the antenna and the propagation channel compared to the antenna gain. (4) The rake receiver shows marginal improvement (factor of 3) in the bit error rate when the number of branches is increased from 20 to 200 for LOS propagation.

4.5 Discussion

Based on the calculations presented in this chapter an adaptive receiver can be envisioned. It is assumed that the receiver has perfect knowledge of the properties of the pulse generated at the transmitter. The receiver first sends a single pilot pulse. The pulse is radiated by an antenna, propagates through the channel and is received by another antenna at the transmitter. The antennas and the propagation channel will distort the pulse. The received pulse is processed in software by the transmitter to estimate the impulse response of the antennas and the propagation channel. A mirror image of the estimated impulse response is used to pre-distort the pulse such that the received pulse has the exact same properties as the transmitted pulse. Hence this will result in improved bit error rate performance at the receiver. Some work has been done on various aspects of an adaptive receiver model [Wang *et al.*, 2005; McKinney and Weiner, 2006] but further investigation is required.

4.6 Concluding Remarks

The calculation presented in this chapter suggest that the antenna and the propagation channel will distort the transmitted pulse. This distortion depends on the orientation and geometry of the antenna, geometry of the propagation channel, and the properties of the transmitted pulse. hence all these parameters place bounds on the bit error rate of a UWB receiver.

The next chapter discusses the important conclusions drawn from the research work presented in this dissertation and lists the shortcomings of the adopted experimental and theoretical methodology and the directions for future research.

Chapter 5 Conclusions and Recommendations

5.1 Introduction

This chapter lists and discusses the results and important conclusions drawn from the experimental and theoretical work presented in this dissertation. The chapter then discusses the deficiencies in the experimental and numerical methods adopted and concludes by discussing some of the unanswered research questions that have risen based on the present work.

5.2 Summary of Conclusions

The conclusions drawn from the measurements, numerical simulations and theoretical analysis presented in this dissertation are listed below:

1. The experimental and numerical results presented in Chapter 2 suggest that there is a strong relationship between the geometry and the orientation of a UWB antenna to the radiated pulse properties (e.g., pulse width, cycle time, bandwidth, center frequency). The reciprocity relation for oval dipole antennas is derived from the measurements:
 - (i) The transmitting antenna radiates the derivative of the input UWB waveform in the time domain or the spectrum of the radiated electric field is 90° out of phase from

the spectrum of the input voltage waveform. (ii) The spectrum of the received voltage waveform is in phase with the spectrum of the electric field waveform incident on the antenna.

2. The experiments and simulations in Chapter 2 show that the polarization of the radiated electric field waveform and the cross polarization ratio is closely related to the geometry of the UWB antenna. For the oval dipole antenna with an axial ratio of 0.8 it is shown that the horizontally polarized fields are 15 dB down compared to the vertically polarized fields in the broadside direction.
3. In Chapter 3, measurements on ultra-wideband (UWB) pulse propagation over the ground show the presence of three distinct propagation regimes: (1) in the first regime, the signal power decreases as $\sim d^{-2}$, where d is the separation distance between the transmitter and the receiver; (2) in the second regime, the signal power decreases on the average as $\sim d^{-2}$ with distance, but exhibits interference maxima and minima; (3) in the third regime, the signal power decreases as $\sim d^{-4}$. Theoretical analysis indicates two characteristic length scales d_1 and d_2 , called first and second breakpoint distances, determine the sizes of the three propagation regimes. These characteristic lengths depend both on the geometrical parameters such as the heights of the transmitter (h_1) and the receiver (h_2) over the ground as well as on UWB pulse properties such as pulse duration (τ_p) and cycle time (τ_c). Simple expressions for break points exist when $h_1, h_2 \gg c\tau_p$ and $d \gg h_1$: $d_1 \approx 4h_1h_2/c\tau_p \approx 4h_1h_2B/c$, and $d_2 \approx 4h_1h_2/c\tau_c \approx 4h_1h_2f_c/c$, where $B \sim 1/\tau_p$ is the bandwidth and $f_c \sim 1/\tau_c$ is the center frequency of the UWB pulse. For a given transmitter height h_1 , the loci of first and second breakpoints in the (d, h_2) plane are hyperbolas with the transmitter and its image as the foci.
4. A Finite Difference Time Domain (FDTD) code is developed to run on 8 parallel computers at the Arctic Region Super Computing Center (ARSC) at the University of Alaska Fairbanks (UAF). The FDTD simulations for UWB antennas and UWB pulse

propagation shown in Chapters 2 and 3 show excellent agreement with measurements.

5. A modular simulation approach is developed to calculate the bit error rate of two UWB receiver models for different measured and simulated antenna and propagation channel models. The simulation framework permits independent investigation of the relative importance of factors such as antenna pattern versus waveform distortion in the degradation of the system performance.
6. The bit error rate of a matched-filter receiver depends strongly on the transmitting and receiving antenna's geometry and relative orientation. An increase in bit error rate by up to a factor of 100 is observed as we rotate the transmitting antenna from the broadside direction to the end-fire direction keeping the receiving antenna fixed and aligned along the local vertical. This is both due to the change in the amplitude and the time dispersion of the radiated pulse.
7. The propagation channel places a stringent bound on the bit error rate and data rate of a matched-filter receiver.

5.3 Deficiencies in the Presented Work and Suggested Improvements

There are several deficiencies in the algorithms employed in the experiments and numerical calculations presented in this dissertation related to the assumptions made. Some deficiencies are listed as follows:

1. The algorithm to calculate the transmitting and the receiving antenna transfer function from the measured scattering parameters, proposed by Qing *et al.* [2006], assumes perfect matching between the antennas and the ports of the vector network analyzer. The approach also assumes that the transmitting antenna transfer function is related to the receiving antenna transfer function by a $j\omega$ factor or the transmitting antenna impulse response is related to the derivative of the receiving antenna impulse response.

It has been shown by Schantz [2005] that the transmitting and the receiving antennas are related by a derivative only if the antennas are constant aperture antennas. For constant gain antennas the transmitting antenna transfer function is related to $1/j\omega$ times the receiving antenna transfer function. So the measured impulse responses in this work assumes a specific reciprocity relationship. An alternative approach to measuring the impulse response of a UWB antenna is by using a small antenna that is electrically short in the transmission frequency range and whose transmitting and receiving impulse response is known. Then the impulse response of the antenna under test can be measured directly from the scattering parameter measurements. This eliminates assumptions on the relation between the transmitting and the receiving antenna transfer functions and on the antennas.

2. The FDTD code developed uses OpenMP C to calculate the electric and magnetic fields radiated by a antenna geometry at each point in a three dimensional grid. The calculations over the entire domain at each time step is divided between a maximum of 8 processors in one node. This limits the maximum possible domain size and the speed of the FDTD code owing to the limited processing power and memory available at each node. This deficiency could be overcome by modifying the current FDTD simulation code to use message passing interface (MPI) which would break the domain into a maximum of 8 parts and supply each part to a separate node. Each node will then further split that smaller domain into 8 smaller chunks and supply it to each of the 8 processors. Information regarding boundary cells would be communicated back and forth between the various nodes. Hence the workload of the simulation domain is shared by a total of 64 processors.
3. The time domain measurements presented in Chapter 2 involved measuring the received voltage waveform without any synchronization between the generated waveform and the received waveform at the oscilloscope. If an exact estimate of the delay of the received pulse needs to be measured then the oscilloscope needs to be triggered at the same time the transmitting antenna is excited by the input pulse. This could be

achieved by designing a power divider that would distribute the power in the input pulse equally to the transmitting antenna and the trigger of the scope. This measurement could provide an estimate of the location of the phase center of the antenna and how it moves as a function of the input pulse properties and antenna geometry.

4. In Chapter 3, the RSS of the UWB pulse propagating over ground is calculated from the peak amplitude of the pulse. There are other measures of the RSS like the energy in the pulse which may provide different propagation characteristics.
5. The frequency domain experiments presented in Chapter 3 are for a specific configuration of the antennas and a specific structure of the propagation channel. Hence the empirical impulse response channel models used in the simulations are specific to the propagation geometry of the experiment. More generalized conclusions would require several measurements that would lead to statistical variations in the amplitude and delay of the multiple propagation paths reaching the receiving antenna. This would aid in building statistical models of the propagation channel based on measurements.

5.4 Outstanding Research Questions and Recommendations

This dissertation work has led to the following unsolved research problem listed below along with recommendations for future work:

1. Is there a general reciprocity relationship between two UWB antennas? The measurements presented in Chapter 2 assumed that the transmitting antenna transfer function is related to the receiving antenna transfer function as [Lu *et al.*, 2006]

$$H_t(\omega, \theta_t, \phi_t) \propto j\omega H_r(\omega, \theta_r, \phi_r)$$

Is this a general relationship for all UWB antennas? Could this relationship be utilized to come up with antenna designs whose transmitting and receiving response are

identical and related as

$$H_t(\omega, \theta_t, \phi_t) = H_r(\omega, \theta_r, \phi_r) = \sqrt{(j\omega)}H(\omega, \theta, \phi)$$

The $\sqrt{(j\omega)}$ term implies fractional derivatives. Could the antenna geometry be modified to yield antennas whose impulse responses are fractional derivatives. Such antennas would be very useful in controlling the properties of the radiated and received UWB pulse.

2. The work presented in Chapter 2 showed that the oval dipole antennas have different radiation properties when the axial ratio of the ovals is varied. Could this potentially be used to design antennas whose geometry is a combination of ovals with different axial ratios resulting in antenna properties favorable to an application? How would a combination of ovals change the radiation properties of each of the ovals taken separately?
3. The work presented in Chapter 2 showed that “bulbous” antennas have a broader impedance bandwidth than “skinny” antennas because they reduce the amount of input energy lost to the reactive fields surrounding the antenna. Can the handshake of energy between the reactive “near” fields and radiation “far” fields be tracked? There is some work done in the past on using energy flow diagrams to design efficient antennas [Schantz, 2001; 1995]. This work still does not provide a general picture of how and where the energy decouples from the antenna other than for a few specific antenna geometries and input pulse shapes.
4. The work presented in Chapter 3 developed a new hyperbola model to relate the radiated UWB pulse properties and the geometry of the propagation channel to the RSS. This work relies on the fact that the cycle time of the radiated pulse remains unaltered for a broad range of radiation angles from the transmitting antenna. This is not true for many commonly available UWB antennas like the TEM horn and frequency independent antennas [Schantz, 2005]. How would this model be modified

to estimate the character of the RSS when the radiated UWB pulse properties change in different directions from the transmitting antenna?

5. The work presented in chapter 3 has shown that maxima and minima in the signal strength will exist in complicated line-of-sight and non-line-of-sight scenarios, but can the properties of the generated and radiated pulses (antenna design) be controlled over f_c and B to follow the maxima locations? Can this model be used to propose spatial encryption codes that would control the signal strength at different locations by changing the properties of the radiated waveform?
6. The frequency domain measurements and the FDTD simulations of UWB pulse propagation inside a hallway suggest that metallic structures cause strong reflections. Can these reflections be used to improve the signal to noise ratio in non-line-of-sight locations. Can experimental and numerical work validate this assertion? How do metallic structures alter the shape of the UWB waveform? Can properties of the antenna and the generated waveform be altered to utilize these structures such as metal doors and dust bins present in a channel to provide propagation paths which enhance the signal amplitude at the receiver thereby improving bit error rate performance?
7. How would simultaneous transmission of multiple UWB receivers affect the bit error rate of a matched filter and a rake receiver? What is the maximum number of UWB receivers that a transmitter can transmit information to with a specific bit error rate and data rate for a specific set of antennas and propagation scenarios? Would signals from cellular phones and global positioning systems (GPS), which occupy similar frequency bands, affect the performance of a UWB receiver? If so, how and by how much? The modular simulation approach developed provides a method to perform calculations to answer many such questions within the assumptions of the approach.

References

- [Allen *et al.*, 2006] Allen, B., M. Dohler, E. E. Okon, W. Q. Malik, A. K. Brown, and D. J. Edwards, *Ultra-Wideband Antennas and Propagation for Communications, Radar and Imaging*. London, UK-Wiley, 2006.
- [Aroonprapararat *et al.*, 2006] Aroonprapararat, S., S. Pichaya, S. Promwong, and J. Takada, *Path Loss Expressions of Ultra Wideband Ground Reflection Channel*, *International Symposium on Communications and Information Technologies*, 2006.
- [Astаниn and Kostylev, 1989] Astаниn, L. Y., and A. A. Kostylev, *Principles of Super wideband Radar Measurements*, Moscow, Radio I Svyaz', 1989.
- [Bennia and Riad, 1992] Bennia, A., and S. M. Riad, *Filtering Capabilities and Convergence of the Van-Cittert Deconvolution Technique*, *IEEE Transactions on Instrumentation and Measurement*, vol. 41, no. 2, pp. 246 - 250, April, 1992.
- [Berenger, 1994] Berenger, J. P., *A perfectly matched layer for the absorption of electromagnetic waves*, *J. Comput. Phys.*, vol. 114, no. 1, pp. 185 - 200, 1994.
- [Bertoni, 2000] Bertoni, H. L., *Radio propagation for modern wireless systems*, Prentice Hall, New Jersey, 2000.
- [Bracewell, 1999] Bracewell, R. N., *The Fourier transform and its applications*, McGraw-Hill College, third edition, November 1999.

- [Cardinali *et al.*, 2006] Cardinali, R., L. D. Nardis, M. G. Di Benedetto, and P. Lombardo, UWB Ranging Accuracy in High- and Low-Data-Rate Applications, *IEEE Transactions on Microwave Theory and Techniques*, vol. 54, no. 4, April 2006.
- [Choi and Stark, 2002] Choi, J. D., and W. E. Stark, Performance of ultra-wideband communications with suboptimal receivers in multipath channels, *IEEE J. Selected Areas Comm.*, vol. 20, pp. 1754 - 1766, Dec. 2002.
- [Cotton *et al.*, 1999] Cotton, M. G., R. J. Achatz, Y. Lo, and C. L. Holloway, Indoor Polarization and Directivity Measurements at 5.8 GHz, NTIA Report 00-372, U.S. Department of Commerce, November 1999.
- [Cramer *et al.*, 2002] Cramer, R.J.-M., R. A. Scholtz, M. Z. Win, Evaluation of an ultra-wide-band propagation channel, *IEEE Transactions on Antennas and Propagation*, vol. 50, no. 5, pp. 561 - 570, May 2002.
- [Cramer *et al.*, 1999] Cramer, R. J. M., M. Z. Win, and R. A. Scholtz, On the Analysis of UWB Communication Channels, 1999 IEEE Military Communications Conference Proceedings, vol. 2, pp. 1191 - 1195, MILCOM 1999, 31 Oct. - 3 Nov., 1999.
- [Davis *et al.*, 2007] Davis, B., C. Grosvenor, R. Johnk, D. Novotny, J. B. Jarvis, and M. Janezic, Complex Permittivity of Planar Building Materials Measured With an Ultra-Wideband Free-Field Antenna Measurement System, *Journal of Research of the National Institute of Standards and Technology*, vol. 112, no. 1, January 2007.
- [DiBenedetto and Giancola, 2004] DiBenedetto, M. G., and G. Giancola, *Understanding ultra wideband radio fundamentals*, Prentice Hall, 2004.
- [Dohler *et al.*, 2004] Dohler, M., B. Allen, A. Armogida, S. McGregor, M. Ghavami, and A. H. Aghvami, A new twist on UWB path-loss modelling, VTC Spring, Milan, Italy, May 2004.

- [Durisi *et al.*, 2003] Durisi, G., J. Romme, and S. Benedetto, Performance of TH and DS UWB multiaccess systems in presence of multipath channel and narrowband interference, in Proc. International Workshop on Ultra Wideband Systems, Oulu, Finland, June 2 - 5, 2003.
- [FCC, 2002] FCC, Revision of Part 15 of the Commission's Rules Regarding Ultra-Wideband Transmission Systems, First Report and Order, ET Docket 98-153, FCC 02-8, adopted/ released Feb. 14/Apr. 22, 2002.
- [Foerster *et al.*, 2003] Foerster, J., V. Somayazulu, and S. Roy, Intel CFP Presentation for a UWB PHY, IEEE 802.1503, March 3, 2003.
- [Foster *et al.*, 1990] Foster, C. *et al.*, Assesment of Ultra Wideband Technology, IEEE Aersospace and Electronic Systems Magazine, pp. 44-49, November 1990.
- [Fowler *et al.*, 1990] Fowler, C., J. Entzminger, and J. Corum, Assesment of Ultra Wideband Technology, Summary Report of the DARPA/OSD Panel to examine state-of-the-art, benefits, and limitations of UWB Technology, 1990.
- [Ghavammi *et al.*, 2007] Ghavami, M., L. B. Michael, and R. Kohno, Ultra Wideband Signals and Systems in Communication Engineering, Second edition, Wiley, 2007.
- [Guofeng *et al.*, 2006] Guofeng, L., L. Greenstein, and P. Spasojevic, Symmetry Properties of Antennas in Transmitting and Receiving UWB Signals, Antenna Technology Small Antennas and Novel Metamaterials, 2006 IEEE International Workshop on, pp. 76-79, March 6 - 8, 2006.
- [Hallikainen *et al.*, 1986] Hallikainen, M., F. Ulaby, M. Abdelrazik, Dielectric Properties of Snow in the 3 to 37 GHz Range, IEEE Transactions on Antennas and Propagation, vol. 34 , no. 11, pp. 1329 - 1340, Nov. 1986.
- [Hawkins *et al.*, 2005] Hawkins, J. G., B. A. Johnson, C. E. Mayer, V. Sonwalkar, and A. Venkatasubramanian, Anchoic Chamber and Instrumentation Calibration Results,

Subcontract Report submitted to Kachemak Research Development Inc., Prime Contract N00164-05-D-6653, August 10, 2005.

- [Heidary, 2004] Heidary, K., Ultra-wideband (UWB) incidence on multiple dielectric interfaces, Antennas and Propagation Society International Symposium, 2004. IEEE , vol. 2, pp. 1315 - 1318, 20 - 25 June 2004.
- [Holloway *et al.*, 1997] Holloway, C. L., P. L. Perini, R. Delyser, and K. C. Allen, Analysis of composite walls and their effect on shon-path propagation modelling, IEEE Trans. in Veh. Technol., vol. 46, pp. 730 - 738, August 1997.
- [Iverson, 1991] Iverson, D., Extracting real samples from complex sampled data, IEEE Electronics Letters, vol. 27, no. 21, pp. 1976 - 1978, 1991.
- [Kanda, 1980] Kanda, M., Transients in a resistively loaded linear antenna compared with those in a conical antenna and a TEM horn, IEEE Trans. Antennas Propag., vol. 28, pp. 132 - 136, 1980.
- [Kissick, 2001] Kissick, W. A., The temporal and spectral characteristics of ultrawideband signals, NTIA Report 01-383, January 2001.
- [Kraus and Marhefka, 2001] Kraus, J. D., and R. J. Marhefka, Antennas, Hardcover, 3rd ed., McGraw-Hill Higher Education, November 2001.
- [Liu *et al.*, 2006] Liu, J., M. Dohler, B. Allen and M. Ghavami, Power-loss Modelling of Short-Range Ultra Wideband Pulse Transmissions, IEE Proceedings Communications, Special Issue on Ultra Wideband Systems, Technologies and Applications, vol. 153, no. 1, pp. 143 - 152, February 2006.
- [Lu *et al.*, 2004] Lu, G., I. Korisch, L. Greenstein, and P. Spasojevic, Antenna modelling using linear elements, with applications to UWB, IEEE Antennas and Propagation Society International Symposium, vol. 3, pp. 2544-2547, 20-25 June 2004.

- [Malik *et al.*, 2007] Malik, W. Q., D. J. Edwards, and C. J. Stevens, Frequency dependence of fading statistics for ultrawideband systems, *IEEE Trans. Wireless Commun.*, vol. 6, no. 3, pp. 800 - 804, Mar. 2007.
- [Malik *et al.*, 2006] Malik, W. Q., D. J. Edwards and C. J. Stevens, Angular-spectral antenna effects in ultra wideband communications links, *IEE Proc.-Commun.*, vol. 153, no. 1, February 2006.
- [Malik *et al.*, 2004] Malik, W. Q., D. J. Edwards, and C. J. Stevens, Experimental evaluation of rake receiver performance in a line-of-sight ultra-wideband channel, in *Proc. Joint IEEE Ultra-Wideband Sys. Tech. and Int. Workshop Ultra-Wideband Sys.* Kyoto, Japan, May 2004.
- [Matzler *et al.*, 1996] Matzler, C., Microwave Permittivity of Dry Snow, *IEEE Transactions on Geoscience and Remote Sensing*, vol. 34, no. 2, pp. 573 - 581, March 1996.
- [McKinney and Wiener, 2006] McKinney, J. D., and A. M. Weiner, Compensation of the Effects of Antenna Dispersion on UWB Waveforms via Optical Pulse-Shaping Techniques, *IEEE Transactions on Microwave Theory and Techniques*, vol. 54, no. 4, April 2006.
- [McLean *et al.*, 2006] McLean, J.S., H. Foltz, and R. Sutton, Conditions for Direction-Independent Distortion in UWB Antennas, *IEEE Transactions on Antennas and Propagation*, vol. 54, no. 11, November 2006.
- [McLean *et al.*, 2005] McLean, J.S., H. Foltz, and R. Sutton, Pattern descriptors for UWB antennas, *Antennas and Propagation, IEEE Transactions on* , vol. 53, no. 1, pp. 553 - 559, Jan. 2005.
- [Mehdipour *et al.*, 2007] Mehdipour, A., K. Mohammadpour-Aghdam, and R. Farajidana, Complete Dispersion Analysis of Vivaldi Antenna for Ultra Wideband Applications, *Progress In Electromagnetics Research, PIER* 77, pp. 85 - 96, 2007.

- [Miller, 2003] Miller, L. E., Why UWB? A Review of Ultrawideband Technology, Report to the NETEX Project Office, DARPA from the Wireless Communication Technologies Group, National Institute of Standards and Technology, Gaithersburg, MD, April 2003.
- [Molisch, 2005] Molisch, A. F., Ultrawideband Propagation Channels-Theory, Measurement, and Modeling, IEEE Transactions on Vehicular Technology, vol. 54, no. 5, pp. 1528-1545, September 2005.
- [Muqaibel, 2003] Muqaibel, A. H., Characterization of Ultra Wideband Communication Channels, PhD Dissertation, Virginia Tech University, Blacksburg, Virginia, March 2003.
- [Parsons, 2000] Parsons, J. D., The Mobile Radio Propagation Channel, Second Edition, Wiley, November 2000.
- [Porcino and Hirt, 2003] Porcino, D., and W. Hirt, Ultra-wideband radio technology: Potential and challenges ahead, in IEEE Communications Magazine, vol. 41, no. 7, pp. 66 - 74, July 2003.
- [Pozar, 2003a] Pozar, D. M., Closed-form approximations for link loss in a UWB radio system using small antennas, IEEE Trans. Antennas Propag., vol. 51, no. 9, pp. 2346 - 2352, 2003.
- [Pozar, 2003b] Pozar, D. M., Waveform optimization for ultra wide band radio systems, IEEE Trans. Antennas Propag., vol. AP-31, no. 9, pp. 2335-2345, Sep. 2003.
- [Proakis, 1995] Proakis, J., Digital Communications. McGraw-Hill Series in Electrical and Computer Engineering. McGraw-Hill New York, 1995.
- [Promwong *et al.*, 2007] Promwong, S., P. Supanakoon, and J. Takada, Ground Reflection Transmission Loss Evaluation Scheme for Ultra Wideband Impulse Radio, ECTI Transactions on Electrical Eng., Electronics and Communications, vol. 5, no. 1, February 2007.

- [Qing *et al.*, 2006] Qing, X., Z. N. Chen, and M. Y. W. Chia, Characterization of ultrawideband antennas using transfer function, *Radio Science*, vol. 41, 2006.
- [Raspopovic and Thompson, 2005] Raspopovic, M., and C. Thompson. *Ultra-Wide Band Pulse Reflection: Exact Image Theory*. SoftCOM, Split, Croatia, September 2005.
- [Reed, 2005] Reed, J., *Introduction to Ultra Wideband Communication Systems*, Prentice Hall, ISBN: 0-13-148103-7, April 2005.
- [Salch and Valenzuela, 1987] Salch, A. M., and R. A. Valenzuela, A statistical model for Indoor multipath propagation, *IEEE journal on selected areas of communication, SAC-5*, vol. 128, no. 13, February 1987.
- [Sato and Kobayashi, 2004] Sato, S., and T. Kobayashi, Path-loss exponents of ultra wideband signals in line-of-sight environments, in *2004 IEEE International Symposium on Spread Spectrum Techniques and Applications*, Sydney, Australia, 30 Aug. - 2 Sept., 2004.
- [Schantz, 2005] Schantz, H. G., *The Art and Science of ultra wideband antennas*, Artech House, 2005.
- [Schantz, 2003] Schantz, H. G., Bottom fed planar elliptical UWB antennas, *Ultra Wideband Systems and Technologies, 2003 IEEE Conference on* , pp. 219 - 223, 16 - 19 Nov. 2003.
- [Schantz, 2001] Schantz, H. G., Electromagnetic Energy Around Hertzian Dipoles, *IEEE Antennas and Propagation Magazine*, vol. 43, no. 2, pp. 50-62, April 2001.
- [Schantz, 1997] Schantz, H. G., *Electromagnetic radiation made simple*, APS/AAPT Joint Meeting, Washington D.C., April 18 - 21, 1997.
- [Schantz, 1995] Schantz, H. G., *The energy flow and frequency spectrum around and electric and magnetic dipoles*, Ph.D. dissertation, University of Texas, Austin, Austin, TX, 1995.

- [Scheers *et al.*, 2000] Scheers, B., M. Acheroy, and A. V. Vorst, Time-domain simulation and characterization of TEM horns using a normalized impulse response, IEE Proc. Microwave Antennas Propag., vol. 47, pp. 463 - 468, 2000.
- [Schmitt, 1960] Schmitt, H. J., Transients in cylindrical antenna, IEE Monogr. Ser., 377E, Inst. of Electr. Eng., London, 1960.
- [Scholtz, 1993] Scholtz, R. A., Multiple Access with Time-Hopping Impulse Modulation, Proc.MILCOM, 11 - 14 October 1993.
- [Scholtz and Win, 1997] Scholtz, R. A., and M. Z. Win, Impulse Radio, in Wireless Communication TDMA versus CDMA, Ed. S. G. Glisic and P. A. Leppbnen, Kluwer Academic Publishers, Boston, pp. 245 - 267, 1997.
- [Shlivinski and Heyman, 1999] Shlivinski, A., and E. Heyman, Time domain near field analysis of short pulse antennas. Part II: Reactive energy and the antenna Q, IEEE Trans. Antennas and Propagat., vol. 47, pp. 280 - 286, Feb 1999.
- [Sibille, 2005] Sibille, A., A framework for analysis of antenna effects in UWB communications, Vehicular Technology Conference, IEEE 61st, vol. 1, pp. 48 - 52, 30 May - 1 June 2005.
- [Silva *et al.*, 2007] Silva, J. A. N., and M. L. R. Campos, Spectrally Efficient UWB Pulse Shaping With Application in Orthogonal PSM, IEEE Transactions on Communications, vol. 55, no. 2, February 2007.
- [Siwiak and Mckeown, 2004] Siwiak, K., and D. Mckeown, Ultra Wideband Radio technology, Wiley, 2004.
- [Siwiak *et al.*, 2003] Siwiak, K., H. Bertoni, and S. M. Yano, Relation between multipath and wave propagation attenuation, Electronics Letters, vol. 39, pp. 142 - 143, Jan. 2003.

- [Siwiak and Petroff, 2001] Siwiak, K., and A. Petroff, A Path Link Model for Ultra Wide Band Pulse Transmissions, IEEE VTS 53rd Vehicular Technology Conference, Proceedings Vol.2, pp.1173-1175, Spring 2001.
- [Sonwalkar, 1986] Sonwalkar, V. S., New signal analysis techniques and their applications to space physics, Ph.D. dissertation, Stanford University, 1986.
- [Sonwalkar *et al.*, 2006] Sonwalkar, V. S., A. Venkatasubramanian, J. Hawkins, B. Satavalekar, B. Johnson, and C. Mayer, Dependence of Multipath Propagation Effects on the UWB Pulse Characteristics, 2006 Waveform Diversity and Design Conference, Kauai Hawaii, 22 - 27 January 2006.
- [Sonwalkar *et al.*, 2007] Sonwalkar, V. S., A. Venkatasubramanian, B. A. Johnson, J. Hawkins, and B. Satavalekar, UWB pulse propagation over the ground, URSI EMTS 2007, Fairmont Chteau Laurier, Ottawa, ON, Canada, 26 - 28 July 2007.
- [Sorgel and Wiesbeck, 2005] Sorgel, W. and W. Wiesbeck, Influence of the antennas on the ultra-wideband transmission, EURASIP Journal on Applied Signal Proccessing, vol. 1, , pp. 296 - 305, Jan. 2005.
- [Sullivan, 2000] Sullivan, D., Electromagnetic Simulation Using the FDTD Method, IEEE Press and John Wiley and Sons, Inc., 2000.
- [Taflove, 1995] Taflove, A., Computational Electrodynamics: The Finite-Difference Time-Domain Method, Boston, MA: Artech House, 1995.
- [Taha and Chugg, 2002] Taha, A., and K. M. Chugg, On Designing the Optimal Template Waveform for UWB Impulse Radio in the Presence of Multipath, IEEE Conference on Ultra Wideband Systems and Technologies, 2002.
- [Tarique *et al.*, 2006] Tarique, Z., W. Q. Malik, and D. J. Edwards, Bandwidth requirements for accurate detection of direct path in multipath environment, IEE Electron. Lett., vol. 42, no. 2, pp. 100 - 102, Jan. 2006.

- [Taylor, 2000] Taylor J. D., Ultra-Wideband Radar Technology, Boca Raton, FL, CRC Press, 2000.
- [Tiuri *et al.*, 1984] Tiuri, M., A. Sihvola, E. Nyfors, M. Hallikaiken, The Complex Dielectric Constant of Snow at Microwave Frequencies, IEEE Journal of Oceanic Engineering, vol. 9, no. 5 , pp. 377-382, Dec. 1984.
- [Venkatasubramanian, 2007] Venkatasubramanian, A., A MATLAB-based simulation model of a Ultra Wideband (UWB) communication system, Internal report, Waves Lab, Department of Electrical and Computer Engineering, December 2007.
- [Venkatasubramanian, 2003] Venkatasubramanian, A., Numerical modeling of electromagnetic wave propagation in a hallway, M.S. thesis, University of Alaska Fairbanks, August 2003.
- [Venkatasubramanian *et al.*, 2007] Venkatasubramanian, A., V. S. Sonwalkar, B. A. Johnson, J. Hawkins UWB dipole radiation: measurements and simulation, URSI EMTS 2007, Fairmont Chateau Laurier, Ottawa, ON, Canada, 26 - 28 July 2007.
- [Wang *et al.*, 2005] Wang, T., Z. N. Chen and K., Chen, Effect of selecting antenna and template on BER performance in pulsed UWB wireless communication systems, Antenna Technology: Small Antennas and Novel Metamaterials, pp. 446 - 449, 7 - 9 March 2005.
- [Wang *et al.*, 2003] Wang, T., Y. Wang, K. Chen, Analyzing the interference power of narrowband jamming signal on UWB system, in Proc. IEEE 14th Sympos. on Personal Indoor Mobile and Radio Commun., vol. 1, p.p. 612 - 615, Beijing, China, Sep. 2003.
- [Win and Scholtz, 2000] Win, M. Z., and R. A. Scholtz, Ultra -wide bandwidth time-hopping spread-spectrum impulse radio for wireless multiple -access communications, IEEE Trans. Comm., vol. 48, pp. 679 - 691, April 2000.

- [Yang *et al.*, 2007] Yang, W., N. Zhang, Q. Zhang, and J. Ye, A 2-Ray Path Loss Model for I-UWB Signals Transmission, International Conference on Wireless Communications, Networking and Mobile Computing, 2007, 21 - 25 Sept. 2007.
- [Yee, 1966] Yee, K. S., Numerical solution of initial boundary value problems involving Maxwells equations in isotropic media, IEEE Trans. Antennas Propagat., vol. 14, pp. 302 - 307, Mar. 1966.
- [Zhang and Brown, 2006] Zhang, Y., and A. K. Brown, The discone antenna in a BPSK direct-sequence indoor UWB communication system, Microwave Theory and Techniques, IEEE Transactions on , vol. 54, no. 4, pp. 1675 - 1680, June 2006.
- [Zhang and Huang, 2002] Zhang, J. T., and Y. Huang, Indoor channel characteristics comparison for the same building with different dielectric parameters, Proceedings of the IEEE International Conference on Communications, vol. 2, pp. 916 - 920, 2002.

Appendix A Noise Calculation in Experiments

A.1 Noise Floor of the Agilent E8358A Vector Network Analyzer

Agilent defines the test port noise floor as the “total average (rms) noise power calculated as the mean value of a linear magnitude trace expressed in dBm.” The manufacturer specifications for the noise of the E8358A VNA with the IF bandwidth equal to 1 kHz and the source power equal to +10 dBm are shown in Table A.1. With the analyzer test port cables on both input ports terminated with calibrated loads, source power set to 10 dBm and IF bandwidth set to 1 kHz, the measured noise floor was generally within specifications over the entire instrument range, as shown in Figure A.1. The noise floor decreased by 10 to 15 dB when the analyzer averaged up to 10 frequency scans (grey curve in Figure A.1). Beyond 10 scans, there was < 1 dB improvement in the noise floor.

A.2 Tektronix TDS6804B Digital Signal Oscilloscope

A.2.1 Vertical Resolution and Quantization Noise

The 8-bit Analog-to-Digital Converters (ADCs) quantize the DSO input signal amplitude into $2^8 = 256$ discrete levels, providing a maximum resolution of 0.39% of the full scale

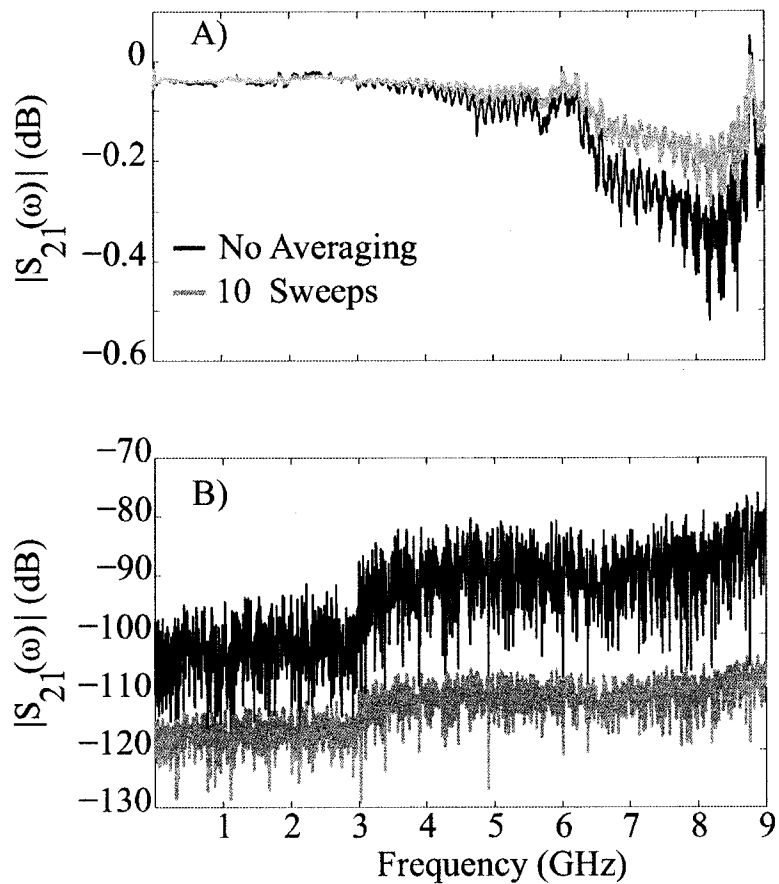


Figure A.1. VNA noise floor with both analyzer cables terminated with 50 Ω loads and calibrated shorts.

Table A.1. Agilent E8356A VNA noise power level and noise floor.

Frequency Range	Noise Power Level with 1 KHz IF bandwidth (dBm)	S-parameter Noise Floor with 10 dBm Source (dBm)
300 kHz to 25 MHz	-95	-105
25 MHz to 3 GHz	-98	-108
3 GHz to 9 GHz	-88	-98

display. This corresponds to a dynamic range of 48 dB. The dynamic range of an oscilloscope refers to how well the instrument can detect small signals in the presence of large signals and is expressed in decibels (dB). It is limited by the quantization error and all other noise sources such as background noise, distortion, spurious signals, etc. The equation for computing the dynamic range is

$$\text{Dynamicrange} = 20 \log \frac{V_{max}}{V_{min}} \quad (\text{A.1})$$

The noise floor characteristics of the DSO was measured by grounding one of the input channels and collecting 32 million samples with no input signal applied. Figure A.2 shows the noise floor waveform captured with the vertical sensitivity set to 10 mV/division. The noise statistics computed by the DSO are shown at the bottom of the figure. The peak-to-peak noise level is 3.5 mV, which is 4.4% of the full-scale deflection of 80 mV. This corresponds to approximately 11 discrete levels of the quantized data. The maximum achievable signal-to-noise ratio (SNR) occurs when the input signal spans the full scale of the display. This corresponds to a maximum SNR of 27 dB for the peak level of the waveform.

This noise floor evaluation was repeated for each vertical sensitivity value of the DSO. The rms and peak-to-peak noise voltages scale directly with the vertical sensitivity setting. This is because the noise is dominated by the quantization noise of the ADCs, which scales directly with the full-scale range of the display. The one exception is the most sensitive set-

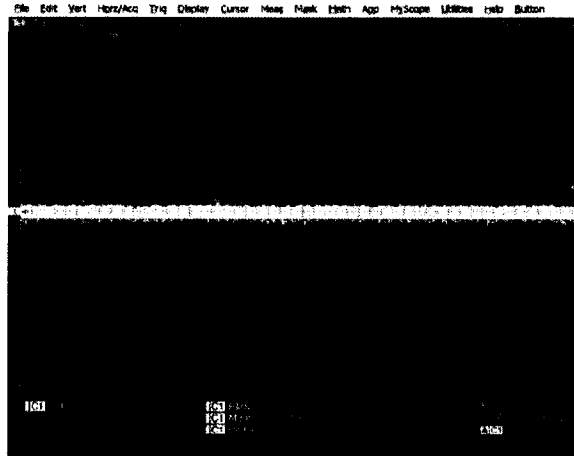


Figure A.2. DSO Noise waveform and statistics for vertical sensitivity equal to 10 mV/div.

ting at 5 mV/division, which the DSO accomplishes by digitally zooming the data collected at the 10 mV/division sensitivity. This effectively doubles the quantization noise voltage for this vertical sensitivity. This quadruples the noise power at this lowest setting, which reduces the maximum achievable SNR by 6 dB.

The noise floor of the DSO may be quantified in terms of the thermal noise referenced to the input for a signal source of the same temperature and bandwidth. The thermal noise power is given by

$$N_{thermal} = kT_{amb}B \quad \text{(A.2)}$$

where $k = 1.38 \times 10^{-23}$ J/K, T_{amb} (K) is the ambient room temperature and B (GHz) is the DSO bandwidth. For a system at room temperature ($T = 300$ K), and a bandwidth of 8 GHz, the thermal noise power is -75 dBm. The DSO noise power may be computed from

$$N_{DSO} = \frac{V_{rms}^2}{Z_0} \quad \text{(A.3)}$$

where $Z_0 = 50 \Omega$. The noise performance of the DSO may then be specified as either a Noise Figure equal to the ratio of N_{DSO} to $N_{thermal}$ in dB, or as an equivalent noise temperature

Table A.2. Noise Performance of Tektronix TDS6804B DSO.

Vertical Sensitivity (mV/Div)	RMS Noise Voltage (mV)	RMS Noise Power (dBm)	DSO Noise Figure (dB)	DSO Noise Temperature (K)
5	0.69	-50.3	24.5	84,000
10	0.75	-49.4	25.4	103,000
20	1.25	-45.1	29.7	281,000
50	2.77	-38.1	36.7	1,390,000
100	6.83	-30.3	44.5	8,438,000
500	12.24	-18.3	56.5	133,406,000
1000	53.69	-12.4	62.4	522,213,000

that would produce thermal noise power equal to the system noise power. These metrics of noise performance are summarized for each DSO vertical sensitivity in Table A.2.

Although the DSO system noise power increases with the square of the vertical sensitivity, the maximum achievable SNR is nearly constant at 30 dB, as shown in Table A.3. As previously noted, the one exception is the 5 mV/div sensitivity which relies on the DSO digital zoom rather than actually re-scaling the signal applied to the ADC.

Table A.3. Maximum Signal-to-Noise Ratio for Tektronix TDS6804B DSO.

Vertical Sensitivity (mV/Div)	Peak-to-Peak Noise Voltage (mV)	Maximum Signal to Noise ratio (dB)
5	3.5	21.2
10	3.5	27.2
20	5.6	29.1
50	13.1	29.7
100	43.6	25.3
500	129.8	28.4
1000	306.1	28.3

A.2.2 Sensitivity of the DSO

The shape of a received UWB waveform is a function of the source waveform, the transmitting antenna, the receiving antenna, and the propagation channel. In the NLOS project, we are evaluating the feasibility of utilizing UWB waveforms for real-time channel sounding by comparing the received waveform with the transmitted waveform to deduce the characteristics of the channel. The ability to accurately capture the waveform of low amplitude UWB signals is therefore crucial to the NLOS project. Since we are trying to extract channel sounding information from the received waveform, a measurement with the highest possible SNR is desirable. As noted in Table A.3, the maximum achievable SNR for the 5 mV/division setting of vertical sensitivity is approximately 6 dB less than the other settings, and is therefore not considered farther. The peak signal amplitude of the UWB waveform must be as close as possible to full scale on the DSO display to approach the maximum achievable SNR of ~ 27 dB. The 10 mV/division setting is the best choice for capturing the lowest amplitude UWB signals, where the optimum peak-to-peak amplitude is 80 mV. This corresponds to a peak received power of $32 \mu\text{W}$ (-15 dBm).

The sensitivity of the DSO to low amplitude signals may be improved by amplifying the received signal with a Low Noise Amplifier (LNA) to boost the signal amplitude relative to the noise floor of the DSO. Table A.3 shows that the RMS noise power associated with the 10 mV/division setting is -49 dBm, while the thermal noise floor is -75 dBm for an 8 GHz system bandwidth. The input signal may be amplified by an LNA without adversely affecting the SNR of the DSO measurement, provided that the amplified thermal noise power plus the noise contributed by the LNA remains small compared to the DSO noise floor. If the LNA gain is equal to the difference between these power levels (i.e., 26 dB), and the LNA does not contribute additional noise ($\text{NF} = 0$ dB), then the amplified noise equals the DSO noise floor and the maximum achievable SNR is reduced by 3 dB. The maximum useful amount of LNA gain is approximately 26 dB which would reduce the required peak input power level to approximately 80 nW (-41 dBm) for measurements with optimum SNR.

The Miteq AFS3-0200600-15-LN LNA has a nominal gain of 26 dB (measured gain of

30 dB) and a Noise Figure of 1.6 dB over the frequencies of interest. The corresponding effective noise temperature for this LNA is $T_{LNA} = 135$ K. The system noise temperature for the complete system at room temperature and the DSO vertical sensitivity set at 10 mV/division is:

$$\begin{aligned}
 T_{SYS} &= T_{ANT} + T_{LNA} + \frac{T_{DSO}}{G_{LNA}} && \text{(A.4)} \\
 &= 300 + 135 + \frac{103000}{1000} \\
 &= 538K
 \end{aligned}$$

which corresponds to a system noise figure of 2.5 dB. To achieve measurements with optimum SNR, a small amount of attenuation may be added to keep the peak amplitude of the input waveform near full scale of the DSO display to prevent switching to the next range of vertical sensitivity with the corresponding increase in the noise floor.

A.3 Anechoic Chamber Calibration Measurements

Figure A.3A shows a picture of the test setup for the free space anechoic chamber calibration measurements. A pair of Time Domain BroadSpec P200 UWB antennas (Figure 2.3B) are connected to the two ports of a VNA which measures the scattering parameters at 1601 equally spaced points in the 300 kHz to 9 GHz frequency range with a transmit power of +10 dBm. Also shown in the figure is the coordinate system used for this measurement. The z -axis is aligned along the local vertical and the x - and y -axis are along the breadth and length of the chamber. The receiving antenna is moved away from the transmitting antenna along the y -axis. The whole experimental setup is placed approximately equidistant from the side walls (walls with x -axis normal to it) of the chamber. Figures A.3B and A.3C show that, in the 2.5 GHz to 8 GHz frequency range (PulsON 200 antenna transmission bandwidth), the deviation from free space is < 0.5 dB for separation distances of 2 to 2.5

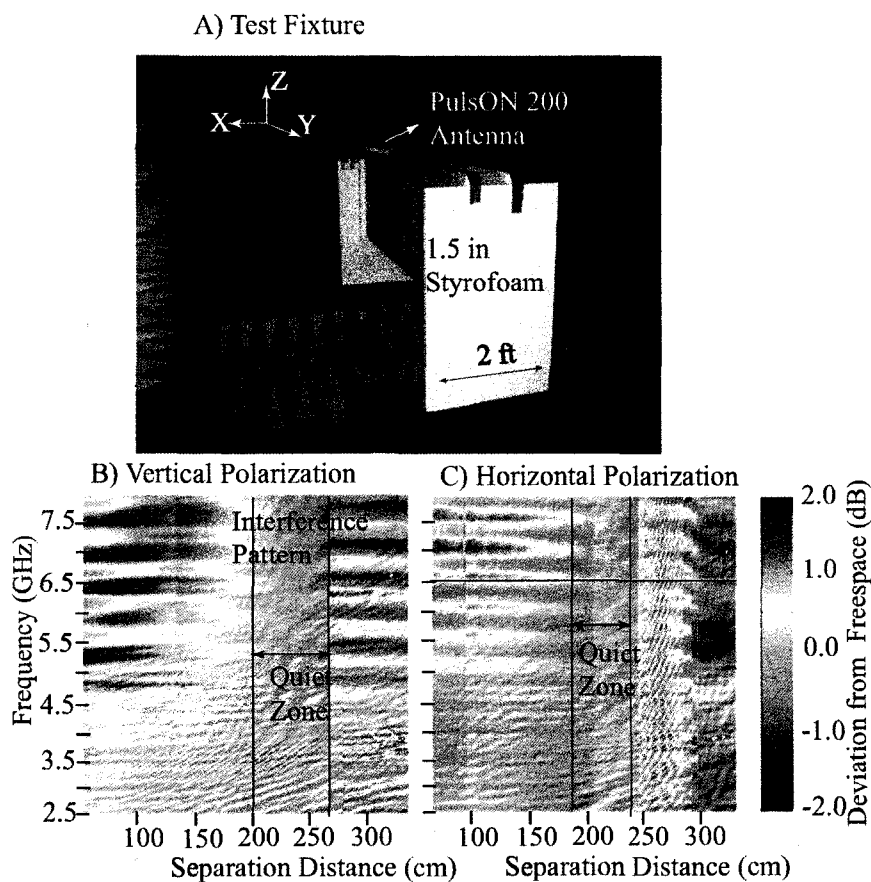


Figure A.3. Free space measurements to calibrate anechoic chamber using Time Domain PulsON200TM antenna. (A) Test fixture fabricated from 1.5-inch Styrofoam sheets for positioning the receiving antenna at varying distances from the transmitting antenna. The transmitting antenna was located 60 cm from the tips of the cones on the transmit wall and the receiving antenna position was varied from 60 cm to 325 cm from the transmitting antenna. (B) 3D contour of deviation from the free space spreading loss versus frequency and distance for horizontal polarization of the transmitting and the receiving antenna. The antenna position was incremented in 1 cm steps and S₂₁ was measured from 300 kHz to 9 GHz at frequency each step. (C) 3D contour of deviation from the free space spreading loss versus frequency and distance for vertical polarization of the transmitting and receiving antenna.

m between the transmitting and the receiving antenna.

A.4 Signal Processing Algorithms

The signal processing techniques described in this section are used to extract antenna and channel characteristics from laboratory measurements. Antennas and propagation channels may be characterized by a transfer function in the frequency domain, or equivalently by an impulse response in the time domain. Frequency domain techniques using measurements performed with a Vector Network Analyzer (VNA) are described in section A.3.1. Time domain techniques using measurements performed with a UWB source and a Digital Storage Oscilloscope (DSO) are described in section A.3.2.

A.4.1 Frequency Domain De-convolution of the Antenna Impulse Response

The transfer function of an antenna is defined as a function of the operating radian frequency ω , the orientation of the antenna in the vertical (θ) and the horizontal (ϕ) plane, and the separation distance, R , between the transmitting and the receiving antenna. The transmitting antenna transfer function, $H_t(\omega, \theta_t, \phi_t)$ is defined as the ratio of the radiated electric field to the input voltage applied to the antenna terminals. The radiated electric field is normalized to the magnitude and phase of the electric field at the location of the receiving antenna in the transmitting antenna reference frame (Figure 2.1A). Hence $H_t(\omega, \theta_t, \phi_t)$ is dimensionless. The receiving antenna transfer function $H_r(\omega, \theta_r, \phi_r)$ is defined as the output voltage at the antenna terminals divided by the electric field incident on the antenna. The direction of arrival of the incident electric field in the receiving antenna coordinate frame (Figure 2.1B) is given by (θ_r, ϕ_r) . $H_r(\omega, \theta_r, \phi_r)$ has dimensions of meters.

The transmitting antenna transfer function is calculated as

$$H_t(\omega, \theta_t, \phi_t) = \sqrt{\frac{2S_{21}}{(1 + S_{11})(1 - S_{22})} \frac{j\omega}{2\pi c} R e^{jkR}} \quad \text{(A.5)}$$

where $S_{11}(\omega)$ is the reflection coefficient of the antenna connected to port 1 when port 2 is terminated in a matched load, $S_{22}(\omega)$ is the reflection coefficient of the antenna connected to port 2 when port 1 is terminated in a matched load, $S_{21}(\omega)$ is the transmission coefficient from the antenna connected to port 1 to the antenna connected to port 2, and $k = \omega/c$ is the wave number.

The receiving antenna transfer function is calculated as [Qing *et al.*, 2006]

$$H_r(\omega, \theta_r, \phi_r) = \sqrt{\frac{2S_{21}}{(1+S_{11})(1-S_{22})} \frac{2\pi c}{j\omega} R e^{jkR}} \quad (\text{A.6})$$

It should be noted that the scattering parameters are complex quantities and hence their measured phases need to be unwrapped using the `unwrap.m` function in MATLAB. This should be done before the calculation of the transmitting and the receiving antenna transfer function using Equations A.5 and A.6. Otherwise, the results will be nonphysical.

The assumptions in this experimental procedure are:

1. The two antennas are an identical, matched pair. This was achieved by comparing the S11 measurement at each frequency point between 300 kHz to 9 GHz and picking two prototype antennas with average difference < 1 dB.
2. The two antennas are in the far field of each other and identically oriented that is $\theta_t = \theta_r = \theta$ and $\phi_t = \phi_r = \phi$.
3. The transmitting antenna transfer function is related to the receiving antenna transfer function as [Scheers *et al.*, 2000]

$$H_t(\omega, \theta_t, \phi_t) = \frac{j\omega}{2\pi c} H_r(\omega, \theta_r, \phi_r) \quad (\text{A.7})$$

where c is the speed of light in vacuum and $j = -1$.

4. The transmitting and the receiving antenna impedance are equal and matched to the characteristic impedance of the transmission line in the frequency range of interest.

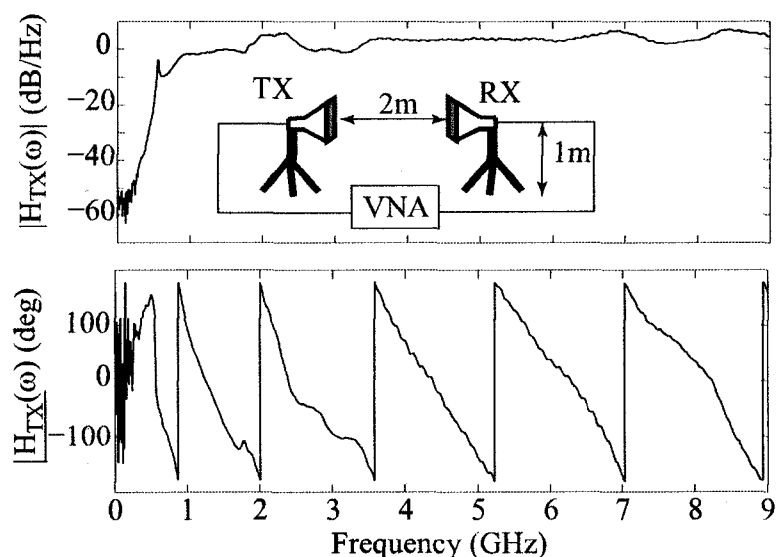


Figure A.4. **Transmitting antenna transfer function computed for the horn antenna.** The top panel shows the amplitude and the bottom panel shows the phase of the transmitting antenna transfer function calculated from the S_{21} measured for a pair of horn antennas separated by 2 m in the anechoic chamber (shown as inset in Figure).

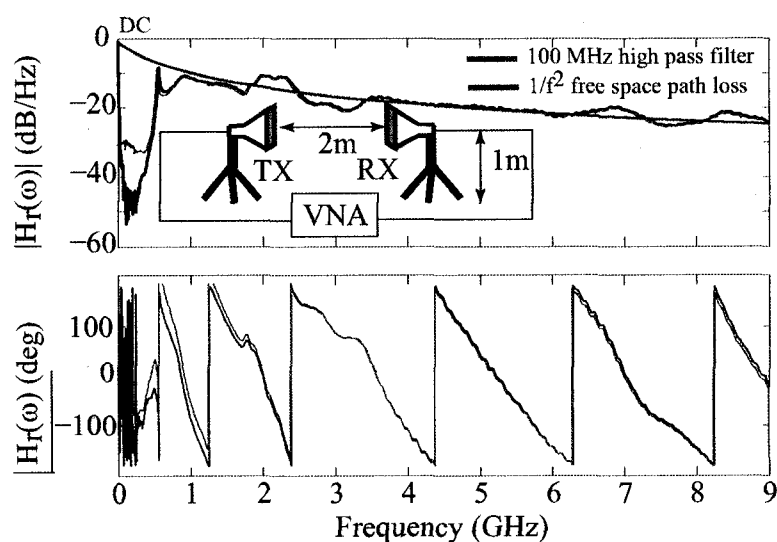


Figure A.5. **Receiving antenna transfer function for the horn antenna.** The top panel shows the amplitude and the bottom panel shows the phase of the receiving antenna transfer function calculated from the S_{21} measured for a pair of horn antennas separated by 2 m in the anechoic chamber (shown as inset in Figure). The blue curve shows the free space $1/f^2$ path loss which explains the negative slope of the transfer function.

To validate the above procedure, the transmitting and the receiving antenna transfer function for a pair of identical, commercial horn antennas (shown in Figure 2.3A) is measured. The horn antennas are separated by 2m in the anechoic chamber with their broadside directions facing one another. The antennas are held on a tripod at a height of 1 m from the floor of the chamber (shown as inset in Figure A.4). The measured transmitting antenna transfer function, shown as a black curve in Figure A.4, indicates that the horn antenna has a flat frequency spectrum in the 1 to 9 GHz frequency range. The receiving antenna transfer function, shown as a black curve in Figure A.5, has a non zero DC component and a $1/f^2$ slope owing to the free space path loss (shown as a blue curve). The non-zero DC component is filtered out using a 100 MHz high pass filter (shown as red curve).

The transfer functions shown in Figures A.4 and A.5, are measured for 1601 positive frequency points spaced every 5.6 MHz. The inverse fourier transform of this transfer function yields a discrete time analytical signal [Iverson, 1991]. The real part of this signal yields the time domain impulse response, $h(t)$, for each pair of elevation and azimuth angles [Sorgel and Wicsbeck, 2005]. The measured impulse response has a time resolution of 284.6 ps. The time resolution can be improved to 5 ps by zero padding the measured transfer function from 9 GHz to 200 GHz. The impulse response is further preprocessed by low pass filtering the high frequency oscillations due to the sharp cut off in the measurement at 9 GHz.

A.4.2 Time Domain De-convolution of the Antenna Impulse Response

An input signal $x(t)$ applied to a band-limited system with impulse response $h(t)$ yields an output signal $y(t)$ related to the input as the convolution of $h(t)$ and $x(t)$:

$$y(t) = h(t) * x(t) \quad \text{A.8}$$

A received signal waveform captured by the DSO in the anechoic chamber is the convolution of the transmitter waveform with the impulse responses for the transmitting antenna, the

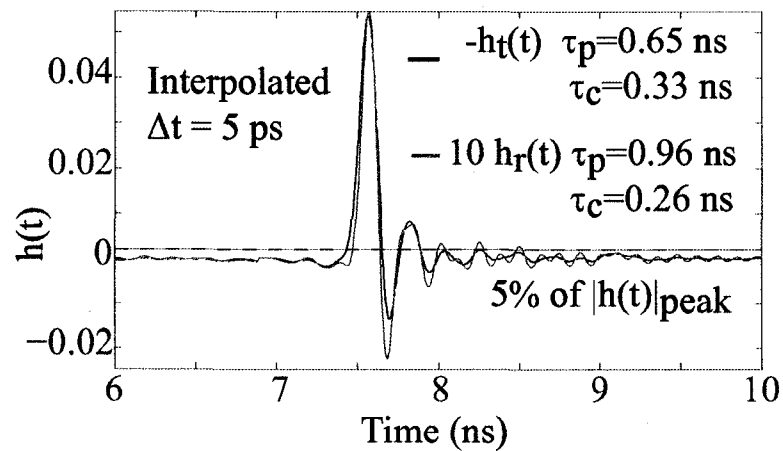


Figure A.6. **Transmitting and receiving band-limited impulse response of the horn antenna.** The black curve shows the transmitting antenna impulse response and the red curve shows the receiving antenna response. There is additional high frequency ringing (~ 9 GHz) in the measured impulse responses owing to the sharp cut off of the VNA at 9 GHz.

propagation channel, and the receiving antenna:

$$y(t) = h_{TX,ant}(t) * h_{channel} * h_{RX,ant}(t) * x(t) \quad \text{A.9}$$

To characterize an antenna with time domain measurements, the ideal input signal would be a true impulse with infinite amplitude and zero width. Our closest available approximation to this ideal input signal is the band-limited impulse from the MSSSI impulse source (shown in Figure 2.2C). This signal is transmitted between two antennas separated by 2 meters in the anechoic chamber. The received waveform captured with the DSO is a function of both the input waveform and the system impulse response.

The waveform is captured by the DSO at the minimum sampling period of 50 picoseconds per sample to provide the greatest possible resolution in the time domain. The effects of the non-ideal input signal must be removed from the DSO data to extract the band-limited impulse response of the system ($h_{TX}(t) * h_{CH} * h_{RX}(t)$). De-convolution does not provide a unique solution to the impulse response of the system. We illustrate this by applying two iterative de-convolution algorithms to the DSO waveform received through the two Sunol

horn antennas.

The Van-Cittert algorithm described in Bennis and Riad [1992] is an iterative time domain technique that approximates $h_i(t)$ by performing successive convolutions with $x(t)$ and then calculating an error term that is the difference between the actual output and the convolution array $[h_i(t)*x(t)]$. The error term is iteratively added to the previous estimated impulse response $h_{i-1}(t)$ to yield $h_i(t)$. The sensor-CLEAN algorithm de-convolves the system impulse response by iteratively subtracting the peaks in the cross correlation array of $x(t)$ and $y(t)$ from the auto correlation of the input signal $x(t)$. This yields the strongest energy peaks in the impulse response $h_i(t)$ at each time step.

The sensor-CLEAN algorithm initiates the impulse response at $h_0(t) = 0$, whereas the Van-Cittert algorithm initiates the impulse response at $h_0(t) = y(t)$. Therefore, the sensor-CLEAN algorithm requires a greater number of iterations but achieves greater accuracy and is less susceptible to noise in the signal. The Van-Cittert algorithm initiates the estimated impulse response to the output signal, so the impulse response is more susceptible to noise in the signal, which increases due to additions involved in the convolution operation. The sensor-CLEAN algorithm is more robust to noise because there is a constant reduction (subtraction) in the signal amplitude and noise level. However, the sensor-CLEAN can give false noise peaks in the impulse response. A detailed discussion of the methods is given in [Cramer *et al.*, 1999].

To validate the approach, the received voltage waveform for a pair of horn antennas separated by 2 m in the anechoic chamber is shown in Figure A.7A as a red curve. The MSSSI source waveform is shown as a black curve. Figure A.7B shows a comparison of the broadside impulse response of the transmitting horn antenna de-convolved from the time domain measurement using the sensor-CLEAN (red curve) and the Van-Cittert (blue curve) algorithms.

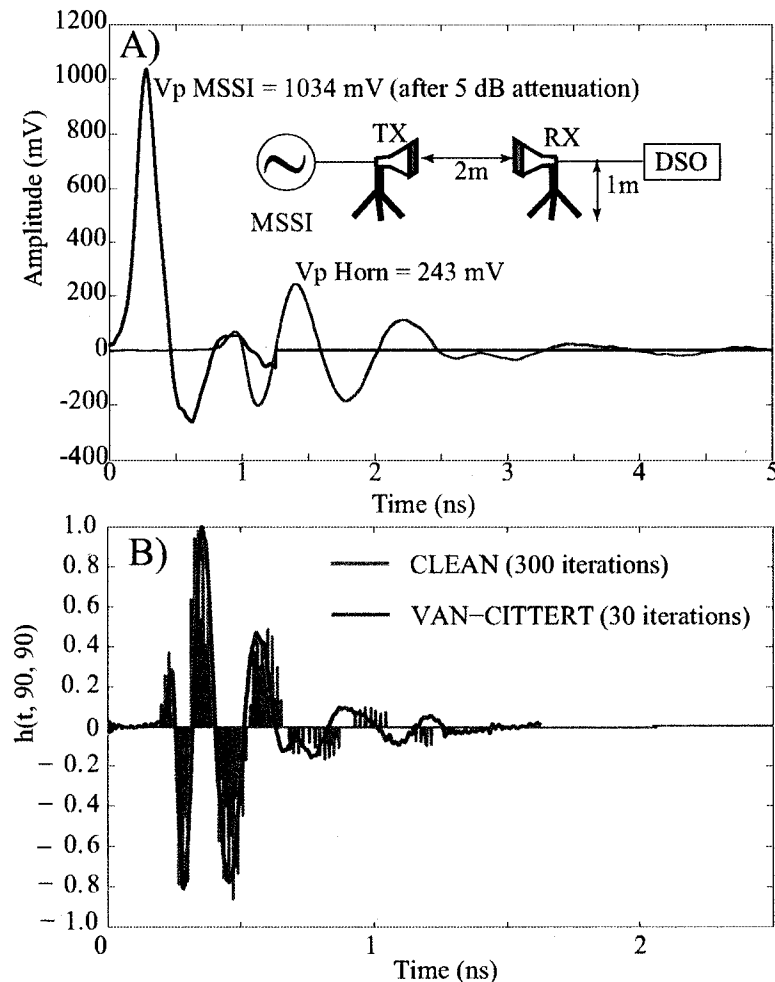


Figure A.7. **Time domain measurement of the band-limited impulse response of a pair of horn antennas.** The top panel shows the two antennas separated by a distance of 2 m in the anechoic chamber. One antenna is connected to a MSSI source (black curve) that generates a $\sim 10 \text{ V}$ peak amplitude waveform with a duration of 0.7 ns. The received voltage waveform (red curve) at the terminals of a identical antenna is measured using a TDS6804B high-speed digital storage oscilloscope (DSO) with a time resolution of 50 ps. The bottom panel shows the time domain band-limited impulse response computed using the sensor-CLEAN [Cramer *et al.*, 1999] and the Van-Citteret [Bennia and Riad, 1992] iterative de-convolution algorithms, shown as red and blue curves respectively.

Appendix B Data Processing Algorithms

B.1 Calculation of the Pulse Width τ_p and the Pulse Cycle Time

τ_c

There are many ways to define a pulse width [Bracewell, 1999]. For a single pulse with bell-shaped amplitude, or a modulated pulse with bell-shaped envelope, it is convenient to define the pulse width as the width where the peak amplitude of the pulse is down by 3 dB in log scale or 0.7 in linear scale. For a more general shape of the pulse or the envelope, it is more convenient to define pulse width as the duration of the pulse that contains 90% of the total energy [DiBenedetto and Giancola, 2004]. In this approach the energy in the input pulse is measured and the duration of the pulse that contains a fraction (0.9 or 90%) of the original energy is calculated. Figure B.1A shows the commercial Multi Spectral Solutions Inc. (MSSI) UWB pulse (solid black curve) measured by directly connecting it to an oscilloscope through a -5 dB attenuator. Also shown is the pulse duration containing 90% of the signal energy. The calculated pulse width τ_p is 0.72 ns. The half cycle time $\tau_c/2$ of the pulse is measured as twice the number of zero crossings in the measured τ_p and is 0.38 ns. The limitation of this approach is that the energy contained in the pulse depends on the total duration of the signal containing the pulse and the amount of noise in the signal.

This decides the fraction of the energy that will be used to calculate τ_p and τ_c . So when the input energy is spread over multiple pulses then a large error ($> 200\%$) is observed in the calculated τ_p and τ_c values. An alternative approach is proposed for the determination of the pulse width of the received UWB pulse when there are multiple pulses.

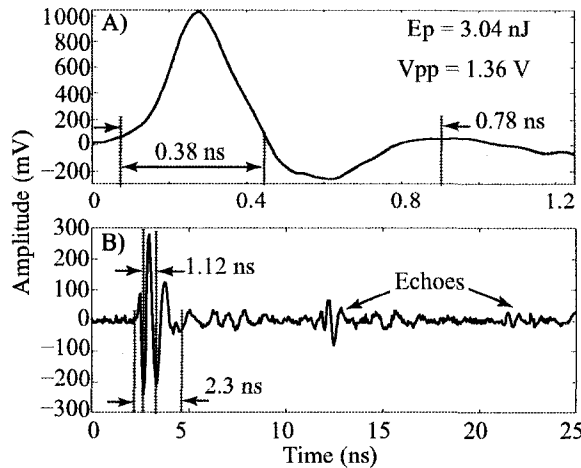


Figure B.1. **Determination of duration and cycle time of the input pulse.** (A) The duration τ_p and cycle time τ_c of the MSSSI source directly connected to an oscilloscope. The duration is measured as containing 90% of the pulse energy. (B) The duration τ_p and cycle time τ_c of the MSSSI source radiated and received by a pair of horn antennas separated by 2 m in the anechoic chamber. The duration is measured using the pulse overlap method.

The proposed approach to calculate pulse width when the received pulse has an overlap of pulses arriving from two or more directions, as is the case in this thesis. This method is termed pulse overlap method. The pulse width is defined as twice the time delay at which the interference of the first and second arriving pulses will give a peak amplitude larger than the peak amplitude of the first arriving pulse. So to calculate the duration of the input pulse, an inverted copy of the pulse is added to the input pulse with a delay greater than at least twice the pulse duration to avoid any pulse overlap. The total pulse has a peak amplitude which is still same as the peak amplitude of the first arriving pulse within noise fluctuations. The delay of the inverted copy of the original pulse is reduced till the absolute peak amplitude total pulse is greater than or lesser than the peak amplitude of the first pulse by a threshold. The threshold depends on the noise and the envelope of the

pulse. The calculated delay is half the duration of the pulse τ_p . The delay of the inverted copy is further reduced till an absolute maximum in the peak amplitude of the total pulse is calculated. This delay is the duration of one-half cycle, $\tau_c/2$, of the pulse. The inherent assumption in this approach is that the two pulses have the same cycle time, τ_c , envelope, and start overlapping when the reflection coefficient is approximately -1 . Within these assumptions it is possible to define pulse width, τ_p , which is independent of the reflecting surface properties and the geometry of the propagation environment. Figure B.1B shows the MSSSI source radiated and received by a pair of commercial horn antennas (section 2.2.1, Figure 2.3A) separated by 2 m in the anechoic chamber. The received voltage pulse is measured by a oscilloscope (discussed in Appendix A). The black curve shows multiple copies of the first arriving pulse due to reflections in the connecting cables. So the energy in the first pulse is a fraction of the total energy contained in the signal and a threshold of 90% provides a pulse width of 22.8 ns. The τ_p and τ_c calculated by the second method is 2.3 ns and 1.15 ns. The threshold set for this calculation is that the difference in the absolute peak amplitude of the measured pulse and the total pulse containing the measured pulse and its inverted replica is greater than 1/4th the peak amplitude of the measured pulse.

Note that in the second method, the defined pulse width τ_p will always be a multiple of the half-cycle duration $\tau_c/2$. This implies that an adaptive receiver design can change pulse properties in discrete steps of $\tau_c/2$.

B.2 Calculation of the Bandwidth B and the Center Frequency f_c

The bandwidth B and the center frequency f_c of an input pulse are frequency domain properties of the time domain pulse. So the input pulse $x(t)$ is Fourier transformed to the frequency domain $X(f)$. The energy spectrum of the pulse is calculated as

$$ESD = |X(f)|^2/df^2 \quad \text{(B.1)}$$

where df is the frequency resolution determined as the ratio of the sampling frequency to the length of the pulse. The bandwidth occupied by the pulse is then defined as the frequency separation between the two points which are below intersected by the straight line drawn at the threshold. The two points define the lower (f_l) and the upper (f_h) cut off frequency of the pulse. The center frequency f_c is defined as the geometric mean of the lower and the upper cut off frequencies, so $f_c = \sqrt{f_l \cdot f_h}$. Note that this method depends on the sampling frequency and the noise contained in the measured pulse. A noisy spectrum of the pulse may have many points that cross a threshold line. But all these points are localized to an average frequency with a spread which decides the error in the measurement. Figure B.2 shows the frequency spectrum of the pulse received by a pair of PulsON 200 systems separated by 1 m in the Taku parking lot.

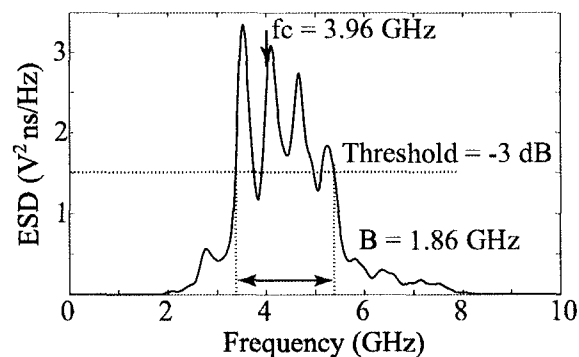


Figure B.2. **Determination of bandwidth B and center frequency f_c .** A pair of PulsON 200 systems are separated by 1 m in the Taku parking lot and the received pulse is fourier transformed to calculate the B and f_c of the pulse.

B.3 Algorithm to Calculate the Breakpoint Distances and the Location of Maxima and Minima in the RSS data

The breakpoint distances and the location of maxima and the minima in the measured RSS (discussed in sections 3.2.1 and 3.2.2) are calculated using an algorithm detailed in this section. The flow diagram of the algorithm is shown Figure ???. The data is partitioned into

two arrays $RSS_1(d)$ and $RSS_2(d)$. The first array, $RSS_1(d)$, is from the first data point up to d_2 and the second segment, $RSS_2(d)$, is from d_2 to the last point. This procedure requires knowledge of d_2 which is calculated using the formula $d_2 = 4h_1h_2f_c/c$. Using the first array, $RSS_1(d)$, the best fit to $1/d^2$ is calculated. Then calculated linear fit line is subtracted from $RSS_1(d)$. The difference is a roughly zero mean data. The low frequency fluctuations in the data is removed by using the `polyfit.m` function in MATLAB. The variance of the resultant noisy data is calculated using the `variance.m` function. A `peakdetect.m` function measure the location of the maxima and minima in the resultant noisy data. To accurately measure d_2 from the data, the second array $RSS_2(d)$ is linearly fit to the $1/d^4$ curve. The location of minimum variance between the linear fit curve and the measured data provides the location of d_2 . The location of d_1 is calculated from the formula $d_1 = 4h_1h_2B/c$.

Figure B.4A shows the measured received signal strength as a function of separation distance for the transmitter and receiver at a height of 0.5 m above the ground in the Taku parking lot (same as Figure 3.8). The blue line shows the $1/d^2$ curve and the red line shows the $1/d^4$ curve. Also shown in the figure is the calculated location of the first breakpoint d_1 and the measured location of the second breakpoint d_2 . Figure B.4B shows the difference between the $1/d^2$ linear fit line and the measured data as a black curve and the filtered data as a red curve. Also shown are the maxima and minima as black and red squares, respectively. Figure B.4C shows the variance of the $1/d^2$ and $1/d^4$ fit to the data shown as blue and red curve, respectively. The same procedure is repeated for the other transmitter heights shown in Figure 3.9.

B.4 Calculation of the relative permittivity of the ground and the thickness of snow layer on the ground using UWB measurements

B.4.1 Mathematical Formulation

The thickness and the relative permittivity, ϵ_r , of snow is calculated from the measured UWB pulse captured by a pair of Time Domain PulsON 200TM UWB transceiver systems

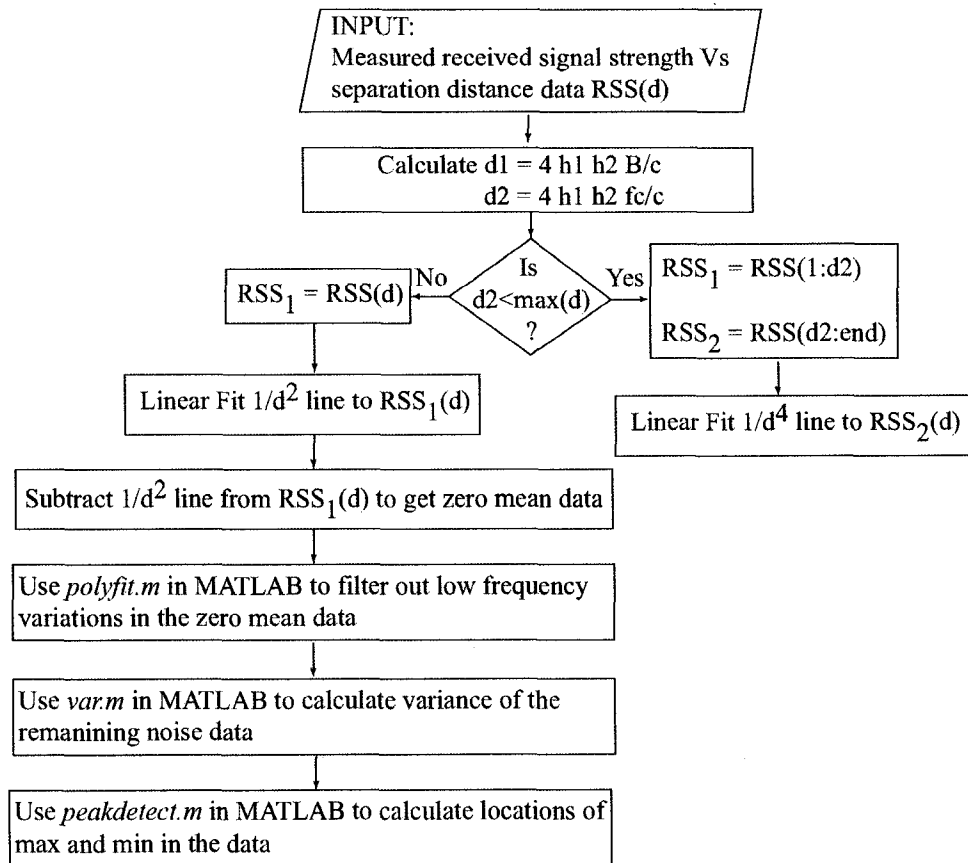


Figure B.3. Flow diagram for the algorithm to determine breakpoint distances and maxima and minima in the received signal strength data.

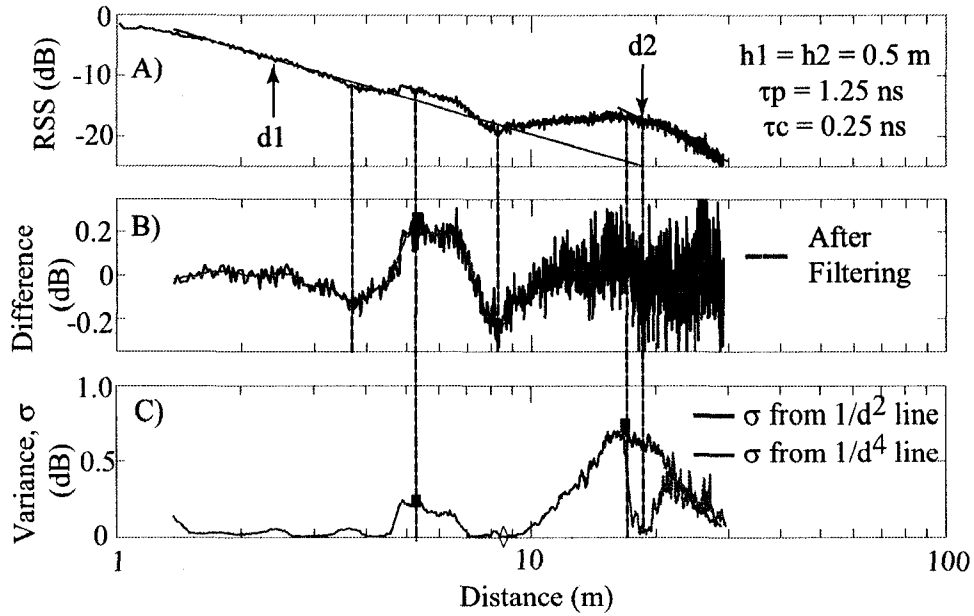


Figure B.4. Determination of breakpoint distances and maxima and minima in the received signal strength data for $h_1 = h_2 = 0.5$ m.

in the Taku parking lot. The transmitting and the receiving UWB systems are held over the ground. As discussed in section 3.2.1 (Figure 3.10), the received UWB pulses, show one direct path pulse and one or more reflected pulses.

Figure B.5 shows the geometry and the variables required to calculate the permittivity of the ground. The peak amplitude of the direct path pulse, V_D , is given as

$$V_D = \frac{V_0}{D} G_t(\theta_D) G_r(\theta_{Dr}) \cos \psi_D \quad (\text{B.2})$$

where V_0 is the voltage at a reference distance of 1 m, $G_t(\theta_D)$ is the gain of the transmitting antenna along the direct path direction defined by the angle θ_D from the antenna axis which is aligned parallel to the local vertical, $G_r(\theta_{Dr})$ is the gain of the receiving antenna for an angle of arrival θ_{Dr} defined from the antenna axis aligned along the local vertical, and ψ_D is the projection angle of the direct path electric field on the receiving antenna axis.

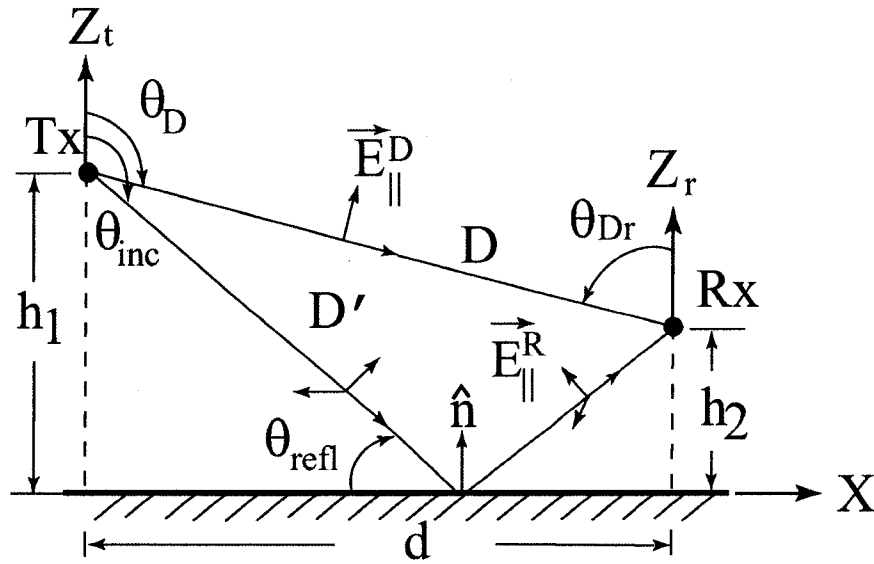


Figure B.5. Problem geometry to calculate the permittivity of the ground.

The peak amplitude of the reflected path pulse, V_R , is given as

$$V_R = \frac{V_0}{D'} G_t(\theta_{inc}) G_r(\theta_{refl}) \cos\psi_R \Gamma(\theta_R) \quad (\text{B.3})$$

where V_0 is the voltage at a reference distance of 1 m, $G_t(\theta_{inc})$ is the gain of the transmitting antenna along the reflected path direction defined by the angle θ_{inc} from the antenna axis, $G_r(\theta_{refl})$ is the gain of the receiving antenna for an angle of arrival θ_{refl} defined from the antenna axis, Γ is the reflection coefficient of the ground, θ_R is the reflection angle defined from the normal to the ground and ψ_R is the projection angle of the reflected path electric field on the receiving antenna axes.

Dividing Equations B.3 and B.2, and rearranging gives

$$\Gamma(\theta_R) = \frac{V_R D' G(\theta_D) G(\theta_{Dr}) \cos\psi_D}{V_D D G(\theta_{inc}) G(\theta_{refl}) \cos\psi_R} \quad (\text{B.4})$$

where the transmitting and receiving antenna are assumed to have identical patterns $G_t = G_r = G$. The relative permittivity of the medium is derived for Transverse Magnetic (TM)

polarization [Bertoni, 2000] by solving the quadratic equation

$$\epsilon_r^2 - \left(\frac{\Gamma - 1}{(\Gamma + 1) \cos \theta_{inc}}\right)^2 \epsilon_r + \left(\frac{\Gamma - 1}{\Gamma + 1}\right)^2 \tan^2 \theta_{inc} = 0 \quad \text{(B.5)}$$

The quadratic equation has two solutions for ϵ_r out of which one solution is always less than or equal to 1 and the other solution provides an estimate of the effective relative permittivity of the ground. It should be noted that to calculate ϵ_r of the ground, the reflected pulse should not overlap with the direct path pulse. This will occur in the first regime when the time delay difference between the direct and the reflected paths is greater than the pulse duration, τ_p .

The thickness of the snow layer on the ground is calculated from measurements consisting of a direct path and two non-overlapping reflected paths. In such a case, the time difference, $\Delta\tau$, between the first and the second reflected paths is used in determining the width, w , of layer using the formula

$$w = \frac{c\Delta\tau}{2\sqrt{\epsilon_r}} \left[\frac{(n^2 - 1)d^2 + n^2(h_1 + h_2)^2}{n^2d^2 + n^2(h_1 + h_2)^2} \right]^{-1/2} \quad \text{(B.6)}$$

The refractive index of the layer is measured using the peak amplitude of the direct path pulse and first reflected pulse in Equations B.4 and B.5. It should be noted that the w of the snow layer can be measured only when there are two reflected pulses accompanying the direct path pulse in the received signal.

It should be noted that each of the reflected pulses may have multiple overlapping pulses. This is because the layers of snow/ice/water on the ground may not have definitive boundaries and will result in multiple overlapping reflected pulses which will change the duration, amplitude and envelope of the net reflected pulse.

B.4.2 Measurements

The UWB pulses were measured in the Taku parking lot for different ground conditions and at different transmitter heights. The measured pulses were categorized as:

1. Type A: one direct path pulse and one non-overlapping reflected pulse.
2. Type B: one direct path pulse and two non-overlapping reflected pulses.
3. Type C: one direct path pulse and three non-overlapping reflected pulses

Figure B.6A shows the pulse received by a pair of PulsONTM 200 systems for $h_1 = h_2 = 0.5$ m on 16 March 2004. The received signal has one direct path pulse and one non-overlapping reflected pulse. The reflected pulse is longer in duration than the direct path pulse and may have more than one overlapping pulses. Therefore such pulses can be used to measure an effective ϵ_r of the ground.

Figure B.6B shows the pulse received by a pair of PulsONTM 200 systems for $h_1 = 1$ m and $h_2 = 0.5$ m on 01 December 2004. The received signal has one direct path pulse and two non-overlapping reflected pulses. Such pulses will provide an estimate of w of the snow layer.

Figure B.6C shows the pulse received by a pair of PulsONTM 200 systems for $h_1 = h_2 = 0.5$ m on 16 March 2004. The received signal has one direct path pulse and three non-overlapping reflected pulses. Such pulses will provide an estimate of ϵ_r and w of multiple layers of ice/snow/water on the ground.

Pulses in all the three above types are used to measure the effective ϵ_r of the ground. Pulses in types B and C are used to measure the w of the snow/ice layer. Table B.4 shows the list of days when the measurements were done, the ground conditions, and the recorded temperature.

The net ϵ_r of the snow covered ground is measured for 16 March 2004, 21 November 2004, 01 December 2004, and 22 December 2004. Figures B.7A, B.7B, B.7C, and B.7D show the measured ϵ_r as a function of distance for each of those days. The measured ϵ_r of the snow is 3.75 ± 1.25 for the 16 March 2004 case, 3.95 ± 2.76 for the 21 November 2004 case, 4.19 ± 1.76 for the 01 December 2004 case, and 4.56 ± 1.02 for the 22 December 2004 case. From past measurements, it is known that the range of relative permittivity of snow/ice, in the 3 GHz to 37 GHz frequency range, is from 1 to 6 and depends on the water content and

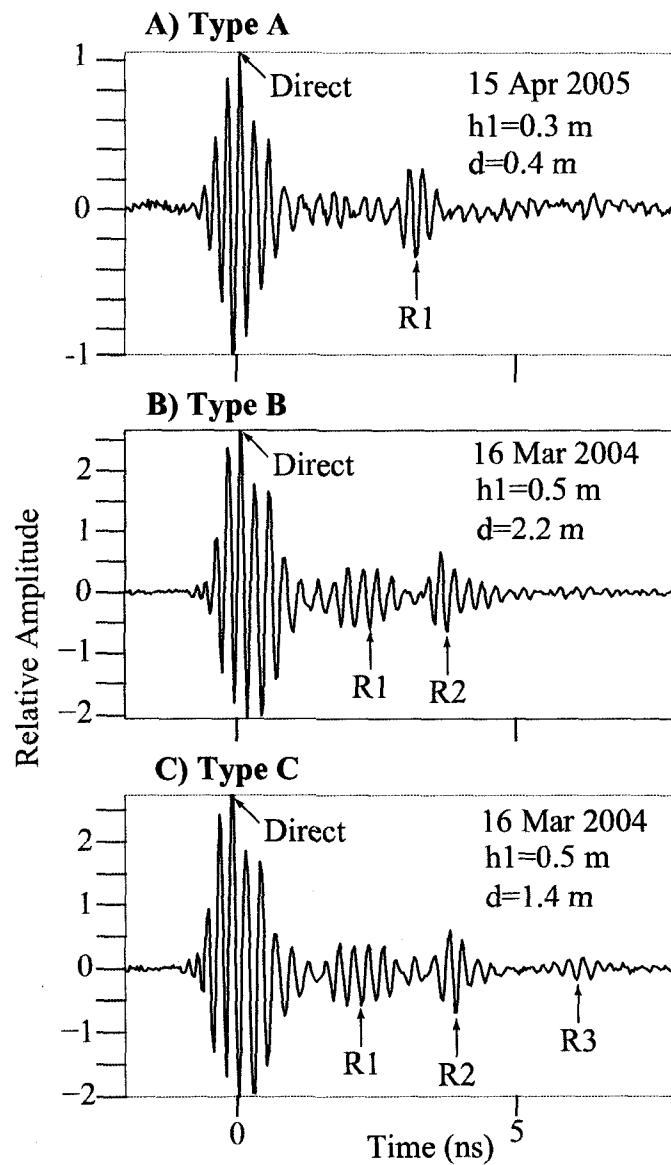


Figure B.6. Examples of received UWB pulses measured in the Taku parking lot at UAF. A) Received pulse categorized as type A with one direct path pulse and one non-overlapping ground reflected pulse. B) Received pulse categorized as type B with one direct path pulse and two non-overlapping ground reflected pulses. C) Received pulse categorized as type C with one direct path pulse and three non-overlapping ground reflected pulses. Note that each reflected pulse could be due to multiple reflected pulses overlapping with one another resulting in a change in the duration, amplitude and envelope of the pulse.

Table B.4. Dates, temperature and ground conditions in the Taku parking lot when the UWB propagation measurements were performed.

Date	Temperature (° F)	Ground Condition
16 March 2004	16	hard and packed snow
18 November 2004	6	hard and packed snow
21 November 2004	22	hard and packed snow
01 December 2004	30	loose and soft snow
22 December 2004	6	hard and packed snow
07 April 2005	50	dry (with few cm size stones)
13 April 2005	36	wet with patches of snow
14 April 2005	40	wet with patches of snow
15 April 2005	38	wet with patches of snow
21 April 2005	36	wet with patches of snow

the packing of snow per cubic centimeter [Tiuri *et al.*, 1984; Hallikainen *et al.*, 1986]. The imaginary part of the permittivity of snow is 0.27 at 3.78 GHz [Matzler, 1996]. The range of permittivity of the water layer is from 50 to 81 and the ground is from 10 to 30 [Bertoni, 2000]. The conductivity of the ground varies from 10^{-4} S/m to 10^{-1} S/m [Parsons, 2000].

A detailed survey of the pulses needs to be done in the future to categorize the 9400 pulses captured at different transmitter heights and on different days to calculate the real and imaginary part of the effective permittivity of the snow and the width of snow on the ground.

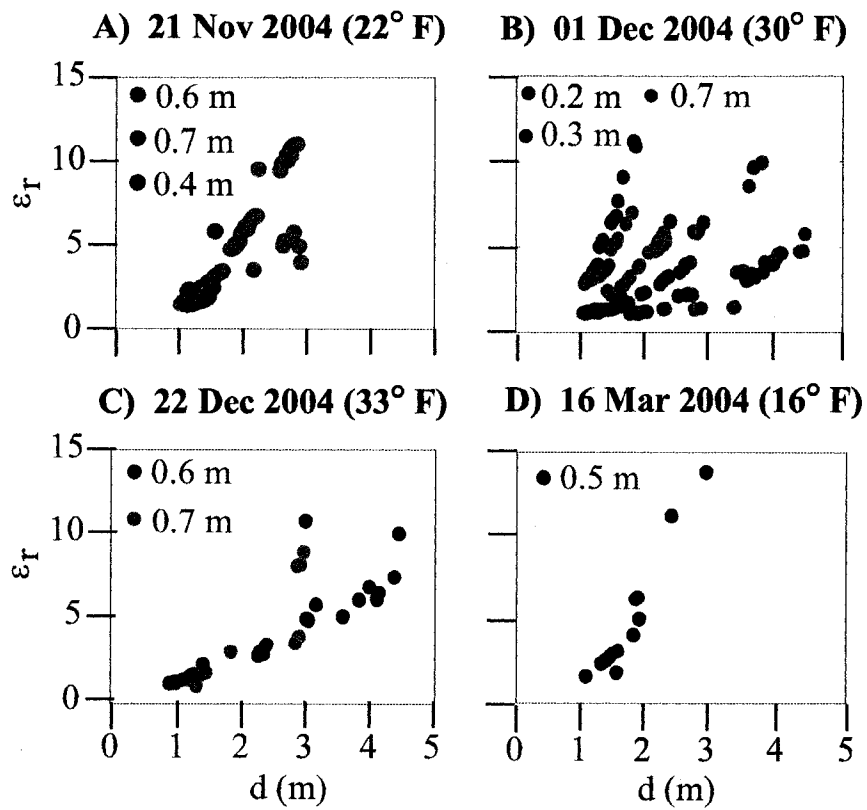


Figure B.7. Measured ϵ_r as a function of distance in the Taku Parking Lot.